uOttawa

L'Université canadienne
Canada's university

FACULTÉ DES ÉTUDES SUPÉRIEURES ET POSTOCTORALES

uOttawa

L'Université canadienne
Canada's university

FACULTY OF GRADUATE AND POSDOCTORAL STUDIES

Christina Vanderwel
AUTEUR DE LA THÈSE / AUTHOR OF THESIS

M.A.Sc. (Mechanical Engineering)
GRADE / DEGREE

Department of Mechanical Engineering
FACULTÉ, ÉCOLE, DÉPARTEMENT / FACULTY, SCHOOL, DEPARTMENT

Coherent Structures in Uniformly Sheared Turbulence

TITRE DE LA THÈSE / TITLE OF THESIS

Starvos Tavoularis
DIRECTEUR (DIRECTRICE) DE LA THÈSE / THESIS SUPERVISOR

CO-DIRECTEUR (CO-DIRECTRICE) DE LA THÈSE / THESIS CO-SUPERVISOR

M. Yaras

R. Milane

Gary W. Slater
Le Doyen de la Faculté des études supérieures et postdoctorales / Dean of the Faculty of Graduate and Postdoctoral Studies

COHERENT STRUCTURES IN UNIFORMLY SHEARED TURBULENCE

by

Christina M. Vanderwel

A thesis submitted to
the Faculty of Graduate and Postdoctoral Studies
in partial fulfillment of
the requirements for the degree of

MASTER OF APPLIED SCIENCE

in Mechanical Engineering

Ottawa-Carleton Institute for Mechanical and Aerospace Engineering
University of Ottawa
Ottawa, Canada

December 2009

Your file Votre référence
ISBN: 978-0-494-61300-9
Our file Notre référence
ISBN: 978-0-494-61300-9

Abstract

Uniformly sheared turbulent flow with a turbulence Reynolds number Re_λ in the range from 80 to 100 has been generated in a water tunnel and its instantaneous structure has been examined using flow visualization, laser Doppler velocimetry and particle image velocimetry. The flow was found to consist of regions with nearly uniform velocity, which were separated by relatively strong shear layers containing large vortices. The concentration of vortices and the probability distribution functions of their directions of rotation, strengths, sizes and shapes in three characteristic planes of the flow have been determined. These results, as well as hydrogen bubble visualisations and high-speed scans of injected dye patterns, support the hypothesis that horseshoe-shaped vortices are prevalent in this flow.

Acknowledgements

I would like to acknowledge the help of several people in the production of this work. First of all, I would like to express my gratitude to my supervisor Dr. Stavros Tavoularis for his confidence in me, for letting me have a go at such an interesting research topic, and for his guidance during this journey of learning.

I recognise the financial support of the University of Ottawa, Le Fonds Québécois de la Recherche sur la Nature et les Technologies, and the Natural Sciences and Engineering Research Council of Canada, which allowed me to pursue this research unhindered by financial worries.

I am grateful to everyone at the machine shop, but especially Leo Denner and Mike Burns, for their assistance and enthusiasm with the design, manufacturing, and setup of the lab equipment.

My fellow graduate students and colleagues were also a great help, and I hope they feel I have reciprocated the same support and good will. A special thanks goes to George Choueiri who was always a helpful presence in the lab from the very start, and I very much appreciate the help of his wife Anne-Lise, without whose expertise I would never have obtained such striking hydrogen bubble photos. Furthermore, I would like to acknowledge the work of Cameron McKnight-MacNeil, who illustrated several "artist's renditions" of the idealised vortices I imagined.

Lastly, I must recognize the support given to me by my partner Ereth, who is always willing to lend a hand or some advice in all aspects of my work, not to mention his unfailing support in life, for which I am always appreciative.

Table of Contents

List of Tables

List of Figures

Nomenclature

a	rate of growth of the integral length scale
d_b, d_p	diameter of bubbles or particles
$e_{\alpha\beta}$	mean rate of strain tensor
h	depth of water in the test section
g	gravitational acceleration
k	turbulent kinetic energy
k_o	reference value of the turbulent kinetic energy
l	length of test section
$L_{11,1}$	integral length scale
L_o	reference value of the integral length scale
l_r	apparent length of the measurement plane
L_r	true length of the measurement plane
l_t	distance from the camera to the measurement plane
m_{ij}	turbulence anisotropy
N	number of samples
Pr	rate of production of turbulent kinetic energy
Re_L	Reynolds number based on the integral length scale
Re_λ	Reynolds number based on the Taylor microscale

Re_θ	Reynolds number based on the momentum thickness in the turbulent boundary layer
S	vortex strength
S^*	shear-rate parameter
t	time
t_s	time scale of the shear
t_u	eddy lifetime
U_c	mean centreline velocity
U_i	velocity
$\langle U_i \rangle$	ensemble-averaged velocity
$\overline{U_i}$	time-averaged velocity
u_i	velocity fluctuation
u'_i	root-mean squared velocity fluctuation
U_g	terminal velocity of bubbles or particles
V_x, V_y	vortex convection velocity in the frame of reference of the PIV plane
w	width of test section
x, y	directions in the frame of reference of the PIV plane
x', y', z'	reference indices in the scanning dye visualisation
x_i	position vector in the test section
ΔX	mean displacement of particles in PIV
y^+	dimensionless distance from the wall in the turbulent boundary layer

Greek symbols

α magnification factor

γ particle-to-fluid density ratio

δ boundary layer thickness in the turbulent boundary layer

δ_{ij} Kronecker delta

δ_ν viscous length scale in the turbulent boundary layer

ϵ rate of dissipation of turbulent kinetic energy

ϵ_u velocity precision uncertainty

η Kolmogorov microscale

θ the angle of the inclined plane with respect to the flow direction

λ swirling strength

$\lambda_{11,1}$ Taylor microscale

μ dynamic viscosity of the fluid

ν kinematic viscosity of the fluid

ρ density of the fluid

ρ_p density of the particles

σ turbulent kinetic energy growth exponent

τ dimensionless development time

τ_s time constant of particle-fluid interactions

τ_w wall shear stress in the turbulent boundary layer

ϕ reference angle

Ω vorticity

Acronyms

CCD charge-coupled device (camera sensor)

CCW counter-clockwise

CW clockwise

DNS direct numerical simulation

ITTC International towing tank conference

LDV laser Doppler velocimetry

PDF probability density function

PIV particle image velocimetry

PVC polyvinyl chloride

USF uniformly sheared flow

Chapter 1

Introduction

1.1 Motivation

Most natural and technological flows are turbulent, exhibiting a disorderly and random motion of the fluid. Although turbulent flows occur in abundance, they are still not fully understood. The statistical equations that define the fluid motion cannot admit exact analytical or numerical solutions because the system of governing equations is open. In addition to analytical methods, research has attempted to better understand turbulence using experimental and numerical methods, however these methods are often unable to resolve the motions with a wide range of scale, which occur in turbulent flows. Many useful relations have been extracted by focussing on mean flow properties but, although the overall understanding of its structure and properties has improved over the decades, turbulence remains a topic of intense research.

The concept of the coherent structure was introduced formally within the last half-century. It has become a topic of intense research due to the development of advanced computational methods, mainly direct numerical simulations, and high-power experimental techniques such as PIV. The name coherent structure refers to a vortical entity of fluid with spatially correlated properties that can be observed with some level of recurrence in a turbulent flow [18]. The study of these large-scale structures brought some order to the notion of turbulence, which was previously often viewed as an assembly of mostly chaotic fluctuations [18]. Coherent structures have been studied in a wide range of shear flows, including mixing layers, jets, wakes, and boundary layers.

The introduction of coherent structures has resulted in many advancements in the understanding and application of turbulence. In the turbulent boundary layer, coherent structures are associated with the production of turbulent kinetic energy and transport of turbulent properties [7]. The large-scale coherent structures are responsible for the entrainment of fluid at the interface of the turbulent and non-turbulent flow [19]. The control of coherent structures has resulted in technological advances, including drag reduction and noise suppression. It has been assessed that riblets on shark skin reduce drag by organising the coherent structures in the boundary layer [47]. Similar control of coherent structure formation and interaction in jet and wake flows can suppress noise generated by the turbulent motions [19].

Uniformly sheared flow (USF) is an example of a turbulent shear flow for which the types of coherent structures have not been thoroughly investigated. USF is characterised by homogeneous turbulence sheared by a uniform mean velocity gradient and, although idealized and relatively simple, it is relevant to the understanding of the structure of more complex shear flows. Shear appears in essentially all types of turbulence including boundary layer flows, jets, and wakes, and is the main mechanism of turbulence production [26], [7]. However, being free of any boundaries and inhomogeneity, USF has a much simpler analytical representation than these other flows.

The investigation of the coherent structures in USF is desirable to help fill in the gaps in the understanding of coherent structures. Because USF has properties that are similar to those of the outer layer of the turbulent boundary layer, this is also a suitable environment to investigate the effects of shear in the absence of rigid walls. The present results will also add to the database for the validation of theoretical and numerical models of turbulence [19].

1.2 Objectives

The goal of this work is to identify and characterise the coherent large-scale structures found in uniformly sheared flow (USF).

This study follows up on the previous flow visualisation study by Kislich-Lemyre [23] at the University of Ottawa, who was the first to document experimentally the presence of horseshoe-shaped vortices in USF. In the present work, with the use of particle image velocimetry (PIV), the instantaneous flow field was mapped in order to identify and analyse all of the flow structures present. Novel methods of analysis were used to capture a statistically significant number of vortices and to determine probability distributions of their properties in three characteristic planes of the flow.

In addition to PIV, several other complementary experimental methods were used to investigate this flow. Laser Doppler Velocimetry (LDV) was used to measure time-averaged local flow properies and compare them to previous studies. Hydrogen bubbles were used to visualise the flow structures, providing the opportunity to observe the length scales, time scales, and shapes of the dominant structures. Scanned laser-illuminated dye injection was used to visualise the three-dimensional dye patterns in the flow.

1.3 Organization of the thesis

This thesis is divided into seven chapters. The background and previous works are discussed in Chapter 2. A description of the flow facilities and measurement apparatus is provided in Chapter 3. The measurement procedures as well as the algorithms developed for the analysis of results are discussed in Chapter 4. The results from all the measurement techniques are described in Chapter 5, which is subdivided to present the results from the four separate methods: LDV, scanning dye visualisation, hydrogen bubble visualisation, and PIV. The results of these experiments are evaluated and compared in Chapter 6, in which some interpretations and consequences of the findings are presented and discussed. Chapter 7 summarises the results and presents some thoughts on future directions of research.

Chapter 2

Analytical background and literature review

2.1 Fundamentals of turbulence

All turbulent flows are characterised by common traits. Flow velocity and pressure are not uniform but fluctuate in space and time. The fluctuations occur with a wide range of time and length scales, related to the scales of motion in the flow. Unlike irrotational potential flow, turbulence contains fluctuating vorticity and requires energy to sustain itself. Turbulence is also associated with enhanced mass and heat transfer compared to laminar flows under comparable conditions and these properties often make turbulence desirable in technological applications.

Classic examples of turbulence include flow through pipes or channels, wakes, jets, boundary layers formed by the retardation of fluid along a stationary wall, and mixing/shear layers that form between two fluid streams moving at different velocities. The strength of turbulence present in these cases has been correlated with the turbulence Reynolds number. Higher Reynolds numbers indicate the dominance of inertial forces and result in stronger turbulence, in which flow properties have stronger fluctuations.

Turbulence is described mathematically by statistical means in such a way as to elucidate the analysis of the fluctuations of flow properties. The statistical description of turbulence in terms of means and fluctuations is known as Reynolds decomposition and can be applied to any flow property such as velocity, pressure, or vorticity. In the case of velocity, the Reynolds decomposition approach decomposes the local instantaneous velocity value into the mean component and the fluctuating component. When the flow is stationary, the mean properties do not change in time; therefore, the mean component can be calculated using a time-average. Following common convention, the ensemble-averaged component will be denoted by angled brackets and the fluctuating component will be denoted by a lower case letter. The decomposition of all three components of velocity is, according to this convention,

$$
\begin{aligned}
U_1 &= \langle U_1 \rangle + u_1 \\
U_2 &= \langle U_2 \rangle + u_2 \\
U_3 &= \langle U_3 \rangle + u_3.
\end{aligned}
\tag{2.1}
$$

The standard deviations of the fluctuating properties will be denoted by primes, as, for example,

$$u_1' \equiv \sqrt{\langle u_1^2 \rangle}. \tag{2.2}$$

The Reynolds stress tensor is defined as $-\rho\langle u_i u_j \rangle$ [43] [32]. The off-diagonal and the diagonal components of the Reynolds stress tensor are known as the shear stresses and normal stresses respectively. The anisotropy tensor is defined as

$$m_{ij} = \frac{\langle u_i u_j \rangle}{2k} - \frac{1}{3}\delta_{ij}, \tag{2.3}$$

where the Kronecker delta is

$$\delta_{ij} = \begin{cases} 1, & \text{if } i = j \\ 0, & \text{if } i \neq j \end{cases}. \tag{2.4}$$

The Reynolds shear stresses are intimately associated with the mean transfer of momentum in the flow and so are very important parameters in the description of turbulence.

The turbulent kinetic energy per unit mass is defined as

$$k \equiv \frac{1}{2}\langle u_i u_i \rangle. \tag{2.5}$$

It describes the kinetic energy of the fluctuating flow field and is related to the strength of the turbulence. Turbulence is continually dissipating its kinetic energy and requires an external source of energy for its maintenance.

2.2 Uniformly sheared flow

Uniformly sheared flow (USF) is an experimental approximation of homogeneous shear flow. Homogeneous shear flow is a theoretical example of turbulence whose statistical properties are defined to be homogeneous or uniformly distributed in space such that they are independent of translation of the coordinate system. This ideal case is very difficult, if not impossible, to accomplish experimentally. However, nearly homogeneous approximations may be attained and are referred to as uniformly sheared flows.

2.2.1 Governing equations

Uniformly sheared flow is the simplest self-sustaining turbulent flow. The mean velocity components in all directions are zero, except for the streamwise direction, in which the mean velocity varies linearly with the transverse position as

$$\begin{aligned} \langle U_1 \rangle &= \frac{d\langle U_1 \rangle}{dx_2} x_2 && (2.6) \\ \langle U_2 \rangle &= 0 && (2.7) \\ \langle U_3 \rangle &= 0. && (2.8) \end{aligned}$$

In USF, the mean rate of strain tensor and the mean vorticity vector take the simplified forms

$$\langle e_{\alpha\beta} \rangle = \frac{1}{2}\left(\frac{\partial \langle U_\alpha \rangle}{\partial x_\beta} + \frac{\partial \langle U_\beta \rangle}{\partial x_\alpha}\right) \rightarrow \begin{bmatrix} 0 & \frac{1}{2}\frac{\partial \langle U_1 \rangle}{\partial x_2} & 0 \\ \frac{1}{2}\frac{\partial \langle U_1 \rangle}{\partial x_2} & 0 & 0 \\ 0 & 0 & 0 \end{bmatrix}, \tag{2.9}$$

$$\langle \Omega \rangle = curl\,(\langle U \rangle) \rightarrow \left(0, 0, -\frac{\partial \langle U_1 \rangle}{\partial x_2}\right), \tag{2.10}$$

in which the Greek indices are not summed. The mean deformation resulting from this strain is a stretching in the direction of $+45\,^\circ$ in the $x_1 - x_2$ plane. Furthermore, the mean vorticity only has a non-zero component in the direction normal to the $x_1 - x_2$ plane.

The addition of the uniform velocity gradient introduces a production term in the kinetic energy balance equation that counters the turbulent kinetic energy dissipation rate, ϵ. This balance equation is

$$\frac{dk}{dt} = -\langle u_1 u_2 \rangle \frac{d\langle U_1 \rangle}{dx_2} - \epsilon. \tag{2.11}$$

The fundamental time scale of the USF is defined as the inverse of the velocity gradient, i.e.

$$t_s = \left(\frac{d\langle U_1\rangle}{dx_2}\right)^{-1}. \tag{2.12}$$

A dimensionless development time, also representing the total strain experienced by the turbulence during its development, can be defined in terms of the downstream position in the flow x_1 and the centreline velocity U_c as

$$\tau = \frac{x_1}{U_c}\frac{d\langle U_1\rangle}{dx_2}. \tag{2.13}$$

Unfortunately, in an idealized, unbounded USF, there is no obvious externally imposed length scale, which complicates the dimensional analysis.

The eddy lifetime, which is a measure of the time between the generation and destruction of the dominant turbulent eddies is defined as

$$t_u = \frac{2k}{\epsilon}. \tag{2.14}$$

The shear-rate parameter is defined as

$$S^* = \frac{t_u}{t_s} = \frac{d\langle U_1\rangle}{dx_2}\frac{(2k)}{\epsilon}, \tag{2.15}$$

which is the ratio of the turbulence timescale to the timescale of the mean shear. It represents the relative strength of the turbulent activity compared to the production by mean shear.

2.2.2 Previous research

The research investigating USF has been predominantly through experimental methods using wind tunnels or water tunnels, as well as by direct numerical simulations (DNS), which were introduced in the late 1970s.

One of the first attempts at generating USF in the laboratory was performed by Rose [37] in the 1960s. He inserted a grid across the entrance to a wind tunnel test section, with this grid consisting of parallel rods with non-uniform spacing in order to create the velocity gradient. However, this shear-gererating grid was found to produce spatially varying scales in downstream flow. The shear generating apparatus was afterwards improved by Champagne, Harris, and Corrsin [5] using the same wind tunnel facility. Instead of using bars, they used plates to separate the flow into ten parallel, equal-width channels each with adjustable internal resistances made up of screens. The flow-separating channels at the inlet were the key to the uniformity of scales and have been used in many subsequent investigations USF ([45], [46], [8], [13], [23]). Alternative methods of generating the uniform shear include using curved screens, tapered honeycombs, or separate fluid supplies, as described by Dunn and Tavoularis [11].

Among the most important experimental studies of USF, subsequent to the work by Champagne at al., are the following.

- Harris, Graham, and Corrsin (1977) [15], who studied USF with greater shear rates and longer development times than those in the work by Champagne et al.

- Tavoularis and Corrsin (1981) [45], who used hot-wire anemometry to study the properties of USF with a superimposed uniform mean temperature gradient in a wind tunnel.

- Rohr et al. (1988) [36], who studied USF generated with multiple pumps in a water tunnel using hot-films.

- Tavoularis and Karnik (1989) [46], who used hot-wire anemometry to document the effect of the shear value on USF in a wind tunnel.

- De Souza, Nguyen, and Tavoularis (1995) [8], who used LDV to study USF in a high speed wind tunnel.

- Ferchichi and Tavoularis (2000) [13], who used hot-wire anemometry to study the effect of the turbulent Reynolds number on the fine structure of USF in a wind tunnel,

- Kislich-Lemyre (2002) [23], who used LDV and flow visualisation to study the large-scale structure of USF in a water tunnel.

Most of these experimental studies have focussed on the collection of time-averaged statistical properties of the flow, using hot-wire anemometry or more recently laser

Doppler velocimetry. As Tavoularis [42] demonstrates, the Reynolds stresses and turbulent kinetic energy grow exponentially in USF. For example, the turbulent kinetic energy changes as

$$k = k_o e^{\sigma\tau}, \tag{2.16}$$

where k_o is some initial value and the rate of growth σ could generally depend on the shear rate [43]. In all studies in which the flow was sufficiently developed, σ was found to be positive, as summarised by Tavoularis and Karnik [46]. The downstream development time is important, as it is observed that the exponential growth only begins after a sufficient development time has been achieved ($\tau \gtrsim 5$ [46]), [32]. It is also important to note that the magnitudes of the non-zero Reynolds stresses are ordered as $\langle u_1^2 \rangle > \langle u_3^2 \rangle > \langle u_2^2 \rangle > -\langle u_1 u_2 \rangle$, as remarked upon by [45], [46], [23] among others. Some insight into this ordering can be found by studying the Reynolds stress equations, which demonstrate that the streamwise normal stress is larger than the other two because it receives energy directly from the mean shear, whereas the other two normal stresses are not produced directly but receive energy from the streamwise component through pressure-strain rate covariance terms. This is also reflected in the typical anisotropy values summarised by Tavoularis [43] as

$$m_{11} \simeq 0.17\ , \quad m_{22} \simeq -0.13\ , \quad m_{33} \simeq -0.04\ , \quad m_{12} \simeq -0.15. \tag{2.17}$$

The previous studies also measured the integral length scale L_{11} and Taylor's microscale λ_{11}. The integral length scale is observed to consistently grow from a starting value, which is comparable to the spacing of elements in the shear generating apparatus. Tavoularis and Corrsin [45] found this growth was essentially linear. Tavoularis and Karnik [46] fit a power law to this growth with an exponent of 0.8 ± 0.1, but admitted that the fit could also be linear within the uncertainty of their measurement. In either case, the growth appeared to be independent of shear value. The Taylor's microscale is found to be nearly constant with downstream position [42], [46].

The only experimental study of USF that used flow visualisation was the work done by Kislich-Lemyre [23].This work as well as those from the follow-up study of Menu [28] were performed using the same facilities as the present study. The measured flow properties using LDV in these two studies are summarised in Table 2.1. The

	Kislich-Lemyre (2002)		Menu (2004)	
	low speed	high speed	low speed	high speed
U_c (m/s)	0.073	0.136	0.135	0.224
$d\langle U_1 \rangle / dx_2$ (s^{-1})	0.25	0.405	0.432	0.613
P_r ($\mathrm{m}^2/\mathrm{s}^3$)	-	-	3.0 E-6	9.5 E-6
ϵ ($\mathrm{m}^2/\mathrm{s}^3$)	-	-	1.4 E-6	4.1 E-6
ϵ / P_r	-	0.47	0.47	0.43
L_{11} (m)	0.05	0.05	0.078	0.110
λ_{11} (m)	-	0.023	0.022	0.020
Re_λ	-	150	130	200

Table 2.1: Summary of average flow properties measured by Kislich-Lemyre [23] and Menu [28] using the same facilities as the current study.

centreline velocity, shear rate, and turbulent Reynolds number in these studies were lower than those in USF generated in wind tunnels. Kislich-Lemyre's conclusions regarding the coherent structures of USF will be discussed in Section 2.3.2.

With the advent of faster and larger computers, direct numerical simulation (DNS) has become a useful tool for studying the structure of turbulent flows. DNS results generally agree with the results of the experimental studies. Among the DNS studies of interest in the present context are those by Lee et al. (1990) [26], Rogers and Moin (1987) [35], and Kida and Tanaka (1992) [22]. Lee et al. were able to simulate USF with $S^* \approx 33$, whereas the simulations of Rogers and Moin have $S^* \approx 8$. One main advantage DNS has over experimental methods is that they provide the instantaneous flow properties without distorting the flow. Most of the current knowledge of coherent structures in USF is based on DNS studies. The main disadvantage of DNS is that they are limited to relatively small Reynolds numbers and development times.

Several studies have observed similarities between the large-scale structure of USF and that of the turbulent boundary layer [26] [8]. In comparing the structures of USF to those found in the turbulent boundary layer it is important to consider the dimensionless flow parameters that characterise the turbulence. De Souza et al. [8] discuss the relevance of the shear parameter S^* and the turbulent stress anisotropy component m_{12}. These values vary over the depth of the turbulent boundary layer but are homogenous in USF. Figure 2.1 summarises the magnitudes of these values in both the boundary layer and previous experiments of USF. The majority of experimental studies of USF have $S^* \approx 11$ and $m_{12} \approx 0.15$, including the works of Tavoularis and Corrsin [45], Tavoularis and Karnik [46], and Kislich-Lemyre [23]. As illustrated by the figure, these 'low shear' USF experiments have comparable turbulence properties to those of the outer boundary layer.

2.3 Coherent structures

Turbulence is composed of random fluctuations with wide ranges of length and time scales. Coherent structures may appear with time scales that are longer than the previously defined eddy lifetime. These structures have repeating patterns and could be distinct from the non-coherent turbulence. A typical example of such a structure is the hairpin vortex, which has been shown to contribute to a large fraction of the total Reynolds stresses in the turbulent boundary layer [1].

The analysis of coherent structures can be based on the triple decomposition by Hussain [18],

$$F(\mathbf{x}, t) = \overline{F}(\mathbf{x}) + f_c(\mathbf{x}, t) + f_r(\mathbf{x}, t) \tag{2.18}$$

where $\overline{F}$ is the time-averaged mean of any random process F, f_c is the coherent component, and f_r is the non-coherent component.

2.3.1 Coherent structures in the turbulent boundary layer

Most of the research concerning coherent structures has focussed on the case of a steady, fully developed, incompressible turbulent boundary layer in a smooth-walled pipe or channel with a zero pressure gradient. In this flow, the turbulence is inhomogeneous, it has a range of scales of eddies, and its kinetic energy is continually produced by shear along the solid wall.

Typical results of some of the first investigations of the coherent structures in the turbulent boundary layer obtained using smoke and hydrogen bubble visualisation are presented in Figure 2.2. As discussed by Adrian [1], these methods identified turbulent bulges, which occur near the edge of the boundary layer. These large scale motions are two to three times longer than the average thickness of the boundary

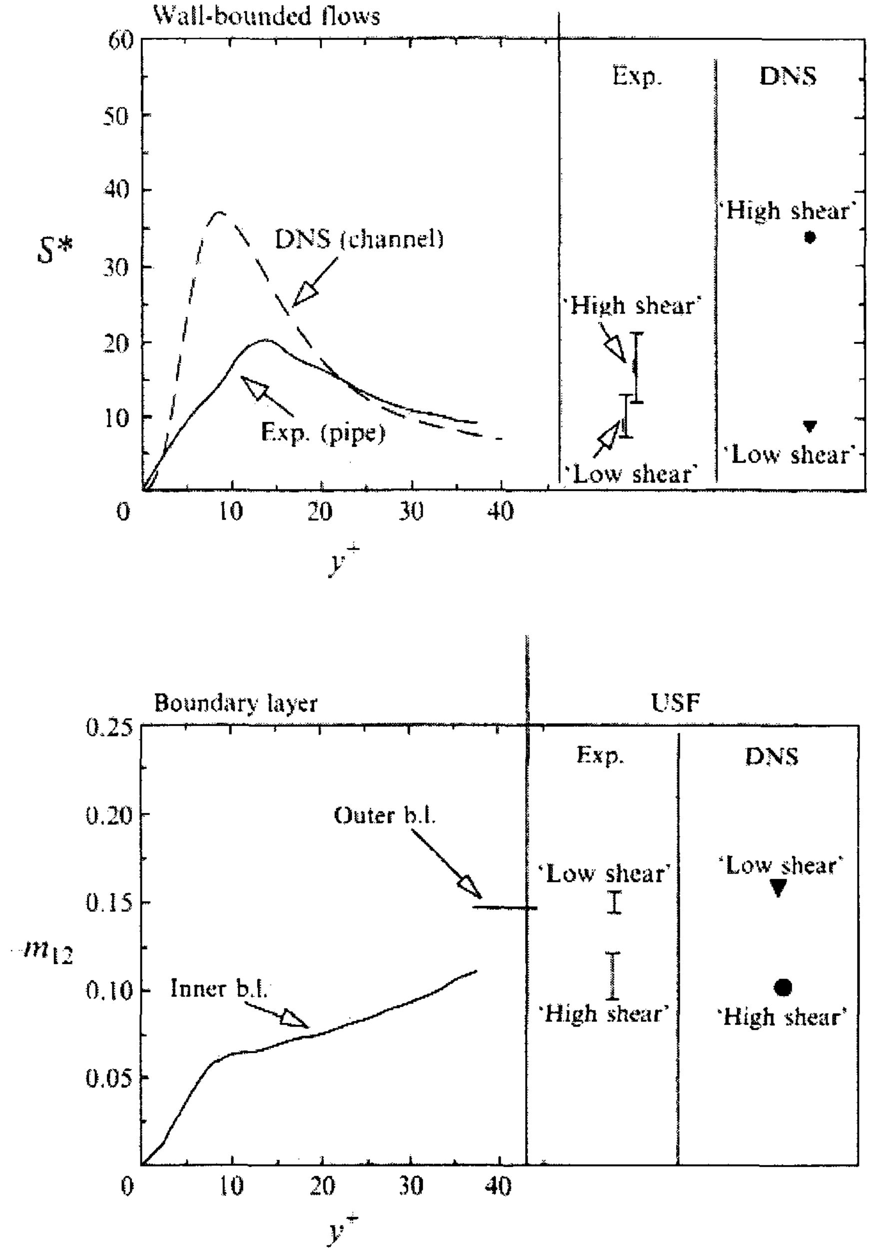

Figure 2.1: Variation of the parameters S^* and $-m_{12}$ in the present and previous flows. (Reproduced with permission from the work by DeSouza et al. [8].)

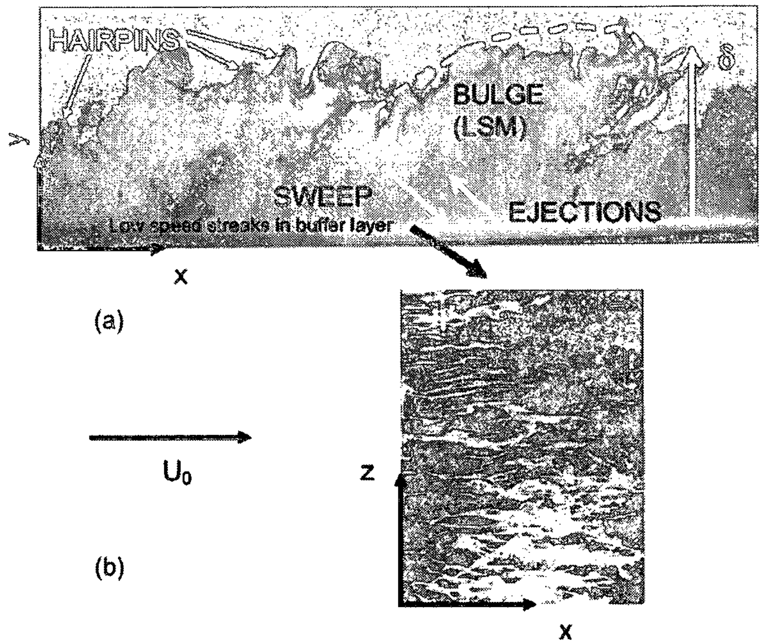

Figure 2.2: (a) Smoke visualisation of the turbulent boundary layer viewed from the side by Falco (1977) and (b) hydrogen bubble visualisation of streaks, viewed from the top by Kline (1967). (Reproduced with permission from [12] and [24].)

layer. Smaller vortices within the bulges can be identified near the turbulent/non-turbulent interface. Low-momentum streaks have also been identified in the buffer layer. Earlier studies also introduced the concept of bursting, which occurs when a streak of fluid is observed to lift away from the wall in an ejection motion.

In 1952, Theodorsen proposed the idea of the horseshoe vortex forming in shear flows, when a spanwise vortex filament encounters a transverse obstruction. In boundary layers, the perturbed part of the filament, now further away from the wall, would be convected downstream faster than the rest of the filament, resulting in the horseshoe shape. This theory did not gain much attention at the time, but, as further experiments and numerical simulations created more evidence, interest was renewed. These structures have since also been referred to as hairpin vortices, which occur at higher Reynolds numbers and are slightly more elongated than the horseshoe structures [16]. Among the studies of coherent structures, one could mention the following:

- Head and Bandyopadhyay (1981) [16], who used inclined light sheets to visualise hairpin-shaped smoke patterns in turbulent boundary layers.

- Smith (1984), who observed the formation of successive in-line hairpin vortices using hydrogen bubble visualisation in low-Reynolds number boundary layer flow.

- Perry and Chong (1982), who tested a theoretical model of the turbulent boundary layer scattered with hairpin vortices to predict the statistical properties of the flow, including the mean velocity, Reynolds stresses, and spectra.

- Moin and Kim (1982), who used large eddy simulations (LES) of turbulent channel flow to produce a 3D model of the characteristic hairpin vortex.

- Robinson and Kline (1991), who catalogued the vortical structures in a low-Reynolds number boundary layer using direct numerical simulations (DNS).

Based on the results of these studies, the properties of the characteristic hairpin vortex can be summarised as follows [1]. The hairpin vortex consists of a strong spanwise vortex at the head and two legs trailing in a nearly streamwise direction, similar to that sketched in Figure 2.3a. The head and legs rotate such that an ejection of flow (labelled as a Q2 event) occurs behind the head and between the legs, inclined approximately by 45° with respect to the wall. A sweep (labelled as a Q4 event) occurs outside the hairpin legs as fluid is pushed down. The streamwise streaks observed using hydrogen bubble visualisation can be interpreted as low-momentum flow being forced up by the ejection between the hairpin legs. In a frame of reference moving with the speed of the hairpin head, the ejection event creates a local maximum in the velocity field, which is a crucial feature for identifying these structures. These characteristics make up the 2D hairpin vortex signature sketched in Figure 2.3b, which is a cross-section of the vortex in the $x-y$ plane. It can be shown that even a simple vortex model shaped like a lambda (Λ) will produce this pattern. This signature can be detected by experimental means, such as single-plane particle image velocimetry (PIV), to identify the presence of a hairpin vortex. Though drawn symmetrically in Figure 2.3, a hairpin can be asymmetric if the ejection event has a spanwise component or if distorted by another nearby eddy. The single hairpin model successfully explains a mechanism for the generation of Reynolds stress and the transport of vorticity and shear away from the wall.

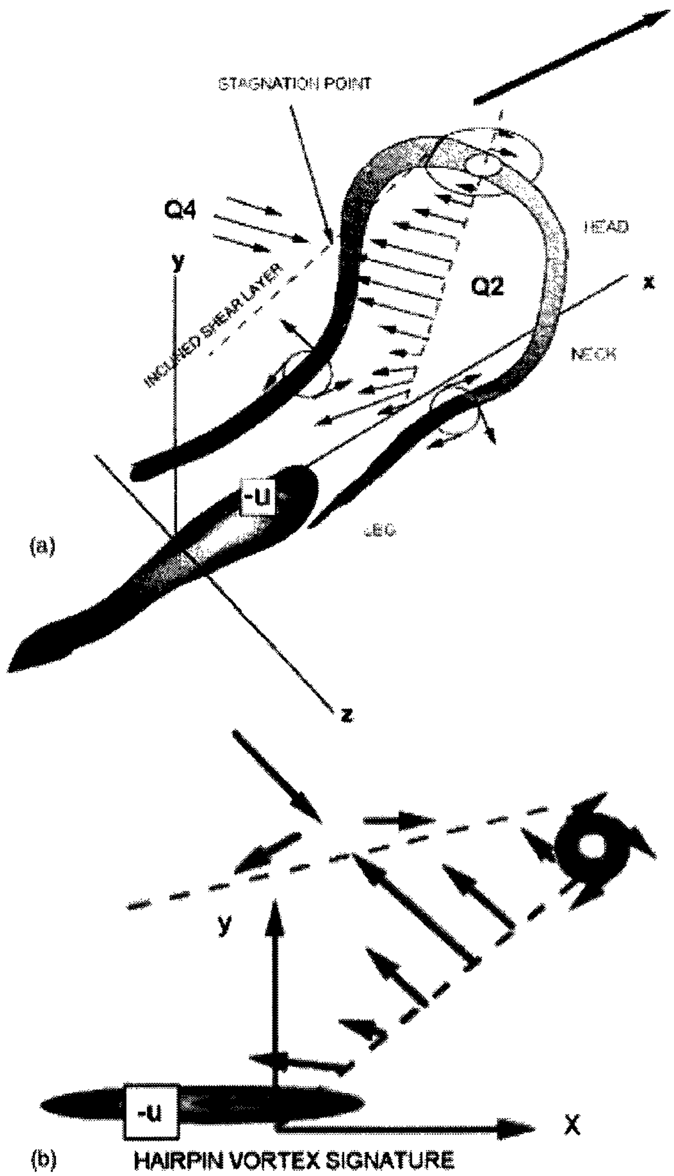

Figure 2.3: (a) A sketch of a hairpin eddy attached to the wall and (b) its hairpin vortex signature. (Reproduced with permission from [1].)

Hairpin vortices tend to occur in packets [1]. These packets correspond to the observations of large-scale bulges in flow visualisations. They have also been identified in both DNS and PIV results as groups of hairpin vortices in close proximity moving at nearly the same velocity. The development of these packets has been modelled using DNS. The first step is the formation of a single hairpin vortex from an initial disturbance. With the addition of a turbulent mean flow, if the first eddy is weak it will dissipate; however, if it is strong enough, it will continue to develop as it is convected downstream. Arches will form between its legs that separate into secondary vortices attached to the wall behind the original vortex. Finally, the downward flow outbound of the legs may form neighbouring counter-rotating quasistreamwise vortex filaments. These filaments then join via arches, creating more hairpins in a transverse direction. In this way, a single initial disturbance is enough to generate a chain reaction of hairpin development called autogeneration. Even in a mean flow with very strong turbulence, hairpins can be distinguished from the chaotic movement.

As the Reynolds number increases, the length scale of the finest turbulent motions becomes finer, and the required computational power increases, making numerical simulations prohibitively expensive. For this reason, most high Reynolds number results have been obtained experimentally. In the flow field shown in Figure 2.4, vortex heads are seen to appear in groups on the edge of a ramp-like structure. The packets tend to be larger, containing more hairpins per packet than in low Reynolds number flow. The alignment of the vortex heads divides the flow into zones of uniform momentum. A low momentum zone is found below the hairpins in the interiors of the packets. The packets create much longer regions of backflow than a single hairpin could produce, and better agree with measurements of long correlation lengths. These also explain the long streaks observed through visualisation that could not be formed by the short legs of a single hairpin. The string of ejections caused by the passage of a packet coincides with the observations of bursts.

In addition to the previous observations, it has been found that packets tend to be aligned in groups, as illustrated in Figure 2.5. These groups have been termed very-large-scale motions. These groups consist of packets of varying age, which travel with different velocities. The younger packets are small, are located near the wall,

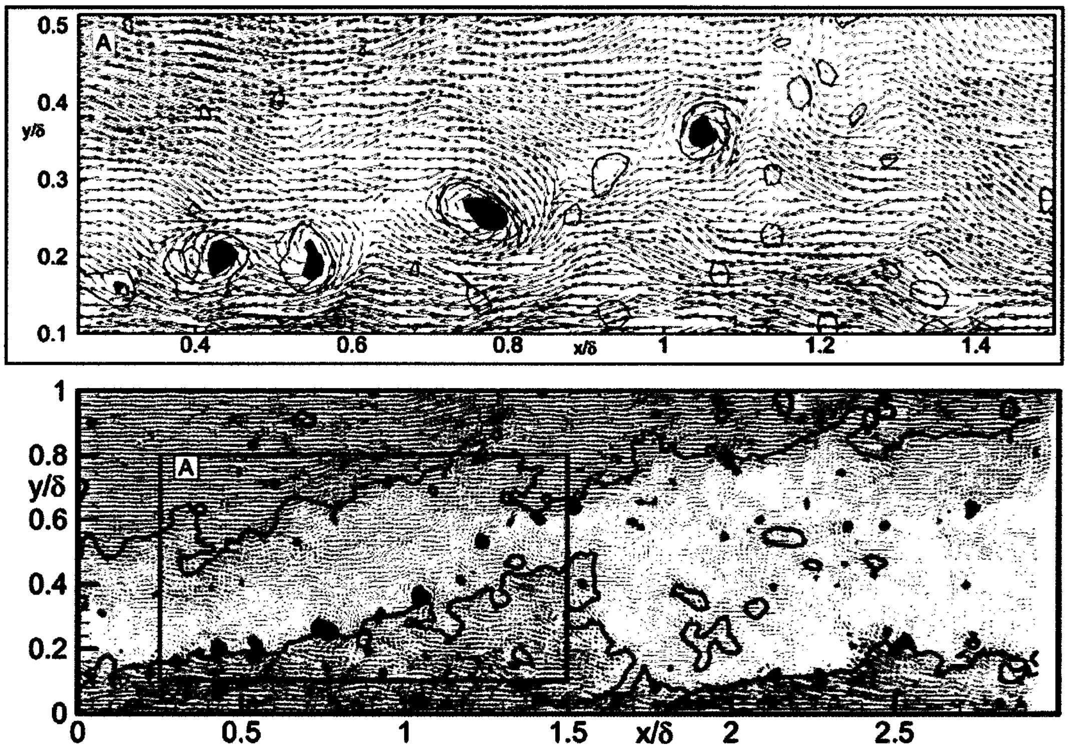

Figure 2.4: A sample velocity flow field at $Re_\theta = 7705$ measured in the turbulent boundary layer using single-plane particle image velocimetry. The contours are swirling strength in the lower plot and spanwise vorticity in the upper plot. The solid line in the lower plot separates the zones of uniform momentum. The velocity field has been manipulated by subtracting 76% (lower plot) and 79% (upper plot) of the free stream velocity so that the vortices may be visualised. (Reproduced with permission from [1].)

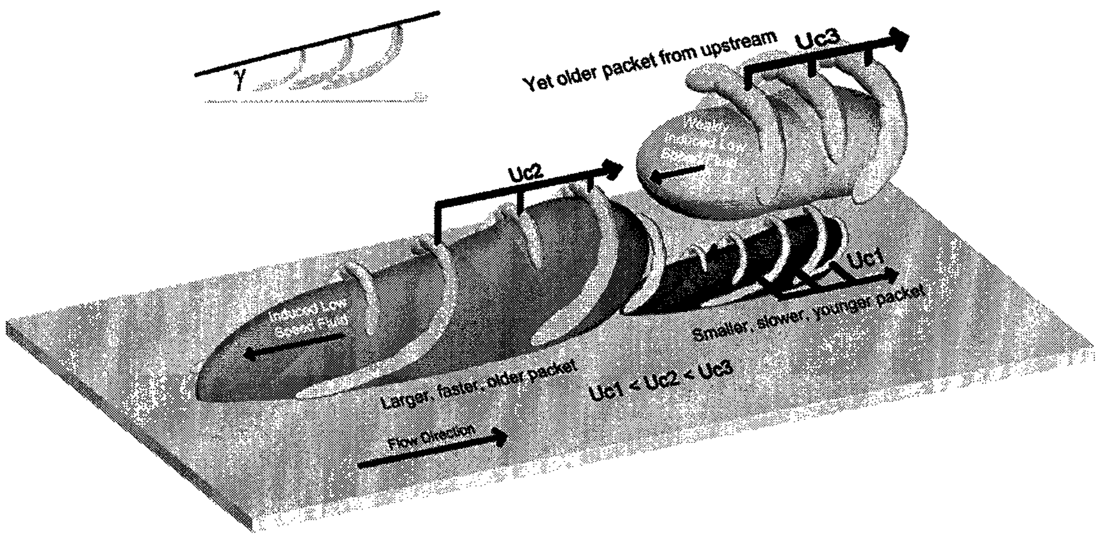

Figure 2.5: Illustration of the hierarchy of packets in a group. (Reproduced with permission from [1].)

and have low velocity, while the older ones have moved away from the wall and are moving at a higher velocity. Superposition of the effects from different packets in a group results in stratification of the zones of uniform momentum. Hence, three scales of coherent motions are identified: the hairpins, the packets of hairpins, and the groups of packets. Very-large-scale and large-scale motions account for over one half of the turbulent stresses. Although hairpins generally occupy less then 4.5% of the total cross-sectional area, they influence another 25% of this area. The remaining area may contain contorted structures that are hard to distinguish from the rest of the flow or perhaps entirely unknown structures.

2.3.2 Coherent structures in uniformly sheared flow

Most of the investigations into coherent structures in USF have been computational. The inspiration for these investigations has been to better understand the mechanisms involved in coherent structures discovered in the turbulent boundary layer. The theory discussed by several researchers is that the mean shear is the key mechanism of the development of hairpin vortices, and the presence of the wall has a secondary effect [35], [26], [23], [7].

The DNS work by Rogers and Moin [35] and the follow-up study by Adrian and Moin [3] suggest that hairpin vortices are prevalent in USF. Rogers and Moin studied the vorticity field of USF and observed that the strongest vorticity vectors are oriented predominantly at 45° and -135° with respect to the direction of flow. Vortex lines passing through the points of strongest vorticity trace out hairpin-shaped vortices in the instantaneous vorticity field. These coherent hairpin vortices are equally as likely to be inverted as oriented upright and in either case are shown to have a magnitude of vorticity eight to nine times that of the mean vorticity. Adrian and Moin further processed the same DNS data using a conditional-averaging method. This method attempts to identify the characteristic eddy pattern by averaging the local flow properties of many sample eddies. The sample eddies are collected using the detector event of coherent upward ejection or downward sweep found in the instantaneous flow. Two characteristic eddy patterns are identified. The upward ejection event is associated with a hairpin vortex inclined at about 45° to the flow direction like in the turbulent boundary layer. The other characteristic eddy is an inverted hairpin vortex inclined at -135° and is associated with downward sweeps.

Coherent structures in USF were also explored by Lee et al. [26] who performed DNS at a much higher shear rate. From contours of the streamwise turbulent velocity, they identified streaks of low and high speed velocity similar to those shown in the viscous sublayer of the turbulent boundary layer. The elongation of the streaks was found to grow with the shear parameter S^*; however, the streaks did not reach the same lengths as those in the turbulent boundary, even at matching values of S^*.

Experimental studies of coherent structures in USF have been limited to flow visualisation. Kislich-Lemyre [23] recorded laser-illuminated dye patterns in several planes through the flow that corresponded to portions of hairpin vortices. Swirls in the $x_1 - x_2$ plane such as in Figure 2.6 were interpreted as vortex heads, whereas the mushroom-shaped patterns in an inclined spanwise plane such as in Figure 2.7 coincided with the counter-rotating vortex legs. The presence of streamwise streaks was also documented. This evidence points to the presence of hairpin-shaped vortices in USF comparable to those generated in turbulent boundary layers, though no information was provided concerning the frequency of inverted hairpins. The study

Figure 2.6: Dye visualisation of the head of a hairpin vortex in the $x_1 - x_2$ plane. (Reproduced from [23]).

Figure 2.7: Dye visualisation of mushroom-shaped vortex pairs in an inclined plane 45° between the $x_1 - x_3$ and $x_2 - x_3$ planes. (Reproduced from [23]).

went on to investigate the effect of a moving wall on the USF structure. The addition of the moving wall distorted the coherent structures of the USF in its proximity. The shear associated with the relative motion of the flow and the wall also generated additional types of coherent structures. The interactions between these two distinct types of coherent structures and the kinematic effects of the wall resulted in strongly inhomogeneous, multi-scale turbulence. The large-scale structure of this turbulence was strongly correlated with the magnitude and direction of relative motion. The visual study concluded that the key source of turbulence production near the wall is friction-related shear (no-slip), whereas obstruction by the wall (no-penetration) acts to organise and suppress oncoming turbulent structures originating in the USF.

2.3.3 Methods of identification of coherent structures

The search for an identification scheme for coherent structures is intertwined with debate on their definition. Adrian [1] describes a coherent structure as some vortex or movement that lasts long enough and is large enough to catch your eye. This descriptive statement relates well to the feeling one gets after staring at flow visualisations for some time, but cannot serve for identifying vortices in PIV-generated velocity maps. Robinson [34] suggests that in a frame of reference moving with a speed equal to that of the vortex, the streamlines should close around the vortex core. This method is useful for identifying vortices in a flow with a uniform mean velocity, however, in order to search for vortices in a flow with a velocity gradient, the frame of reference must be shifted many times to accommodate the full range of flow velocities.

Many of the initial studies of coherent structures (such as [35], [18]) suggested the use of vorticity magnitude as a criterion for locating vortices. Vorticity, however, does not discriminate between mean shear and isolated vortices and therefore is not very suitable for identifying vortices in shear flows. Maps of the vorticity magnitude are useful for discriminating the direction of rotation, making it easy to identify counter-rotating vortex pairs.

Like the vorticity, swirling strength is also independent of the frame of reference, but unlike vorticity it is able to discriminate between the mean shear and isolated vortices. As explained by Zhou et al. [48], swirling strength is defined as the square of the imaginary part of the complex eigenvalue of ∇u. This is mathematically calculated from the velocity field as [25]

$$\lambda = max\left(0, -\left(\frac{dU_1}{dx_2} \times \frac{dU_2}{dx_1} - \frac{1}{2}\left(\frac{dU_1}{dx_1} \times \frac{dU_2}{dx_2}\right) + \frac{1}{4}\left(\frac{dU_1}{dx_1}^2 + \frac{dU_2}{dx_2}^2\right)\right)\right). \quad (2.19)$$

A common method to locate vortices (for example [2], [27], [14]) is to use a cut-off value of swirling strength, and define the location of relatively strong vortices by locating peaks of swirling strength that are higher than this cut-off value. A similar method of vortex identification is the Q-criterion, which was introduced in the late 1980s, before the establishment of swirling strength as a common method of vortex identification. It has been shown that the Q-criterion and the swirling strength are mathematically related (see [4], [9]).

Proper orthogonal decomposition, which is the same as the Karhuenen-Loeve method in mathematics, can be used to identify the vortices containing the most kinetic energy. This method decomposes the vector field into a series of orthogonal basis functions, starting with the function on which the energy of the projected data would be maximised. The decomposed basis vector fields are ordered in decreasing influence on the kinetic energy. Therefore, by only using the first few of the basis fields, one can separate out those eddies with the strongest influence on the kinetic energy. For more information on this method the reader is referred to the book by Holmes, Lumley, and Berkooz [17].

Template-matching or pattern recognition algorithms can also be implemented to search for recurring patterns of coherent structures. The conditional-sampling analysis of DNS results uses a similar process [3]. However, because the researcher must define a detection event, this method may be biased to only recognise those patterns one anticipates to exist, and not necessarily any unexpected structures.

The quantitative analysis of PIV results in this thesis relies mainly on swirling strength for the identification of coherent structures. The velocity vectors (in a convected frame) surrounding vortices identified in this way were then checked visually to ensure that they encircled the vortex cores as suggested by Robinson [34]. In general, the visual check did not reveal any problems with this approach.

Chapter 3

Experimental facilities and instrumentation

All of the present experiments were conducted in the University of Ottawa's closed-loop water tunnel. The tunnel was equipped with a shear generator and flow separator in order to create a uniformly sheared water flow.

Several experimental methods were used. These included laser Doppler velocimetry (LDV), particle image velocimetry (PIV), and flow visualisation with hydrogen bubbles and with dye injection. The facility and equipment required for these experiments are described in the following sections.

3.1 Water tunnel

The closed-loop water tunnel holds a fluid volume of about 15,000 L; it is illustrated in Figure 3.1. The water is drawn from the test section through the return pipe by an axial pump, which is located below the settling chamber and is powered by a 5.6 kW electric motor through a variable speed controller. The large settling tank contains a series of perforated plates, foam sheets, and a natural fibre filter in order to precondition the flow entering the test section. The test section has a width of 0.54 m, is approximately 3.9 m long (4.2 m without the flow separator used for USF), and can be filled with water up to a height of approximately 0.77 m; however, the water tunnel was only filled to a depth of 0.426 m for these experiments. The test section allows optical access through the three glass walls, the free surface, and a glass window at the downstream end of the tunnel. Filtration and chlorination processes are timed to occur nightly through a secondary loop to maintain clean, clear water, and to remove particles larger than about 30 μm in the water that would possibly introduce errors into the LDV and PIV measurements. Further details of the construction and features of the water tunnel are provided by Kislich-Lemyre [23] and Dunn [10].

An orthogonal coordinate system was defined in the test section of the water

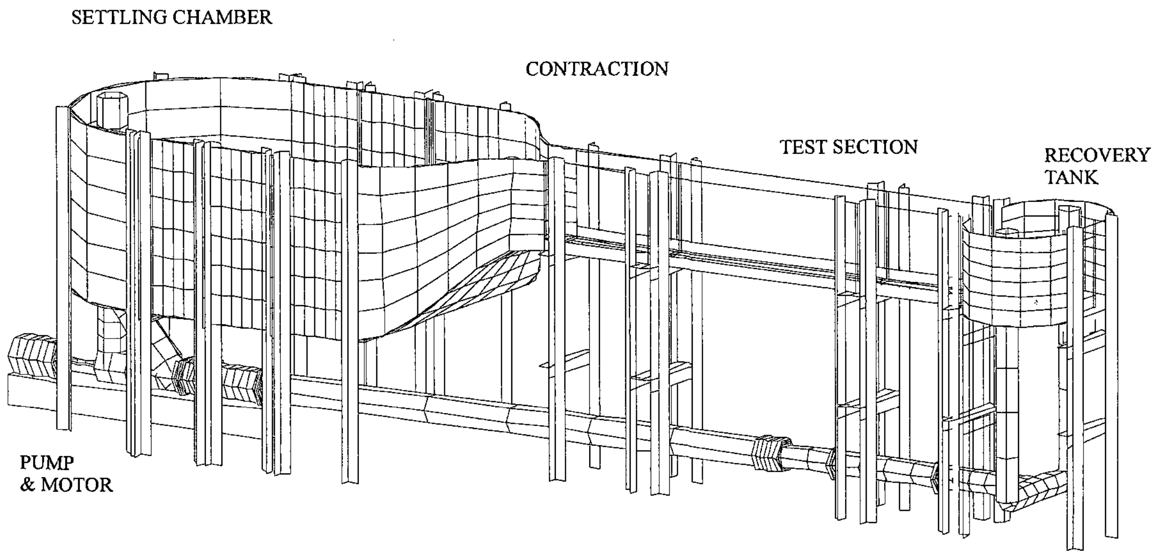

Figure 3.1: The closed-loop water tunnel facility at the University of Ottawa. (Reproduced from Kislich-Lemyre [23].

tunnel for all measurements in the USF. The x_1 direction corresponds to the direction of flow. The x_2 direction is in the transverse (vertical) orientation in the water tunnel, which coincides with the direction of the velocity gradient. The third component x_3 is orthogonal to both x_1 and x_2 and corresponds to the spanwise direction along the horizontal width of the tunnel. This coordinate system is illustrated in Figure 3.2. Its origin is located at the exit of the flow separator, at the bottom centre of the channel.

3.2 Shear generator and flow separator

The uniform shear was generated by a shear generating plate followed by a flow separator inserted at the entrance of the test section. The same equipment used in the work of Kislich-Lemyre was used in this study, with the exception of a slight redesign in the frame of the flow separator and a small adjustment of the blockage distribution of the shear generator. This equipment is displayed in Figure 3.3.

The shear generator is an aluminium plate, perforated in a non-uniform manner such that the flow obstruction changes from a lower value near the top to a higher value near the bottom. As shown in Figure 3.3, the solidity of the plate was carefully adjusted to create a linearly varying flow profile. Fishing line was stretched across

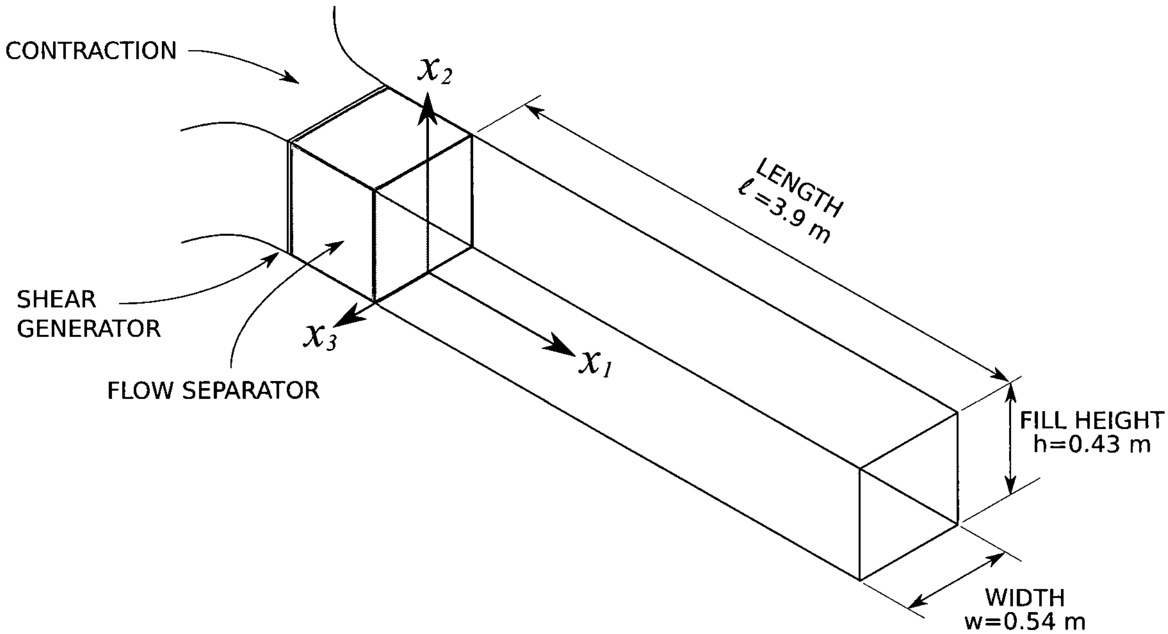

Figure 3.2: Definition of the coordinate system and basic dimensions of the test section.

the 6th, and 7th slots, counting from the top, to slightly increase the flow resistance in these areas. An additional line across the 3rd slot from the top was used in the current study to improve the flow profile, reducing the velocity of a local jet that was forming near $x_2/h = 0.7$. As with all aluminium equipment, the shear generator was removed from the water overnight to prevent chlorine deposits on it.

The shear generator was followed by the flow separator allowing the flow to enter the test section parallel to the axis on the mean. This also ensured the uniformity of the initial length scale of turbulence (i.e. making it proportional to the width of the channels). The flow separator is made up of 16 panes of tempered glass, 1.6 mm thick, which slide into a PVC frame held together by Inconel and stainless steel braces, as illustrated in Figure 3.4. The panes of glass line up with the solid parts of the shear generator that separate the different perforated sections.

A PVC endplate was inserted across the end of the test section to improve the flow development along the tunnel. This endplate partially blocked the bottom 325 mm of the tunnel at the end of test section, countering the suction effect of the return pipes, which are located in the bottom of the receiving tank. The effectiveness of this

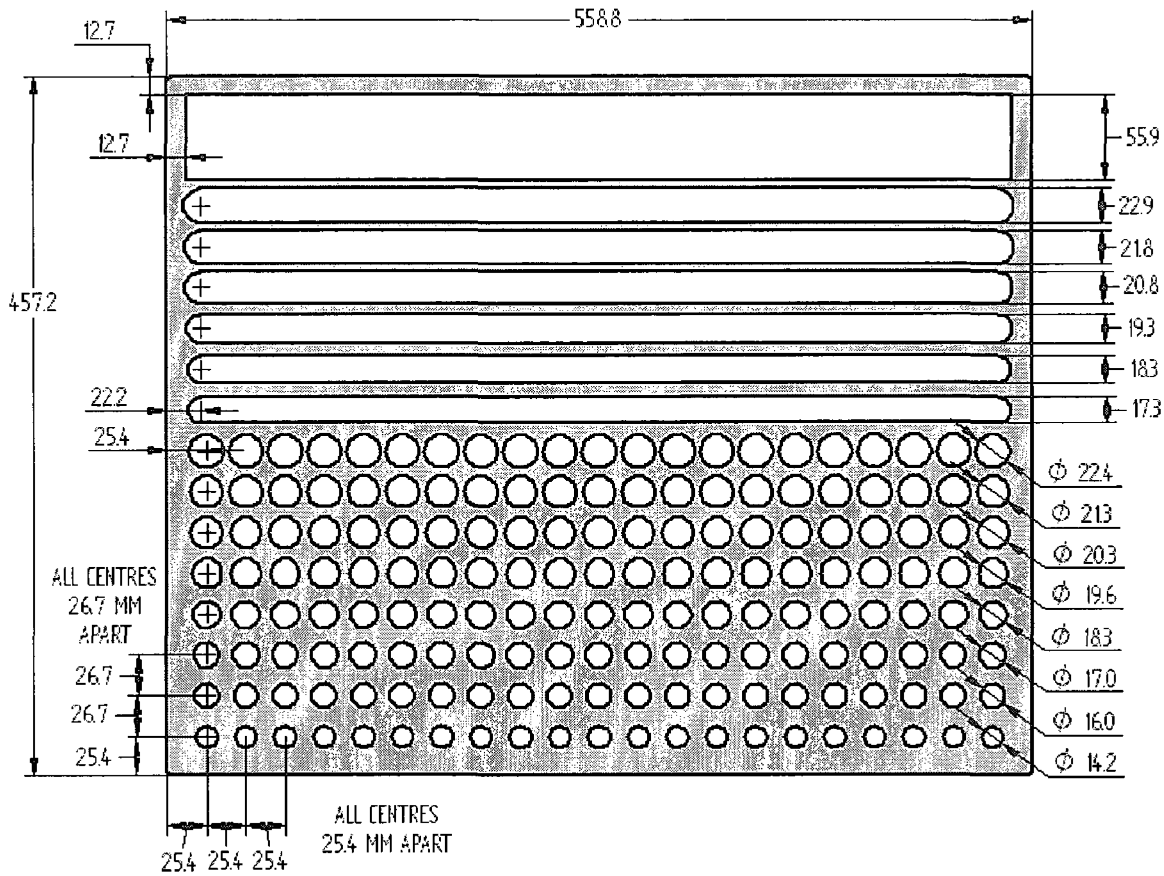

Figure 3.3: The shear generator plate (dimensions in mm).

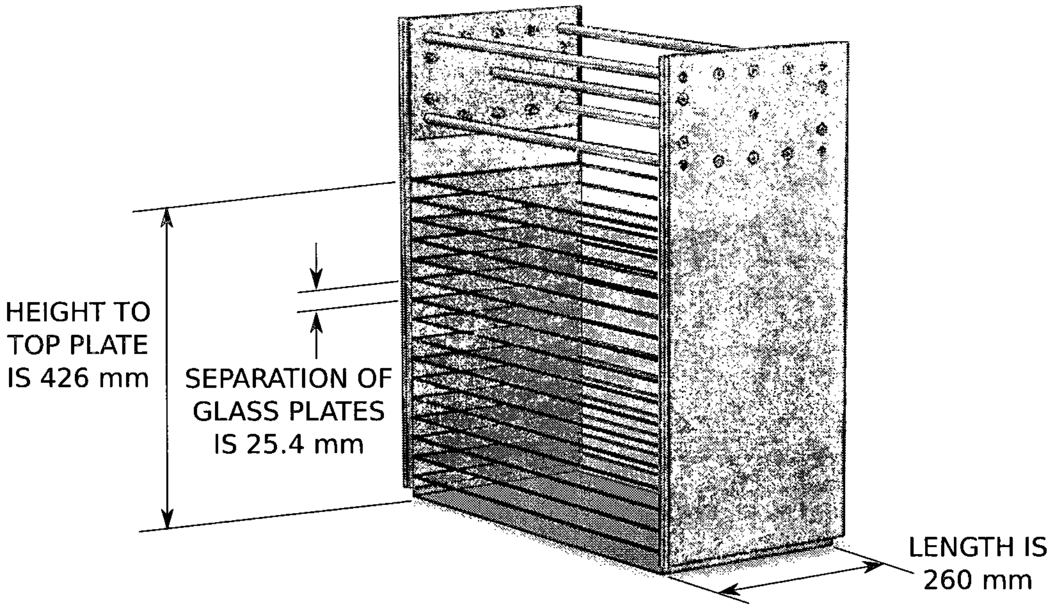

Figure 3.4: The flow separator assembly.

endplate in improving the shear uniformity was verified using LDV.

3.3 Traversing system

The water tunnel is equipped with three independent traversing systems composed of three pairs of stainless steel rails fastened below, above, and on one side of the test section, along each of which carts can be traversed smoothly. The locations of these rails are illustrated in Figure 3.5.

The cart mounted to the side rails carries a horizontal traverse mounted to a vertical traverse to allow for full 3D traversing of equipment. Both traverses can be separately positioned with the use of stepper motors that are controlled with a LabVIEW program on a PC interface connected through a Velmex motor controller. A sketch of this side cart will be shown in a later section (Figure 3.9).

The streamwise motions of the bottom and side carts are controlled using a continuous electric motor with velocity feedback. For both units the streamwise position along the rails is controlled by means of a cable connected to an axle near the exit of the test section. By inserting the screw from the disc on the axle into the pulley

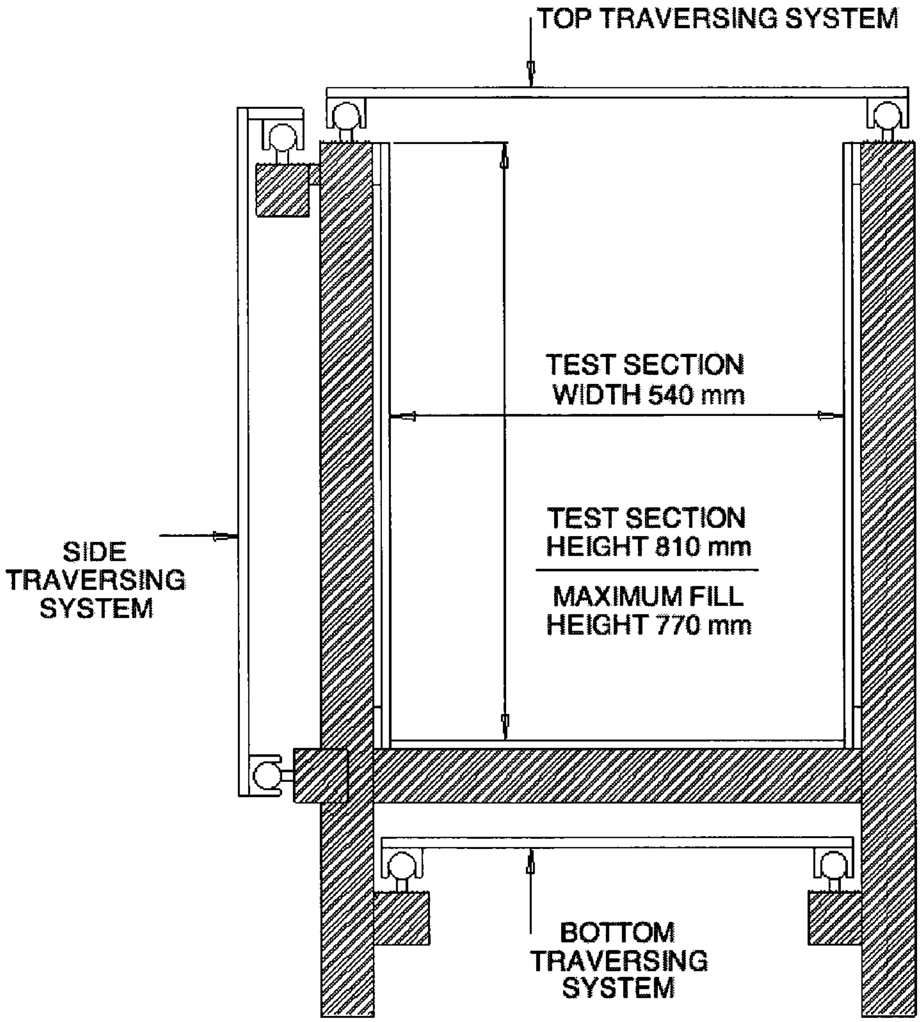

Figure 3.5: The traversing systems above, beside, and below the test section of the water tunnel.

holding the cable, the two traverses may be engaged or disengaged to the motor depending on whether one or both need to be traversed. By engaging both traverses, the two platforms can be made to move together. The motor was connected to the pulleys through a 100:1 reducer, which increases the available torque by decreasing the shaft rotational velocity. A motor speed of about 4000 rpm was required for a traverse speed of 0.2 m/s. End-stop sensors were wired to the motor controller and placed at the either end of the test section to stop the motor when the carts reach the end of their track.

3.4 Dye injection system

Dye injection is a method of flow visualization that can be used to identify coherent structures. There is reduced turbulence and mixing in the core of a vortex, so dye is less quickly diffused, leaving a high concentration in the vortex core. The main disadvantage of dye visualisation is that the flow only becomes visible at the interfaces between the dyed and non-dyed fluids. Swirls cannot be identified where there is no dye or where the dye has constant concentration. Therefore, analysis can mainly be conducted only on the dye interfaces where contrast is maximised.

Two fluorescent dyes, dibromofluorescein and fluoroscein sodium salt solutions, were used. These dyes fluoresce when excited by specific wavelengths of light. The peak emission wavelength of these dyes is about 517 nm and the peak absorption wavelength is about 495 nm [20]. These dyes do not diffuse well in water and therefore provide clear 2D patterns when excited with a laser sheet downstream in the test section. 3D patterns, however, are not improved using fluorescent dye, as the dye looks like a cloud when illuminated by flood lights.

The dye was stored in three one-litre canisters that could be pressurised with the use of compressed air from the laboratory supply. Opening the outlet valve let the dye flow through a streamlined dye-injection tube that was lowered to the appropriate depth in the water, with its orifice facing downstream. The tube was placed before the shear generating apparatus so that the wake and jet effects resulting from the probe or dye injection did not distort the downstream structure of the flow.

3.5 Hydrogen bubble generator

Hydrogen bubbles can be used as flow markers in water flows, as they are very visible when illuminated with a backlight and the drag from the surrounding fluid causes them to follow the flow quite well [44]. They are especially good at identifying vortices because centrifugal actions cause the bubbles to tend to be drawn near the axes of the vortices, where the pressure is minimum. As well, the low turbulence at the vortex cores reduces the diffusion of the bubbles. In this way, bubble lines highlight well the positions and shapes of vortex structures.

Hydrogen bubbles were created by the electrolysis of water. An electric voltage of approximately 300 V was applied to electrodes immersed in the water. Hydrogen bubbles were generated at the cathode and oxygen bubbles were generated at the anode. In the present facilities, a platinum wire with a diameter of 50 μm and a length of 380 mm was used as the cathode. A carbon rod was used as the anode; it was placed so that the oxygen bubbles were out of view of the visualization. Sodium calcite was added to the water to increase its electrical conductivity. A pulse generator was used to control the voltage to the cathode. More information regarding the hydrogen bubble apparatus and pulsing circuit has been provided by Dunn [10].

The bubbles had a sufficiently small diameter for their buoyancy to be negligible. Assuming that the Reynolds number based on the rise velocity is small, the terminal rise velocity of the bubbles can be calculated based on the Stokes expression as:

$$U_g = \left(\frac{gd_b^2}{18\nu}\right), \tag{3.1}$$

where the gravitational acceleration is g $= 9.8$ m/s^2, the bubble diameter is $d_b =$ 25 μm (roughly equal to half the diameter of the wire), and the kinematic viscosity of the water is $\nu = 1.0 \times 10^{-6}$ m^2/s [44]. This leads to a terminal rise velocity of about 0.3 mm/s and a corresponding Reynolds number of 9×10^{-3}. Travelling at an approximate streamwise velocity of 0.16 m/s, the bubbles should rise about 2 mm for every 1 m of downstream travel.

The support probe for the hydrogen bubble wire is sketched in Figure 3.6. This sketch illustrates the small probe, which held a 100 mm long piece of wire, whereas the current experiments use a similar, wider support with a 380 mm long wire. The ends

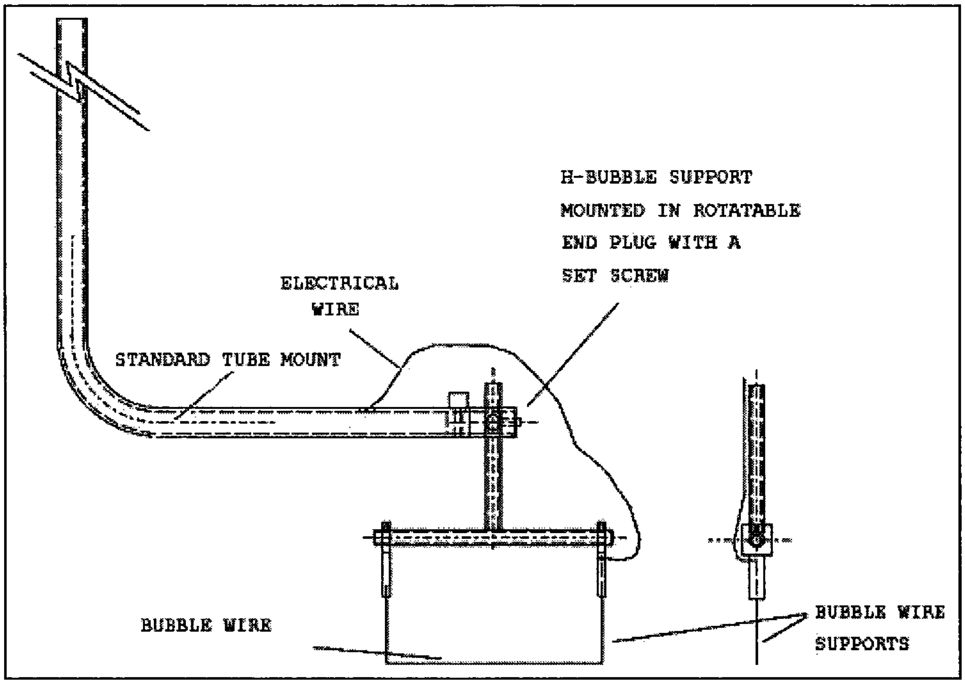

Figure 3.6: Sketch of the support rods for the hydrogen bubble wire [10].

of this wire were wrapped around the two aluminium arms and covered with silicone, which acted as an adhesive as well as insulated the wire from exposure to the water and creating stray bubbles [40]. The end sections of the wire were coated with nail polish in order to restrict all bubble formation to the central section of the probe and avoid the generation of bubbles in the wake region of the probe arms. One end of the wire was soldered to a sheathed wire that ran up the probe holder and back to the power delivery circuitry. Still photos were taken using a Nikon D70 Digital SLR camera with a lens of adjustable focal length in the range of 18-70 mm. Photographs were digitally enhanced using Adobe Photoshop to increase the brightness and contrast of the bubbles compared to the background.

3.6 Laser Doppler velocimetry

Laser Doppler velocimetry (LDV) provided unobtrusive local measurements of flow velocity. The LDV system had a probe head, from which two pairs of laser beams emerged and were focused in the measurement control volume. The same probe

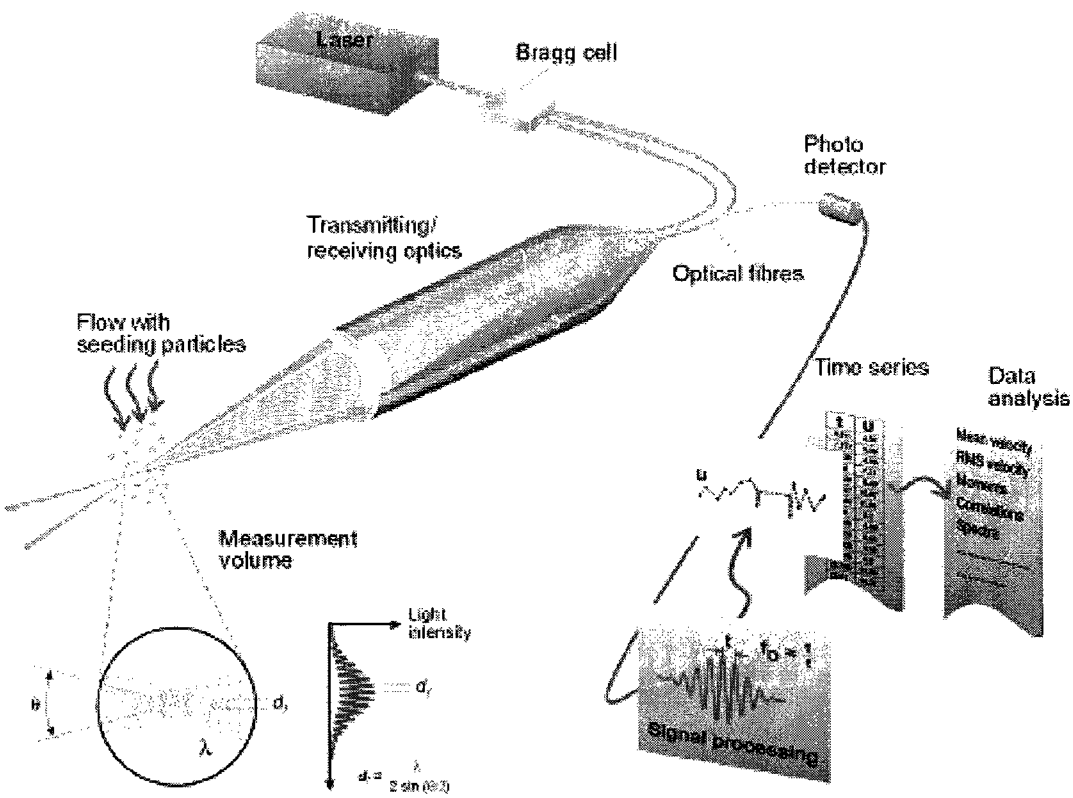

Figure 3.7: Illustration of the principle and basic components of an LDV system. (Reproduced with permission from [6].)

head also received the backscattered light from seed particles passing through the control volume, from which two perpendicular velocity components of the particles were measured. This process is illustrated in Figure 3.7.

The 2D system used presently was supplied by Dantec Dynamics A/S (Skovlunde, Denmark). It used a BSA F50 flow processor in conjunction with Dantec's BSA Flow Software to analyse the measurement signal. Continuous light was supplied by a 5 W Argon-ion laser (model # 95L-5) manufactured by Lexel Laser (Fremont, CA, USA). The laser beam passed through the transmitter (Fibre Flow model # 60×41), which split the beam in two and frequency shifted one of the beams by 40 MHz using a Bragg cell. The two beams were both then split into 488.0 nm and 514.5 nm wavelengths resulting in four beams. Light was transmitted to the probe through fibre optic cables rated at 1 W. A beam expander and a 310 mm focal length lens focused the laser beams, creating a measurement volume in the water with a spanwise depth of 865 μm and a cross-section of approximately 77 μm $\times$ 78 μm. The backscattered light was transmitted through the fibre optic cables back to a distribution box, which separated the colours to be processed by two photomultipliers tubes. These were connected to the processor which sent the data back to the computer.

Though the available tap water seemed to contain plenty of suspended solid particles, additional particle seeding in the water tunnel was necessary in order to maintain a sufficiently high data rate. A mixture of about 0.6 ml of 2 μm diameter silicon carbide spheres, made by TSI (Shoreview, MN, USA), thoroughly dispersed into about 2 litres of water was generally adequate for clear water. This mixture was introduced into the running water tunnel well before taking the measurement to ensure sufficient distribution of the particles in the flow. More seeding was required in later tests, as the particles would eventually settle or were removed by the cleaning filter. Particles of large diameter were deliberately filtered out of the water because they do not follow the flow well, as will be discussed in Section 4.4.2.

3.7 Particle image velocimetry

Particle image velocimetry (PIV) provided two-dimensional instantaneous velocity measurements of the flow. In order to do so, two images of the particles in the measurement plane were taken, one shortly after the other. The velocities in the plane were then calculated from the displacements of the particles during the time separation of the two images. This principle is illustrated in Figure 3.8.

The PIV system was manufactured by LaVision Inc. (Ypsilanti, MI, USA) and used a Solo PIV 120XT laser manufactured by New Wave Research, Inc. (Fremont, CA, USA). This laser is a Nd:YAG dual-cavity laser and can provide up to 120 mJ of power per pulse at a frequency doubled wavelength of 532 nm. A LaVision Imager ProX 4M digital video camera captured the image with a resolution of 2048 $\times$ 2048 pixels. The camera was fitted with a Nikon lens with an adjustable focal length in the range of 18-70 mm and an interference filter that only allowed light in a narrow waveband centred at 532 nm. Using interframing recording, the camera was capable of capturing pairs of images in quick succession. A recording frequency of up to 7.24 Hz was achieved by storing video to the PC RAM, however this could

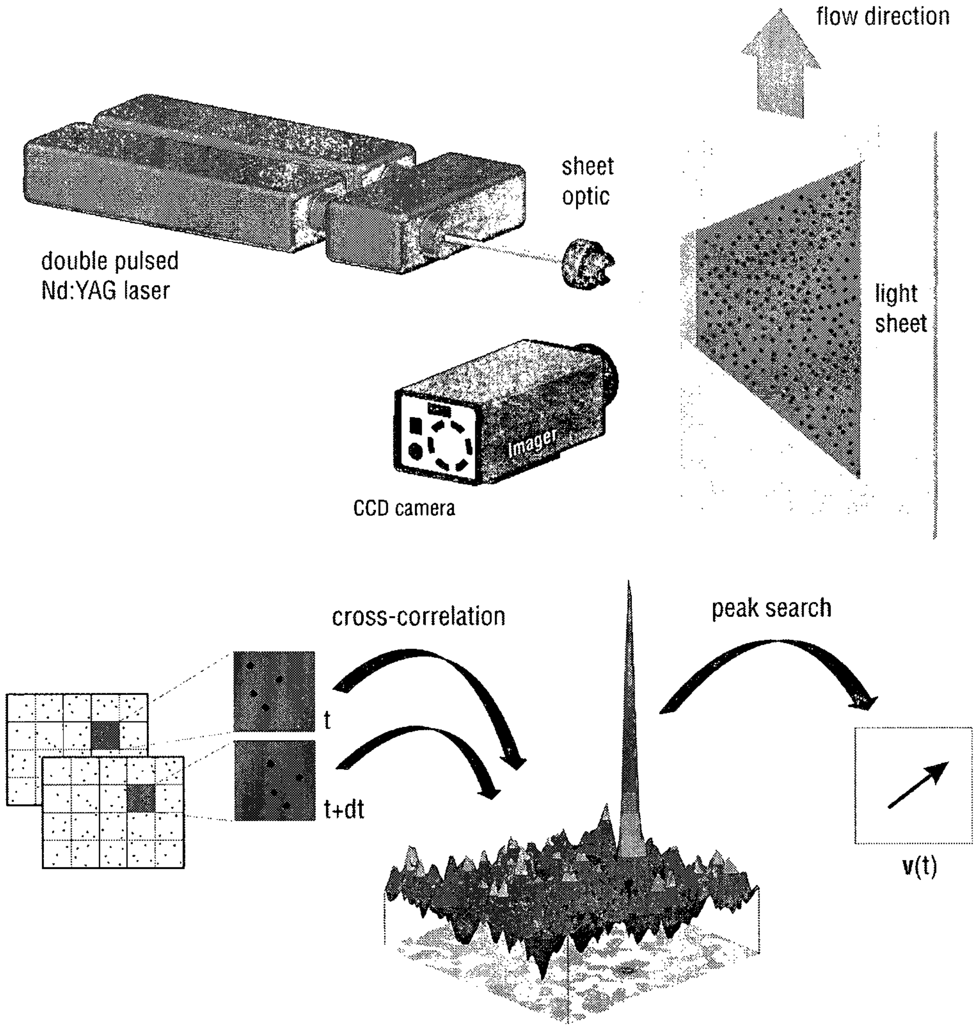

Figure 3.8: Illustration of the principle and basic components of a PIV system. (Reproduced with permission from [25].

only accommodate a capacity of 35 image pairs. For longer recordings, images were transferred directly to the hard drive at a rate of up to 4 Hz. The implementation of a RAID array towards the end of the present work upgraded the data transfer rate to the hard drive array to accommodate full speed measurement rates of 7.24 Hz. A programmable timing unit provided by LaVision synchronised the actions of the camera and the laser.

Several configurations of the equipment were used to obtain data in different planes of the flow. In order to accommodate these multiple configurations, which are described in the following sections, several carts were built to mount the equipment to the water tunnel. A camera mount was manufactured to attach the camera to the existing side cart, as illustrated in Figure 3.9. A new cart for the lower rails was designed to hold the laser, as illustrated in Figure 3.10. A mirror attached to the cart reflected the beam at any desired angle up into the water tunnel. To achieve a horizontal laser sheet, the laser was placed on a table beside the water tunnel. A tripod was used in the configurations that required the camera to be positioned below the water tunnel, looking upwards. The camera was typically placed at a distance of about 500 mm from the measurement plane, resulting in a field of view of the PIV that was approximately 100 mm $\times$ 100 mm.

3.8 Scanning cart system for dye visualisation

A laser scanning system was designed to scan a light sheet through the flow in order to capture the full 3D shape of vortical structures. Rather than illuminating planar sections of the flow as it was convected past the stationary laser sheet, the laser sheet was rapidly traversed towards upstream, effectively illuminating a large volume of the liquid almost instantaneously. Because the PIV-system does not have sufficiently high sampling rate to be used while scanning, the patterns marked by fluorescent dye in the plane of the light sheet were recorded using a high speed camera.

A cart was built to hold the camera and the laser transmission lens rigidly in place relative to each other. This cart (displayed in Figure 3.11) ran along two rails under the water tunnel test section. The cart was set in motion by a falling mass of approximately 9.5 kg, located at the upstream end of the test section. The mass was

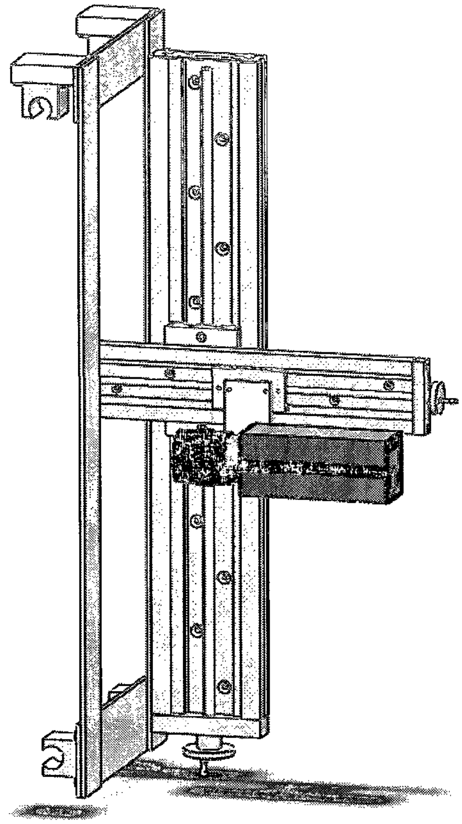

Figure 3.9: Sketch of the PIV camera mounted to the side cart.

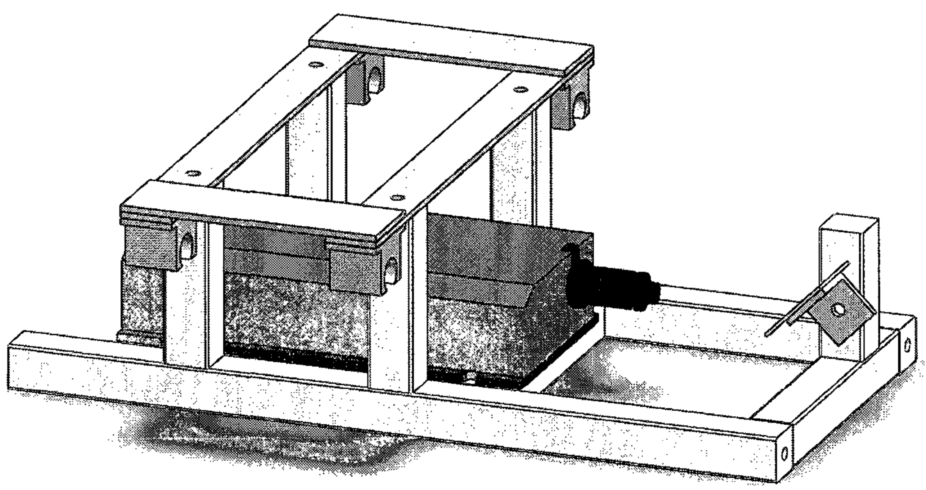

Figure 3.10: Sketch of the laser cart that mounts on the lower rails and the inclined mirror for reflecting the laser sheet up into the water tunnel.

tethered to the cart using steel cable; two pulleys were used to redirect the direction of travel as illustrated in Figure 3.12. The cart was released using a gate latch. When the cart reached the end of the test section, a mounted brake would make contact with a ramp located beside the rails. The gradually increasing friction brought the cart to a stop without significant jolt. The position of the cart during the scan was recorded directly in the video by recording the image of a ruler positioned under the cart and reflected in a mirror within the field of view of the camera.

The light sheet was generated by the same laser as was used for LDV, the 5 W Argon-ion laser. A beam splitter was mounted at the end of the laser before the beam entered the LDV system. This split off about 40% of the laser intensity, which was channeled into a 10 m long fibre-optic cable, rated at 1 W. The fibre-optic cable routed the light to a Powel lens (Oz Optics, ON, Canada) mounted to the scanning cart, which created a light sheet with an approximate thickness of 2 mm. The fibre-optic was long enough such that it was not damaged during the scanning process. The laser sheet had light at two wavelengths, 488.0 nm and 514.5 nm, which were in the correct range to excite the fluorescent dye.

A Fastcam 512 PCI high-speed camera, manufactured by Photron USA, Inc. (San Diego, CA, USA), was borrowed from the University of Ottawa Neurotrauma Impact Research Centre. Through trial and error it was found that a shutter speed of 1/500 s was fast enough to avoid blurring of the image but long enough to allow enough light for sufficient contrast. The corresponding maximum frame rate of 500 frames per second was therefore used for all recordings. In this configuration, the image resolution was estimated at 140 pixels/mm.

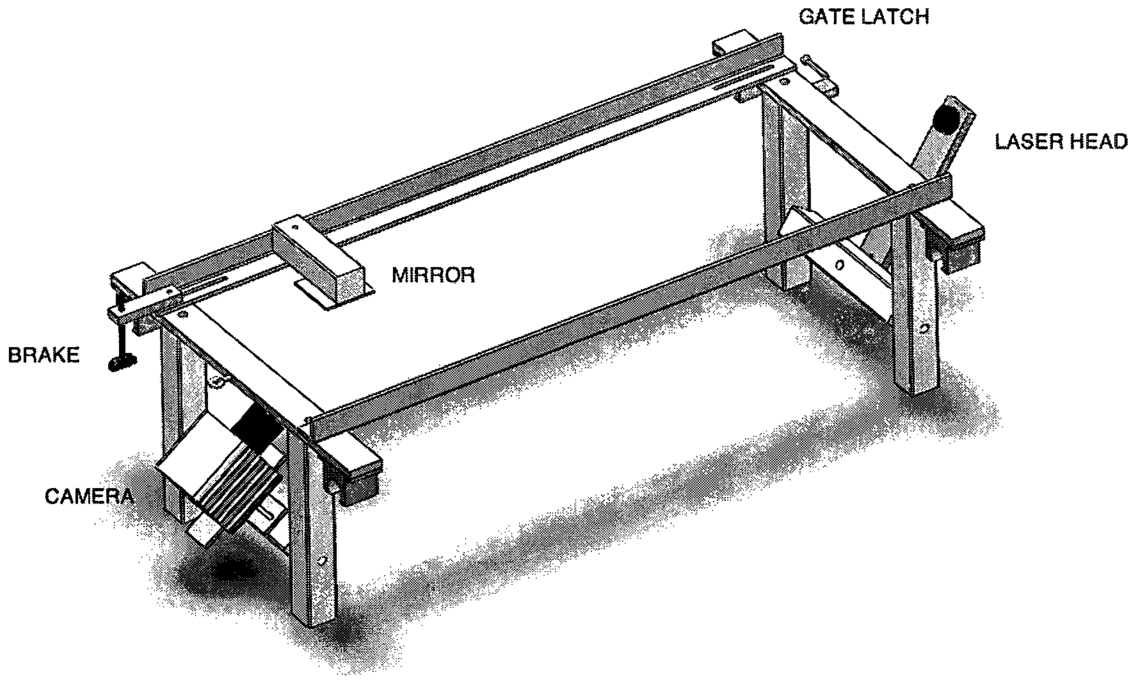

Figure 3.11: Sketch of the scanning cart which carries the laser sheet and camera and runs along two rails under the water tunnel.

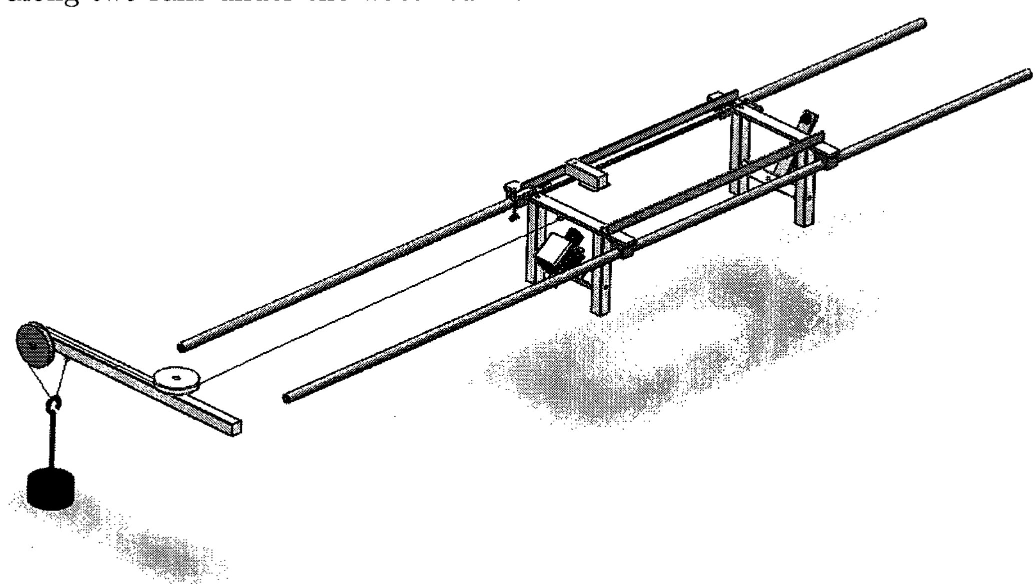

Figure 3.12: Sketch of the scanning cart system mounted on the lower rails and set in motion by a falling weight.

Chapter 4

Experimental procedures

In this chapter, the measurement methods and techniques of analysis are described for the three more complex flow measurement techniques: the LDV, the PIV, and the scanning dye visualisation.

In several cases, more than one methods were used in combination or to measure the same flow property. For example, LDV and PIV were both used to collect time-averaged measurements. Another example is simultaneous PIV and dye visualisation, which allows both qualitative and quantitative characterisation of the flow structures. Moreover, scanning dye visualisation was performed as an extension of the inclined plane PIV measurements, in order to collect more information on how the flow changes in time. These experiments are all described in this chapter.

Most of the analysis of these results was performed using the Matlab programming software distributed by Mathworks (Natick, MA, USA). The computer algorithms that were developed for the analysis of these experiments are explained in this chapter.

4.1 Laser Doppler velocimetry

LDV was the main method that was used for measuring the time-averaged statistics of the flow. LDV has the advantage of requiring relatively short processing time once a Matlab code is prepared to perform the necessary calculations. Measurements at approximately fifty points were possible to acquire and process in one day. Each point measurement was recorded using 'dead-time', which, rather than recording the burst signals of all particles passing through the measurement volume, only samples the particles that are in the volume at a given repeating time interval. This helps to eliminate the velocity bias that results because faster particles dwell less long in the measurement volume than slower ones, allowing a greater population of fast particles to be counted. Both velocity components were measured for each passing particle in 'coincident mode'. Each measurement lasted a minimum of 100 seconds and was composed of a minimum of 1000 samples.

The LDV is also used to calculate the turbulence length scales and Reynolds numbers. For these calculations, in order to maximise the sampling rate, 'burst mode' and 'coincident mode' were used, which record all passing particles that register both velocity components.

The LDV probe was mounted on the side cart and was oriented towards the water tunnel along the x_3 direction, allowing for measurements of the streamwise and vertical velocity components (U_1 and U_2). A Matlab code was written to calculate the statistics for each measurement point. The time-averaged velocity components ($\overline{U}_1$ and $\overline{U}_2$) were calculated from all the samples at the given point. These were then used to obtain the velocity fluctuations (u_1 and u_2) for each sample, from which the turbulent stresses $\overline{u_i u_j}$ were calculated. Outliers that were introduced by the LDV equipment were removed before calculating the second moments. An outlier was defined as a value with a difference from the average of more than four times the standard deviation of the sample, which typically corresponded to about 4 of the 1000 samples collected at a given point.

Vertical velocity profiles at several downstream distances were constructed from sets of point measurements taken along a vertical line in the centre-plane of the tunnel. Similarly the downstream development of the flow was measured from a set of points taken along a streamwise line in the centre-plane of the tunnel.

4.2 Particle image velocimetry

PIV was used to measure the instantaneous velocity fields in a several different configurations. For each configuration, the camera required calibration to measure the transformation between the true displacements of the particles in the measurement plane (in millimetres) and the recorded displacements (in pixels). Two possible calibration techniques were available using LaVision's Davis software, one to account for the scale of the image and one to account for any non-uniform optical distortion in the image. The scale of the image (in mm/pixel) was measured by recording the image of a ruler placed temporarily in the image plane. The calibration to account for any optical distortion was found to be unnecessary for the current configurations as the camera was always positioned with its axis normal to the measurement plane. Furthermore, any distortion due to the glass wall was less than or comparable to the uncertainty of the distortion correction algorithm built into the software.

Vector field extraction was performed entirely by LaVision's Davis software. The raw images were first pre-processed using a background sliding filter to remove any intensity variations in the light sheet. Vector fields were then calculated using multiple passes starting with a window size of 128 x 128 pixels and decreasing to a final window size of 32 x 32 pixels, always with a 50% overlap. Between the passes, in addition to a smoothing algorithm, vectors that did not agree with their neighbours were removed and iteratively replaced so that there would be agreement among neighbouring vectors. Any windows that did not have sufficient particles were assigned a vector calculated by interpolation between the neighbouring vectors; however, if a large fraction of the results required interpolation, the measurements were repeated using higher intensity light or a higher concentration of seed particles. The final result was a vector field of 128 $\times$ 128 vectors for the entire field of view that was 100 mm $\times$ 100 mm. Thus the spatial resolution of the PIV map was approximately 0.8 mm.

4.2.1 Time-averaged measurements

Time-averaged turbulence properties and average velocity profiles were obtained using PIV by time-averaging a large set of at least 100 independent measurements. Measurements were recorded in the $x_1 - x_2$ plane with the camera mounted on the side traverse and the laser mounted on the lower cart. Recordings were collected at a rate of 1 Hz, which corresponds to a sampling interval of several times the timescale of the flow. The field of view was approximately 100 mm by 100 mm. In order to collect measurements over the entire depth of the channel, which is approximately 426 mm, four views were recorded by moving the camera as illustrated in Figure 4.1. The lowest part of the tunnel, within 40 mm from the bottom, was not visible due to blockage from the frame of the water tunnel.

Time-averaging calculations were done in Matlab using the Readimx toolbox from LaVision [25] and the Pivmat toolbox by Moisy [29]. The averages of the two velocity

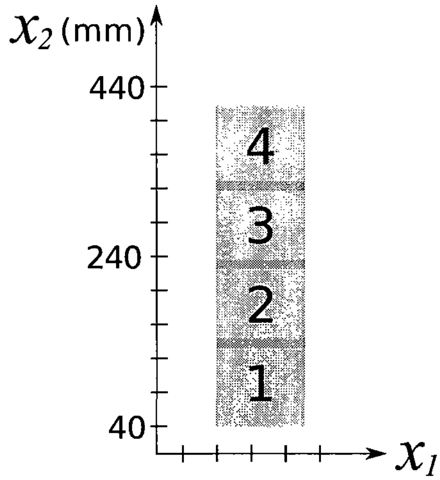

Figure 4.1: Illustration of the measurement configuration for time-averaged measurements with the PIV.

components ($\overline{U}_1$ and $\overline{U}_2$) were calculated for each of the 128 $\times$ 128 vectors in the set of measurements. This resulted in a single average vector field for each of the frames. To obtain the average velocity profile at a given downstream position for the entire depth of the channel, the average velocites corresponding to this x_1 position from all four frames were superimposed at their corresponding x_2 locations. The second moments of the velocity were calculated after the mean was calculated. Calculations included profiles for $\overline{u_1^2}$, $\overline{u_2^2}$, and $\overline{u_1 u_2}$ at a given streamwise position as they varied with channel depth. Note that $\overline{u_1^2}$ corresponds to the variance of the U_1 component of the velocity.

4.2.2 Instantaneous flow fields

Particle image velocimetry was also used to capture instantaneous planar flow fields. The measurement planes provided a 2D cross-section of the flow and the resulting velocity fields were used to identify vortex locations, sizes, and strengths. Because this method only provided information in a single 2D plane at a time, measurements at three different planes were used to provide a more complete view of the structures. These planes, referred to as vertical, horizontal, and inclined, are sketched in Figure 4.2. The vertical configuration used the camera mounted on the side traverse and the laser mounted on the lower cart. The horizontal configuration was realised with the

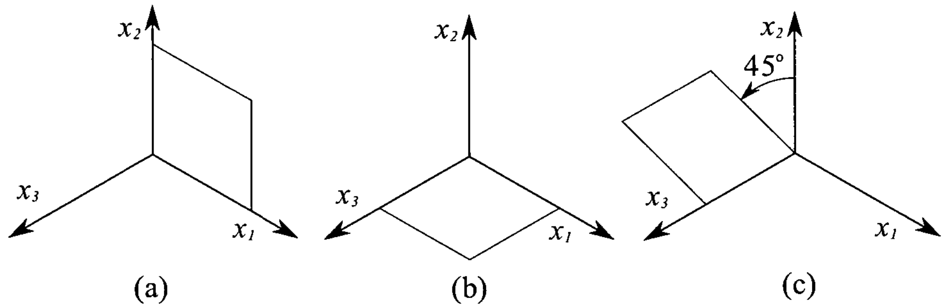

Figure 4.2: Illustration of the three measurement planes for PIV recording: (a) vertical, (b) horizontal, and (c) inclined.

laser positioned beside the tunnel and the camera on the tripod below the tunnel. The inclined laser sheet was achieved by using a mirror for the laser on the lower cart, with the camera tilted upwards at 45° on the tripod under the tunnel.

All of the measurements focused on the fully-developed region near $x_1 = 2.3$ m and $x_2/h = 0.5$, with the exception of some exploratory investigations near the exit of the flow separator in the vertical configuration at $x_1 = 0.10$ m and $x_1 = 0.40$ m. A minimum of 2 sets of 35 images recorded at 7.24 Hz were obtained for each configuration, resulting in at least 70 samples of the flow field.

4.2.3 Traversing PIV measurements

The measurements in the vertical plane were extended in an attempt to track the entire development of a vortex as it was convected downstream. The camera and laser were positioned in the same way as for the vertical stationary PIV; however, each were mounted on separate carts that were traversed together along the length of the test section at a speed of up to 0.2 m/s. The carts' motion was manually started as soon as the PIV recording began and their speed was adjusted to match the convection velocity of the flow at a level with $x_2/h = 0.41$. Thirty-five images were recorded at 7.24 Hz and the process lasted for about 5 seconds.

The relative velocity of the cart with respect to the flow velocity was estimated from the mean velocity of each frame measured by the PIV system. Depending on the timing of the start of the measurement, up to the first five frames of the measurement were discarded because the cart was found to accelerate during that

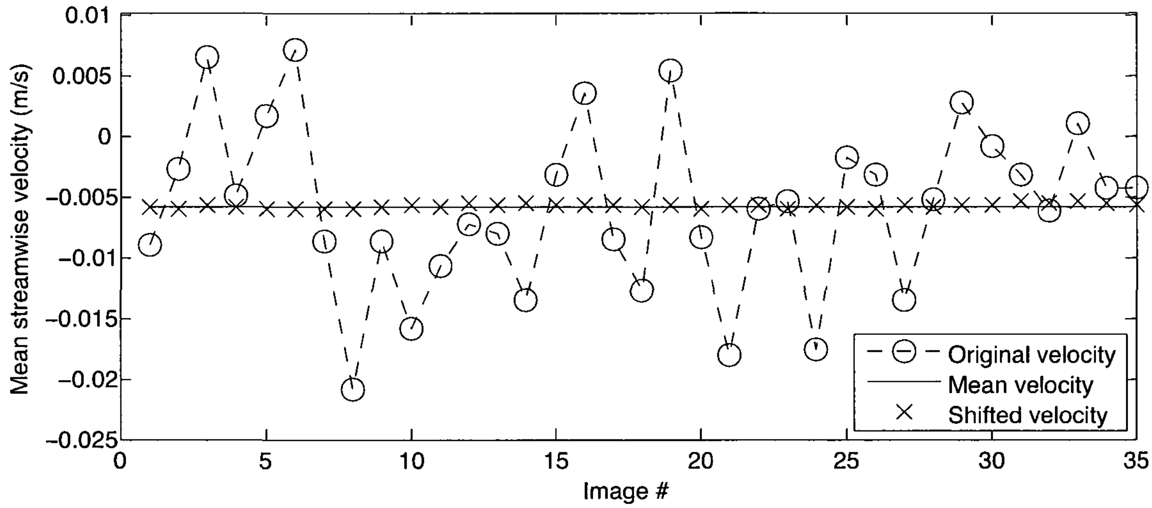

Figure 4.3: Comparison of the original measured velocities of the traversing cart to those corrected for the cart jitter.

time. Afterwards, the cart velocity was not constant, but exhibited small irregular fluctuations of an amplitude of about 0.01 m/s, as illustrated in Figure 4.3. To correct for this jitter, each velocity vector field was shifted by the amount that its mean differed from the mean velocity of the entire set. Next, to improve the continuity between frames, starting with the second frame, the vector fields were shifted by the amount that minimised the sum of the differences between each individual vector and the corresponding vector of the preceding frame. This second shift was typically very small, and the resulting velocity fields all had a mean velocity very near the mean velocity of the set, as shown in Figure 4.3. This uniform shift in the velocity fields did not effect the calculation of vorticity or of swirling strength, which depend on the gradients of the velocity field and are independent of translation.

4.2.4 Simultaneous PIV and dye visualisation

Planar dye patterns where used to complement simultaneous PIV measurements in the inclined plane. The same laser sheet was used for both PIV illumination and to excite the dye. The advantage of using dye injection and PIV at the same time is that the dye images identified areas of interest, which were then examined using PIV. This also allowed comparison with the results of Kislich-Lemyre [23], which only used dye injection. However, the dye patterns that indicated swirling flow did not always correspond to vortices as identified by the PIV vector fields. These patterns were the remnants of swirls that were generated by vortices upstream of the field of view of the PIV [18]. These misleading dye patterns may explain any discrepancies between the current PIV results and flow visualisations. The dye injection did not interfere with PIV measurements, as confirmed by tests performed with and without dye.

4.2.5 Vortex identification algorithm

The velocity field and swirling strength maps were used to identify vortices in the flow. Following the method suggested by Gao et al. [14], it was assumed that vortices were present at the locations of peak swirling strength. Only peaks with $\lambda > 0.05\lambda_{max}$, where λ_{max} was the maximum swirling strength in the flow field, were considered. The presence of vortices at these locations was confirmed visually by verifying that the velocity vectors within their proximity indicated a swirling motion, when considered relative to the vortex's convection speed, as suggested by Robinson [34].

The areas of the vortex cores were determined by using an area growing algorithm starting at each peak of swirling strength. This algorithm identified the extent of the vortex core as the coincident region with a swirling strength greater than $0.025\lambda_{max}$ (see Figure 4.4). In most cases, this approach made it possible to separate discrete vortices, especially those of opposite vorticity as the swirling strength vanishes when the vorticity changes sign. This method, however, sometimes allowed neighbouring vortices of similar vorticity to be connected and so be identified as parts of a single vortex. In cases such as this, even though the vortex core contained two peaks, if they were not separated by a region where the swirling strength was less than $0.025\lambda_{max}$, they would be considered a single entity.

The properties of each of the identified vortices were then calculated and recorded. The convection speed of each vortex was found by averaging the absolute velocity over the area of the vortex core as identified by the coincident region with swirling strength greater than $0.025\lambda_{max}$. Each vortex's circulation strength was calculated by integrating the local vorticity over the area of the vortex core. The measured vorticity magnitude was only that of the component which was normal to the plane of the

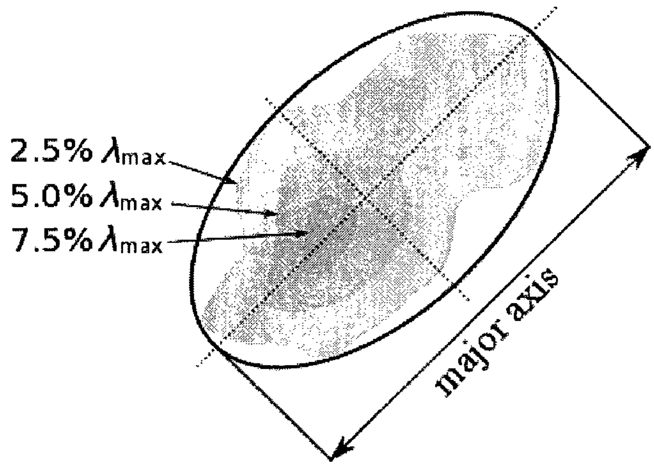

Figure 4.4: Sketch of the contours of swirling strength identifying a vortex. The peak is greater than 5% of λ_{max} and the area of the vortex core is defined as the region with swirling strength greater than 2.5% of λ_{max}. The minimum-area ellipse enclosing the area of the vortex is identified.

measurement. The vortex's diameter was defined as the major axis of the smallest fitted ellipse that enclosed the area of the vortex core (refer to Figure 4.4). The minimum-area enclosing ellipse was calculated using a MATLAB algorithm written by Moshtagh [31] based on the Khachiyan algorithm.

The preliminary set of vortices identified in each of the time frames was then screened in order to reduce the effect of noise and to remove the weaker vortices. All vortices that were identified but could not be followed in one of the two adjacent time frames were discarded. The change in position of the vortex based on its convection speed was accounted for. Additionally, the vortex was allowed to change in size or strength by up to 50%. This screening successfully removed most of the small vortices that were indistinguishable from noise and had a strong effect on the probability distributions of the strength and size of the vortices. Nevertheless, the removal of small vortices is not disconcerting because it is the large scale structures that are of interest in this study. For the statistical analysis of the vortices, a single vortex appearing in two consecutive frames was counted as two separate occurrences. This allowed vortices with longer lifetimes to be weighted more heavily and so to obtain a more representative statistical distribution.

The sensitivity of the vortex identification algorithm on the choice of swirling strength threshold values was briefly investigated. After testing a range of thresholds for the minimum peak swirling strength, $0.05\lambda_{max}$ was found to be the optimum value to exclude those peaks of swirl that may be deemed to represent noise, while still being able to track a wide range of vortex strengths. Doubling the threshold values had a small effect on the resulting statistics: the mean vortex diameter was reduced by about 10%, however the mean vortex strength remained about the same because the decrease in strength of the large vortices was balanced by the removal of the smaller vortices that did not exceed the threshold limit. A peak threshold of $0.05\lambda_{max}$ and a lower threshold of $0.025\lambda_{max}$ were used in all cases considered.

4.2.6 Vortex pairing algorithm

Pairs of counter-rotating vortices were observed in both the horizontal and the inclined planes. Unfortunately, it was difficult to determine with consistency from the PIV vector fields which vortices belonged to a pair. In an attempt to alleviate this problem, an algorithm was developed by the author to automatically pair counter-rotating vortices without human bias, based on closeness in strength and convection velocity, and physical proximity. This algorithm was applied to the separate time frames and first separated the clockwise and counter clockwise vortices into two lists. It then analysed sequentially all possible connections, assigning an associated cost to each pair based on their difference in absolute strength S (in m^2/s), convection velocity Vx and Vy (in m/s), and positions x and y (in m), following the formula

$$Cost_{\alpha,\beta} = A_{\alpha,\beta} + B_{\alpha,\beta} + C_{\alpha,\beta} + D_{\alpha,\beta} \tag{4.1}$$

where

$$A_{\alpha,\beta} = 50 \times \frac{|(S_\alpha) - (S_\beta)|}{max(|S_\alpha|, |S_\beta|)} \tag{4.2}$$

$$B_{\alpha,\beta} = 500 \times \frac{\sqrt{(x_\alpha - x_\beta)^2 + (y_\alpha - y_\beta)^2}}{max(|S_\alpha||S_\beta|)} \tag{4.3}$$

$$C_{\alpha,\beta} = 1000 \times |Vx_\alpha - Vx_\beta| \tag{4.4}$$

$$D_{\alpha,\beta} = 1000 \times |Vy_\alpha - Vy_\beta|, \tag{4.5}$$

and the subscripts refer to the two vortices in question, and x and y are the directions of the axes in the frame of reference of the PIV measurement. The coefficients used

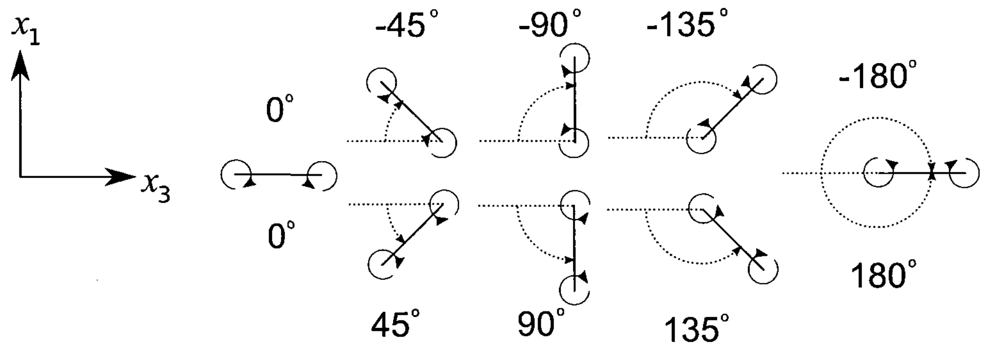

Figure 4.5: Sketch illustrating the calculation of the inclination of the vortex pair based on the relative position of the clockwise vortex to the counter clockwise vortex with respect to the $x_1 - x_3$ axes (or in the case of the inclined plane, the $x_1 cos(\theta)$ and x_3 axes.

in this formula were selected by trial and error. The pair of vortices with the lowest cost was identified as a valid pair and removed from the two lists. The algorithm then re-analysed all possible remaining connections, and selected the pair with the next lowest cost. The algorithm repeated this process until no pairs had a cost lower than a set threshold of 80. All characteristics of the valid pairs were recorded so that the orientations of the pairs and other properties could be analysed statistically. The inclination of each pair with respect to the $x_1 - x_3$ axes (or in the case of the inclined plane, the $x_1 cos(\theta)$ and x_3 axes) was calculated based on the relative position of the clockwise vortex to the counter clockwise vortex, as illustrated in Figure 4.5.

4.3 Scanning dye visualisation

The dye images recorded with the use of the scanning cart were analysed visually to identify recurring dye patterns. The high speed images had relatively low brightness and contrast, which made the use of computer vision algorithms quite difficult. Structures were identified at the locations showing swirling dye patterns that remained coherent in several frames. Wherever possible, the direction of rotation of the vortex was inferred from the direction of induced flow in the proximity of the vortex.

Each frame sequence containing the coherent vortex signature was further analysed by reconstructing the dye pattern in three-dimensional space. The location of each pixel in the frame sequence was defined by its two-dimensional position (x', y') in the

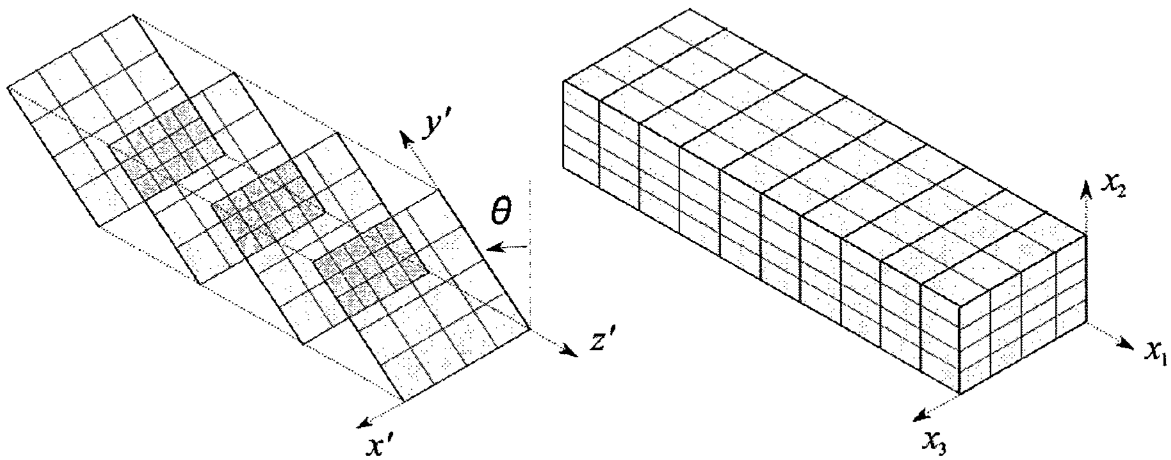

Figure 4.6: Sketch of the transformation from the scanned inclined planes to a 3D voxel array.

frame of reference of the inclined plane and by the number of the frame that contained it, which was identified by the downstream position of the lower corner of the frame z'. The values of the pixels in this non-orthogonal and non-uniform array defined by (x', y', z') were resampled into an orthogonal three-dimensional array of voxels (volumetric pixels) filling the entire measurement volume with coordinates associated with the (x_1, x_2, x_3) positions in the water tunnel test section. As Figure 4.6 shows, the two coordinate systems where related as

$$x_1 = z' - y' \sin(\theta) \tag{4.6}$$

$$x_2 = y' \cos(\theta) \tag{4.7}$$

$$x_3 = x' \tag{4.8}$$

The spacing of the array in the x_2 and x_3 directions was chosen to be consistent with the pixel positions in the inclined frame. This allowed the resampling process to be strictly one dimensional along the aligned x_1 and z' axes. The values for each voxel were calculated for constant values of (x_2, x_3) at a time by interpolating between the values in the corresponding (x', y') coordinates of the nearest inclined planes.

The voxel array was exported from Matlab using the NIfTI and Analyze toolbox by Shen [38]. It was analysed using ITK-SNAP (www.itksnap.org), which is open-source software that was designed for 3D segmentation of MRI or X-ray measurements in the medical field and uses the Neuroimaging Informatics Technology Initiative (NIfTI) standard format. The software accommodates manual and automatic segmentation based on image intensity. For extracting vortices, segmentation was performed by manually shading the appropriate areas outlined by the swirling dye patterns. The 3D mesh was then viewed using ParaView (www.paraview.org), an open-source scientific visualisation software based on the Visualization Toolkit (www.vtk.org).

4.4 Uncertainty estimates

4.4.1 Uncertainties associated with the water tunnel operation and the positioning systems

Previous work in the water tunnel by Dunn [10] and Menu [28] identified some uncertainty associated with the reproducibility of the flow in this facility. Dunn measured the variation of the flow velocity over the cross-sectional area for uniform flow to be 1% of the mean velocity. He also examined the effect of surface waves on the flow velocity. Menu showed that these small changes in the water level result in a sinusoidal fluctuation of the mean velocity signal. The period of the fluctuation was measured at 11 $\pm$ 1 seconds independently of the flow rate. For a centreline velocity near 0.15 m/s, the amplitude of the fluctuation was measured at 0.0015 m/s or 1%.

The uncertainty of the positioning of the measurement probes is also worth discussing. The accuracy of vertical positions in the x_2 direction was equal to that of the vertical stage, which was a fraction of one millimetre. The streamwise positions in the x_1 direction were measured by eye using a tape measure mounted to the side of the test section and had an estimated total uncertainty of 10 mm, due to the sum of the uncertainties of the positioning of the ruler, the measurement of the position of the cart, and the measurement of the distance between the centre of the probe and edge of the cart. Using the properties of the USF measured in Section 5.1.1, this streamwise position uncertainty translated to an uncertainty of 0.03 in the dimensionless downstream position τ. Because of the constraints imposed by the side walls of the water tunnel and the presence of the water, direct measurements of the spanwise position in the x_3 direction were difficult. The spanwise position of points in the water were inferred by measuring the extrapolated spanwise positions above and under the tunnel. In the case of the vertical laser sheet used for PIV, which was shone up through the bottom glass window of the test section, a piece of paper was inserted in the beam's path under then above the tunnel to measure its spanwise position. For this reason, the spanwise positional uncertainty was estimated to be about 10 mm. Dunn showed that the velocity varied less than 1% in the spanwise direction and Kislich-Lemyre [23] showed that the turbulent properties of USF were also roughly uniform in spanwise direction; therefore, the propagated uncertainty of the flow properties due to the spanwise position uncertainty was expected to be small. Nevertheless, an improved positioning method catering to the new PIV system would be a suggested improvement for future experiments.

4.4.2 LDV uncertainty

Much of the error related to the LDV measurements was to the aforementioned positional accuracy of the probe. Furthermore, the spanwise length of the LDV measurement volume is 865 μm, which means that the velocity signal was averaged over this distance. These two effects limited the accuracy of the desired point measurement.

Other than the positional accuracy, the greatest source of error is caused by the possible differences between the velocity of the light-scattering particles and the velocity of the surrounding fluid. Tracer particles are subject to drag when there is a relative motion between the particle and the fluid. There is also a vertical relative velocity when the particle density is different from the fluid density. The terminal velocity U_g of small, heavy spherical particles can be estimated by the expression provided by Raffel [33], where d_p is the diameter of the particle, ρ_P and ρ are the densities of the particles and the fluid respectively, and μ is the viscosity of the fluid.

$$U_g = d_p^2 \times \frac{(\rho_P - \rho)}{18\mu} \times g \tag{4.9}$$

For the silicon carbide seed particles used here, $d_p \approx 2$ μm, from which one estimates that $U_g = 5 \times 10^{-6}$ m/s. However, foreign particles of a diameter up to 30 μm, corresponding to the rating of the water filter, may be present in the flow. Assuming a density similar to that of the seed particles, these foreign particles would exhibit a terminal velocity of about 1×10^{-3} m/s. The time constant of the particle-fluid interaction τ_S is given by Tavoularis [44] as

$$\tau_S = \frac{\rho_P d_p^2}{18\mu}\left(1 + \frac{1}{2\gamma}\right), \tag{4.10}$$

where the particle-to-fluid-density ratio is $\gamma = \rho_P/\rho_f$. This time constant is about 0.82 μs for the seed particles, but is about 186 μs for the largest possible foreign particles. The maximum frequency of the fluid motion at which the particle will still follow the velocity fluctuations can also be estimated. Based on the chart by Tavoularis, the 3-dB cut-off frequency of the seed particles is about 1000 kHz, compared to about 3 kHz for the foreign particles. The maximum sampling rate of the LDV was roughly 0.5 kHz. These results illustrate that the seed particles would have followed the flow quite well and would have had negligible contribution to the measurement uncertainty. Foreign particles, on the other hand, could have contributed to the measurement uncertainty.

Another source of error in the LDV measurements was the velocity bias. This term describes the bias of the mean velocity measurement towards higher velocities, as a greater proportion of fast particles cross the measurement volume than slow particles. An estimate of the magnitude of the velocity bias in turbulent flows is provided by Tavoularis [44] as

$$\frac{\overline{U_m}}{\overline{U}} \approx 1 + \frac{\overline{u^2}}{\overline{U}^2} = 1 + \left(\frac{u_1'}{U_c}\right)^2 \tag{4.11}$$

where U_m is the measured velocity and U is the actual velocity. For the typical value of $u'/U_c = 0.05$ in the present flow, the velocity bias ratio would be 1.0025. This was further reduced by using the LDV in 'dead-time' mode, which did not take into consideration all particles but instead sampled the flow at regular intervals. This produced a more random sampling of the flow particles but reduced the data rate.

The LDV signal was also found to randomly contain large outliers, which were many standard deviations away from the average. The cause of these outliers is unknown, but it is deemed to be unrelated to the measurement of particle velocities because the corresponding velocities were outside the range of values that were possible for this flow. These outliers were easily removed and had no effect on the flow measurements.

4.4.3 PIV uncertainty

Uncertainty can effect the PIV velocity measurements at three stages of the measurement process. Firstly, systematic error may be introduced in the calibration stage if the measured scale does not equal the true scale of the plane. Secondly, systematic and random errors may result in the measurement of the time separation or the imaging of the displacement of the particles, for example by out-of-plane motion of the particle or a misalignment of the camera recording plane and the measurement plane. Last of all, some random error is inherent in the cross-correlation calculations for extracting the particle displacements from the image, especially if particle and fluid densities are not ideal.

All of these considerations as well as uncertainty estimate procedures are outlined by the International Towing Tank Conference (ITTC) Guide for the Uncertainty Analysis of PIV [41]. These errors each effect either the particle displacement ΔX, the magnification factor α, or the time separation Δt, used in the calculation of the velocity vector U by the equation

$$U = \frac{\alpha \times \Delta X}{\Delta t} \ . \tag{4.12}$$

The errors in the estimation of these three factors are propagated to the uncertainty of the velocity as

$$\frac{\delta U}{|U|} = \sqrt{\left(\frac{\delta\alpha}{\alpha}\right)^2 + \left(\frac{\delta(\Delta t)}{\Delta t}\right)^2 + \left(\frac{\delta(\Delta X)}{\Delta X}\right)^2} \ . \tag{4.13}$$

For a typical mean velocity of $U = 0.15$ m/s in the present experiements, nominal values of these factors are $\alpha = 0.055$, $\Delta t = 5000$ μs, and $\Delta X = 14$ pixels.

Magnification α

Uncertainty in the magnification ratio α between the image size in pixels l_r and the true length on the measurement plane in millimetres L_r is introduced in the calibration stage. The magnification is measured by inserting a ruler into the image plane; typically the spacing read on the ruler is about $L_r = 90$ mm, and the corresponding image size is $l_r = 1640$ pixels. There are multiple sources of error in this calibration, which are highlighted by the following:

- The image distortion by the abberation of lenses could be up to 0.5% of the image length.

- The discretisation of the image into discrete pixels could add an error of about 0.5 pixels, or 0.03% of the image length.

- Human error in selecting the correct pixel in the software could be up to 2 pixels, or 0.1% of the image length.

- Incorrect placement of the ruler so that the ruler is at a different depth than the measurement plane could cause the ruler to appear larger or smaller than it is. This error can be estimated using similar triangles, so that the fractional error is equal to twice the ratio of the error in depth Δz to the actual distance from the camera to the measurement plane l_t. In this case the plane may be off by up to 10 mm and the approximate distance from the camera to the measurement plane is 500 mm, resulting in an uncertainty of 4%.

- Incorrect alignment of the ruler to the image plane would introduce perspective error on the reading of the ruler. If the ruler were tilted by 5°, the true length would be shortened by $1 - \cos(5°)$ or 0.4%.

Summing these fractional uncertainties we obtain a maximum expected bias of the magnification of 5%.

Time Separation of Pulses Δt

The time separation of the two pulses is triggered and recorded by the timing unit, which has an uncertainty of 5 ns, according to the LaVision manual. Furthermore, the duration of the two pulses contributes an uncertainty of 2×5 ns as the particle may be captured at any point during the pulse. These combined uncertainties result in a precision of 0.0001% from the total average time separation of 5000 μs, which is entirely negligible.

Displacement of Particles ΔX

Uncertainty in the measurement of the displacement of the particles can be caused by the finite thickness of the 2D sheet, during the recording of the particle images to the camera, or during the cross-correlation calculations. Factors contributing to these processes are:

- Out of plane motion of the particle cannot be measured and would result in an underestimation of the true particle velocity magnitude. For the vertical and horizontal configurations, this out-plane motion is less than 1% of the streamwise velocity, and therefore the velocity vector is at most misaligned by an angle of 0.6°, and the particle displacement would be foreshortened by only 0.005%. In the case of the inclined plane, the plane is misaligned to the streamwise velocity by 45°. This results in a particle displacement shortened by 40%, which can be corrected for rather than being considered as uncertainty.

- This effect of the out-of-plane motion would be doubled when the measurement plane was not parallel to the flow direction as intended. For a maximum estimated misalignment of 5° and would result in a shortened velocity by 0.4%.

- A misalignment of the camera to the measurement plane away from 90° would also result in an underestimation of the true particle displacement. A misalignment of 5° the measured velocity would be lower by 0.4%.

- The correlation process is not perfect and contributes to the uncertainty of the calculated particle displacement as well. The ITTC suggests that an average random error of 0.2 pixels would be due to the potential mismatching of particles. An additional systematic error due to the discretisation of particles into discrete pixels, referred to as 'peak-locking', contributes another 0.1 pixels to the uncertainty. This totals to a fractional precision of 2%.

- The ability of the particles to follow the flow was discussed for the LDV measurements and similarly applies to the PIV measurements. While the seed particles were found to follow the flow well, foreign particles up to a diameter of 30 μm would exhibit a terminal velocity of 1×10^{-3} m/s, which corresponds to a precision uncertainty of about 1%.

Considering all of the above sources of error, the particle displacement would have a total fractional uncertainty of 4% for an average particle displacement of 14 pixels. This can be decomposed into a precision of 3% and a bias of 1%.

Propagation of error to the velocity U and further derivatives

Using the previously found uncertainties, one may use Equation 4.13 to estimate the velocity bias limit at about 5.1% and a precision limit at about 3%, for a total velocity uncertainty of about 6%, at a 95% confidence level. The low-pass smoothing filter that was applied to the vector field during processing drastically decreases high-frequency random errors, thus further decreasing the precision uncertainty.

By averaging a large amount of velocity measurements, the precision limit may be reduced. The uncertainty in the mean value is reduced by $1/\sqrt{N}$, where N is the number of samples [44]. For the time-averaged measurements, 100 samples were used, which reduces the precision uncertainty to 0.3%. The bias uncertainty, however, remains at 5.1%.

The propagation of the velocity error to the velocity derivatives depends on the differentiation scheme. LaVision uses a central difference scheme with the four closest neighbours. Raffel [33] suggests that the central difference scheme results in an uncertainty of the velocity derivative of $0.7\epsilon_u/\Delta x$, where Δx is the spacing between adjacent vectors and ϵ_u is the velocity precision uncertainty as the bias uncertainty of the velocity does not contribute to the derivative. For the present case, the uncertainties of the derivatives of U_1 are about 4 s^{-1}, and those of U_2 are about 0.2 s^{-1}. Using these results, the uncertainties of the vorticity and of the swirling strength may be estimated. The vorticity is calculated as

$$\Omega = \frac{dU_2}{dx_1} - \frac{dU_1}{dx_2}. \tag{4.14}$$

The uncertainty of the vorticity is therefore

$$\delta\Omega = \sqrt{\left(\delta\frac{dU_2}{dx_1}\right)^2 + \left(\delta\frac{dU_1}{dx_2}\right)^2}, \tag{4.15}$$

which results in a value of 4 s^{-1} in the present case. The calculation for swirling strength [25] uses all four velocity derivatives as

$$\lambda = max\left(0, -\left(\frac{dU_1}{dx_2}\times\frac{dU_2}{dx_1} - \frac{1}{2}\left(\frac{dU_1}{dx_1}\times\frac{dU_2}{dx_2}\right) + \frac{1}{4}\left(\frac{dU_1}{dx_1}^2 + \frac{dU_2}{dx_2}^2\right)\right)\right), \quad (4.16)$$

such that the uncertainty equation is

$$\delta\lambda^2 = \left(\frac{dU_2}{dx_1}\times\delta\frac{dU_1}{dx_2}\right)^2 + \left(\frac{dU_1}{dx_2}\times\delta\frac{dU_2}{dx_1}\right)^2 + \left(\left(\frac{1}{2}\frac{dU_2}{dx_2} + \frac{1}{2}\frac{dU_1}{dx_1}\right)\times\delta\frac{dU_1}{dx_1}\right)^2 + \left(\left(\frac{1}{2}\frac{dU_1}{dx_1} + \frac{1}{2}\frac{dU_2}{dx_2}\right)\times\delta\frac{dU_2}{dx_2}\right)^2. \quad (4.17)$$

Assuming the typical maximum magnitudes of the velocity derivatives observed in this flow were about 2 s^{-1}, except for dU_1/dx_2 which was about 4 s^{-1}, the maximum uncertainty of the swirling strength was about 11 s^{-2}. The uncertainties of both the vorticity and the swirling strength are on the same order as the mean absolute magnitudes of these values measured in the USF, which causes some concern about the quality of the results. However, these uncertainties should be considered as over-estimates because they depend on the vector spacing Δx, which was effectively increased when the velocity results were smoothed during processing.

In addition to the velocity uncertainty, the PIV also fails to capture the small motions of the turbulent flow due to the resolution of the measurements. The result of the correlation calculations is an 128 × 128 vector field, corresponding to an approximate area of 100 mm × 100 mm. Each vector therefore represents an area of 0.8 mm × 0.8 mm. Any motions smaller than this scale cannot be resolved, and the smallest identifiable vortex requires four encircling vectors and would therefore have a minimum diameter of 1.6 mm. This limits the range of vortex diameters that can be measured in this flow.

4.4.4 Uncertainty of the scanning system

The laser scanning method has been used previously in experimental fluids dynamics. Kelso and Delo [40] suggest that the most significant source of uncertainty is the positioning accuracy of the laser sheet. In the present case, the position of the cart was recorded directly in the image, using the reflection of a ruler aligned with the streamwise direction. Uncertainty in this measurement could be introduced by vibration of the mirror, which would misalign the image of the ruler, or by limitations in reading the ruler in the video image. It is deemed that the second effect was the dominant source of uncertainty, which was estimated to be about 2 mm.

The assumption of the 'frozen' flow needs to be evaluated. The speed of the cart was at least 10 times higher than the flow speed. To further increase its relative velocity, the cart was traversed against the flow. In the 1 second that the cart took to traverse 1 m, the flow would have been convected downstream by only 0.10 m. This would result in recordings of the fluid volume to appear shorter than the actual one by 10%. The cart displacement in the x_2 and x_3 directions was many times smaller than the streamwise movement, and so the uncertainty in these directions is negligible.

Finally, the choice of the recording rate of the camera also strongly affects the quality of the results. This was set as a trade-off between long exposures, which allow as much light into the camera as possible, and short exposures, which avoid image blurring and can be repeated in rapid succession for increased streamwise spatial resolution. In the present case, images were recorded at 500 frames per second, as slower rates resulted in blurred images, and images recorded at faster rates were much too dark. Even so, images recorded at 500 frames/s had a brightness that did not cover the entire light intensity range of the CCD, despite efforts to increase the laser light intensity and to use higher concentrations of dye. This means that even when the images were digitally enhanced to increase the range of brightness to the full possible range, the resolution of the values of the pixels was still poor. This poor resolution affected the sharpness of the outlines of the dye pattern, limiting the ability to distinguish flow structures.

Chapter 5

Results

This chapter has been divided into four sections representing the four experimental methods employed in this study. The first section presents the time-averaged measurements, which were measured predominantly with LDV, though for some measurements PIV was used as well. The second section presents the results of the scanning dye visualisation, namely the three-dimensional dye patterns recorded using a scanning light sheet. Next, the flow visualisation results using hydrogen bubbles are presented. Lastly, the PIV results are presented, which include examples of the measured instantaneous flow fields as well as summaries of the properties of the vortices in three characteristic planes.

5.1 Time-averaged measurements

Time-averaged velocity profiles have been measured using LDV and PIV in order to document the flow characteristics and permit a comparison to previous studies of USF as summarised in Chapter 2.2.2. The LDV was further used to acquire estimates of the length scales and the turbulent kinetic energy of the current USF.

5.1.1 Velocity measurements

Using LDV, velocity profiles at several downstream positions were constructed from sets of at least twelve point measurements taken along a vertical line in the centreplane of the tunnel. These point measurements were collected using the 'dead-time' mode and consisted of at least 1000 samples. With PIV, the 2-D mean velocity variation was calculated by averaging 100 independent flow fields.

Multiple flow measurements were conducted to determine the effect of adding an endplate at the end of the test section and the effect of adding rods at the exit of the flow separator. The endplate introduced blockage to the flow at the bottom of the

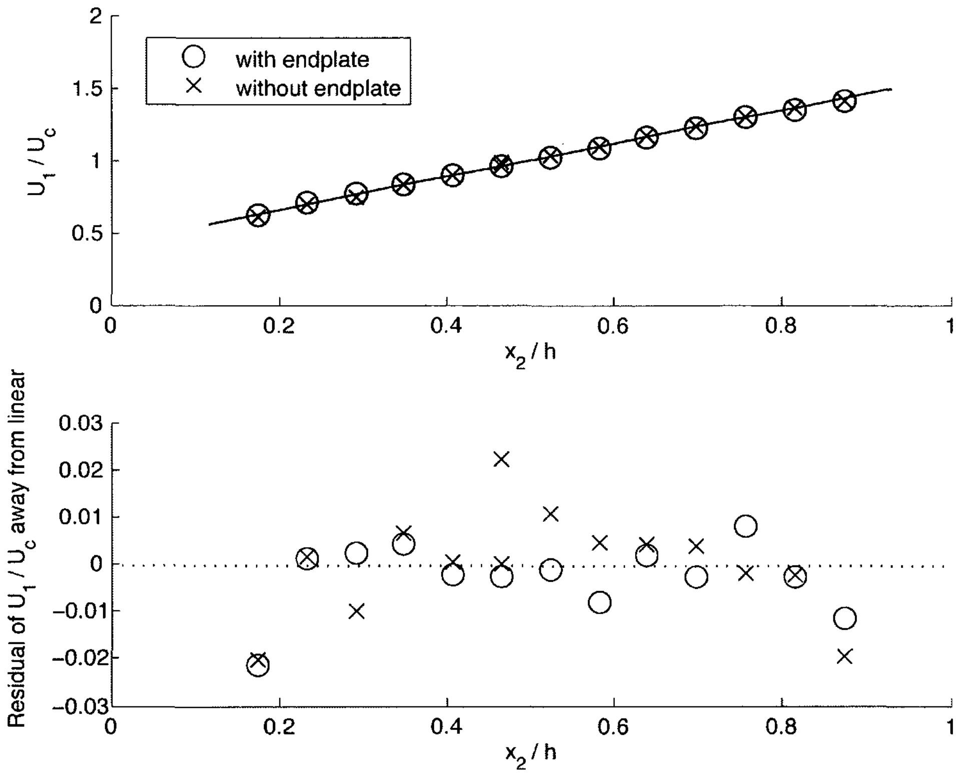

Figure 5.1: Comparison of the mean velocity profiles near the end of the test section ($x_1 = 3.5$ m) with and without the endplate.

tunnel, which compensated for the suction of the drains in the floor of the recovery tank. The LDV was used to measure the velocity profile of the flow at a position with $x_1 = 3.5$ m and $x_3 = 0$, both with the endplate in place and without it. Figure 5.1 illustrates that the velocity profiles in both cases were close to being linear and that the endplate generally decreased the differences ΔU_1 between the measured values and the fitted linear function. With the endplate, these differences were less than 1% in the core of the flow ($0.2 < x_2/h < 0.8$). For this reason, the endplate was used for all further studies.

A summary of the LDV measurements taken at three downstream positions is presented in Table 5.1 for the cases with and without rods installed in the flow separator. Note that the centreline velocity U_c tended to slightly increase with streamwise position for both cases due to flow acceleration caused by boundary layer growth. The addition of the rods in the shear generator had the undesirable effect of decreasing the mean shear of the flow. This can be attributed to the momentum loss by the rods,

	LDV						PIV
	Without rods			With rods			Without rods
x_1 (m)	0.57	1.86	3.21	0.57	1.86	3.21	2.58
$d\overline{U_1}/dx_2$ (s^{-1})	0.431	0.444	0.469	0.421	0.421	0.417	0.53
U_c (m/s)	0.161	0.163	0.165	0.164	0.165	0.167	0.18
τ	1.5	5.1	9.1	1.5	4.7	8.0	7.6

Table 5.1: The flow parameters measured using LDV and PIV.

which is higher at higher velocities [21]. The difference in the velocity gradient also affected the dimensionless development time τ. Because of the decreased shear rate and the decreased range of τ associated with the rods, no rods were used in further experiments.

Time-averaged measurements of the flow using PIV, different from the PIV measurements presented in Section 5.4, were performed at a downstream position with $x_1 = 2.58$ m. PIV measurements of the mean velocity and mean shear, also displayed in Table 5.1, were higher than the LDV values by about 10% and 15% respectively. The time-averaged measurements using the PIV were performed before the additional nylon line was fastened on the shear generator, which could account for at least part of this discrepancy. In any case, considering the higher uncertainty of the PIV measurements, and that only 100 samples were used for time-averaging compared to more than 1000 for the LDV, only LDV results will be used as time averages.

5.1.2 Turbulent stresses

The turbulent stresses and the turbulent shear stress correlation coefficient were calculated from both the LDV and the PIV measurements. The vertical profiles of the parameters have been plotted in Figure 5.2. Values are relatively uniform near the centre and lower half of the tunnel, but decrease drastically at the top of the tunnel. This was also found by Kislich-Lemyre [23] and Menu [28] and is attributed to the drop in mean shear near the free surface. To avoid this complication, all subsequent results were taken in the central and lower sections of the tunnel. The PIV recorded slightly lower streamwise fluctuations, and a slightly higher magnitude of the shear stress correlation coefficient.

In conformity with previous USF results, the streamwise normal stress was found

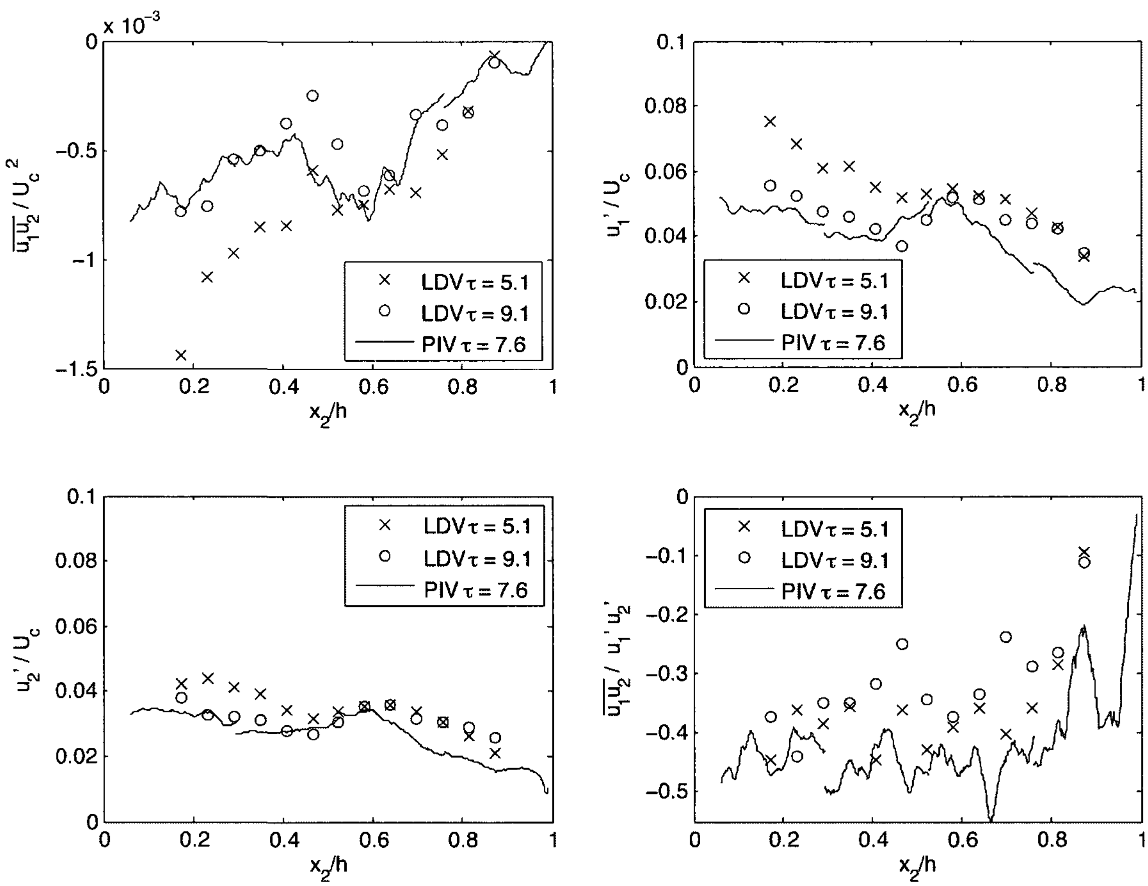

Figure 5.2: Vertical profiles of the normalised velocity component standard deviations and the shear stress correlation coefficient.

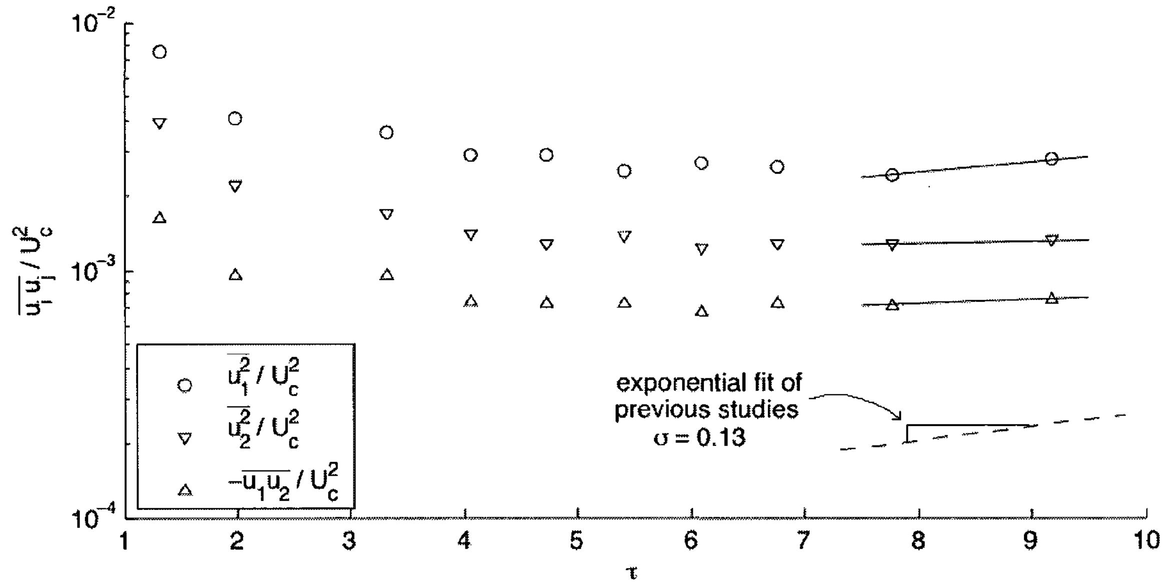

Figure 5.3: Downstream development of the normalised velocity component standard deviations at $x_2/h = 0.634$.

to be larger than the transverse normal stress. Also, the shear stress correlation coefficient was typically about 0.4 and at times approached 0.45, which is close to previous results. The ratio of $\overline{u_1^2}/\overline{u_2^2}$ was approximately 2.0, which is slightly smaller than the value of 2.5 found in previous studies [44].

The downstream development of the turbulence, measured with the LDV along a streamwise line in the tunnel at $x_2/h = 0.634$ and $x_3 = 0$, is presented in Figures 5.3 and 5.4. All stresses decayed from initially high values and reached minima at about $\tau = 5$, beyond which they increased at a mild rate. Kislich-Lemyre [23] found that all the normalised velocity component standard deviations exponentially grew beyond $\tau = 5$ at a similar rate to that of the turbulent kinetic energy according to

$$\frac{\overline{u_iu_j}}{U_c^2} = k_o \times e^{\sigma\tau}, \tag{5.1}$$

where k_o was a variable reference value, and σ was found to be approximately 0.13. For the streamwise data at $x_2/h = 0.634$, σ is calculated to be 0.10 for $\overline{u_1^2}/U_c^2$, 0.02 for $\overline{u_2^2}/U_c^2$, and 0.04 for $\overline{u_1u_2}/U_c^2$. When interpreting these results, one must take into consideration that they are extremely sensitive to experimental scatter, which was appreciable in these measurements. Estimating the mean growth of these values

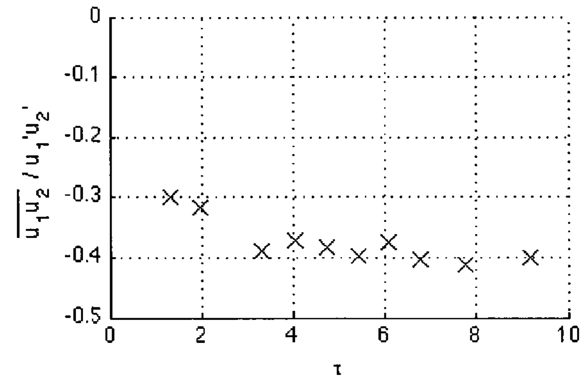

Figure 5.4: Downstream development of the shear stress correlation coefficient at $x_2/h = 0.634$.

from the data presented in Figure 5.2 at $\tau = 5.1$ and 9.1, the mean growth rate at $x_2/h = 0.23$ was about $\sigma = 0.14$, and about $\sigma = 0.08$ at $x_2/h = 0.52$. Though the growth rates at $x_2/h = 0.634$ are relatively low, the mean growth rate averaged over the entire depth of the flow is comparable to previous studies.

5.1.3 Length scales

The LDV data have sufficient temporal resolution for calculating the turbulent integral time scale. Taylor's frozen flow approximation was used to convert the temporal fluctuations of the measured local velocity to spatial fluctuations in the streamwise direction. The streamwise integral length scale was measured by integrating the autocorrelation function of the velocity signal as

$$L_{11,1} \approx U_1 \cdot \int_0^\infty \frac{\overline{u_1(t)u_1(t+\mathrm{d}t)}}{\overline{u_1^2(t)}} \mathrm{d}t. \tag{5.2}$$

The integral length scale was measured first at a downstream position of about $x_1 = 2$ m ($\tau = 5.6$), at $x_2/h = 0.65$ and $x_3 = 0$. This record consisted of 514,105 samples and was obtained using 'coincident burst' mode, which records all passing particles. The mean time separation between passing particles was 2 ms and the maximum observed time separation was 30 ms. Because the particles had random arrival times, the data were resampled at a fixed time interval of 5 ms using a sample/hold method [42] before the autocorrelation calculation was performed.

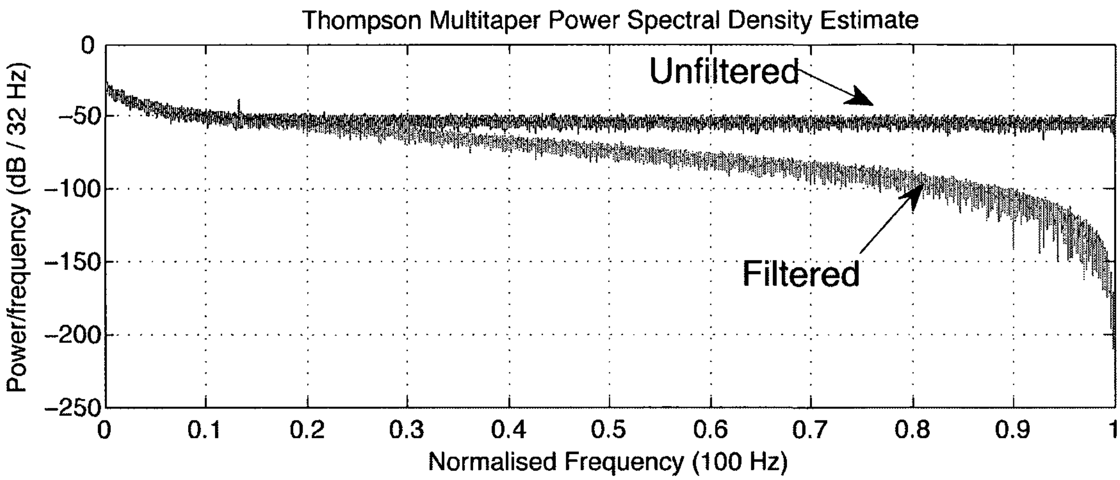

Figure 5.5: Comparison of the spectra of the unfiltered and filtered velocity fluctuation signals, used in the calculation of the integral length scale.

It was found that the LDV measurement using 'burst' mode contained some noise. In order to reduce the effect of the noise, a second-order low-pass Butterworth filter was applied to the resampled data before calculating the autocorrelation. A cut-off frequency of 20 Hz (0.2 times the Nyquist frequency) was chosen, corresponding to a time period of 50 ms. The spectra before and after filtering are displayed in Figure 5.5. The filter only removed high frequency noise and preserved the low-frequency fluctuations, which are associated with the dominant coherent structures, as shown in Figure 5.6.

The signal was then partitioned into consecutive records 24 s long, and the autocorrelation coefficient was calculated for each record. The results were then ensemble averaged before being integrated. The ensemble-averaged autocorrelation coefficient is presented in Figure 5.7. The integral length scale was estimated by integrating this coefficient until it first crossed zero. The resulting value was $L_{11,1} = 28$ mm.

The precision uncertainty of this measurement was estimated by comparing it to the result of the same calculations applied to a second long data record of 263,387 samples. Furthermore, the effect of the choice of parameters was explored by varying the cut-off frequency of the filter and the window size of the autocorrelation. Besides the unfiltered case, filters with two cut-off frequencies, equal to 0.5 and 0.2 times the sampling frequency, were used. Two window sizes were tested: 16 s, which is 100

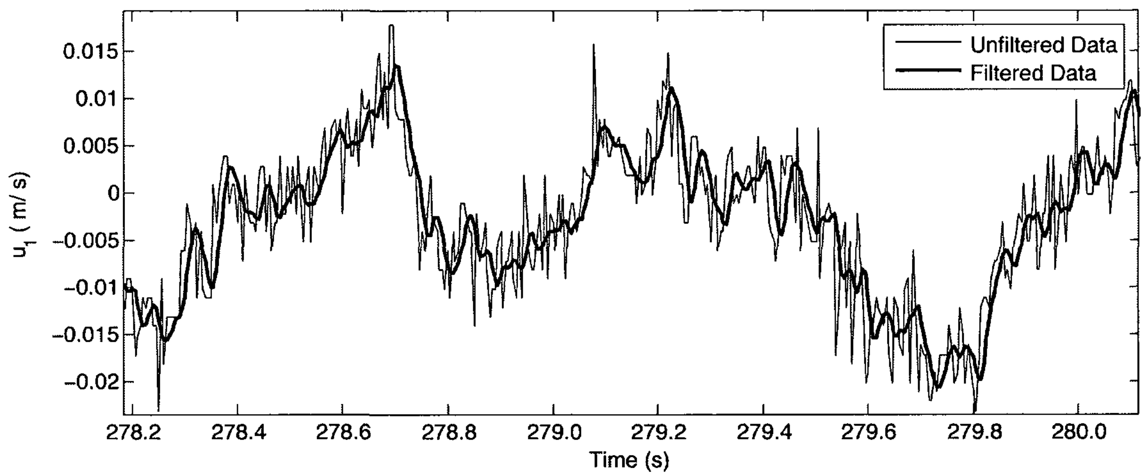

Figure 5.6: A portion of the velocity fluctuation signal used in the calculation of the integral length scale, comparing the unfiltered and filtered signals.

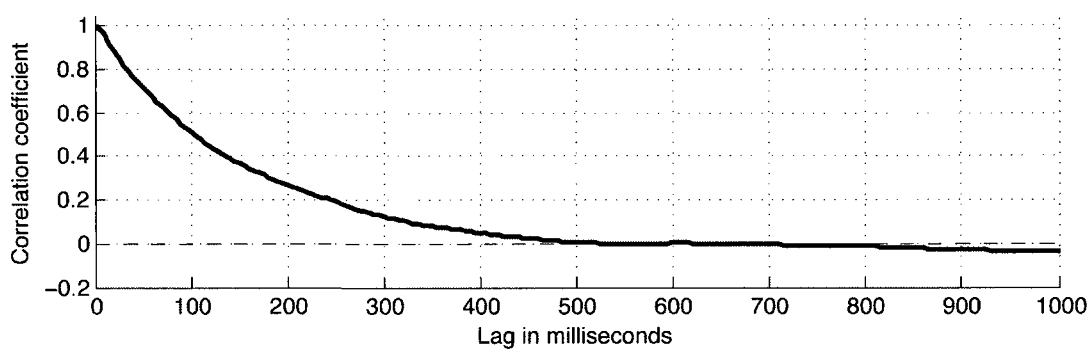

Figure 5.7: The autocorrelation coefficient of the streamwise velocity fluctuations at $x_1 = 2$ m ($\tau = 5.6$), $x_2/h = 0.65$, and $x_3 = 0$.

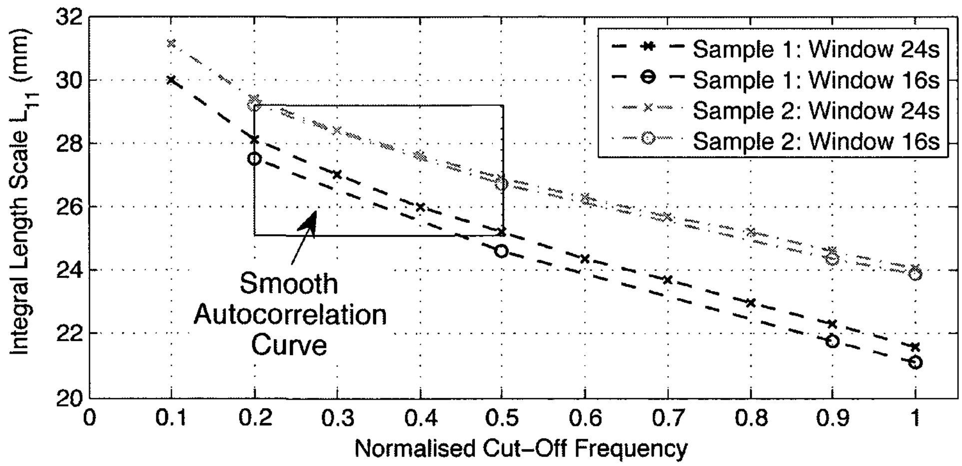

Figure 5.8: Results from two separate measurements of integral length scales, illustrating the effect of the cut-off frequency of the filter and the window size of the autocorrelation.

times the time scale, and 24 s. A scatter plot of these results is presented in Figure 5.8. The calculated length scales ranged between 21 mm and 31 mm, illustrating the uncertainty of the length scale measurement. Only considering the results using 20% or 50% filters, which properly reduced the effect of the noise and resulted in smooth autocorrelations, the true length scale was found to be $L_{11,1} = 27 \pm 2$ mm.

Using a similar method for the u_2 signal, the transverse length scale was calculated as $L_{22,1} = 12 \pm 3$ mm.

Velocity measurements at ten downstream positions were used to estimate the streamwise evolution of the integral length scale. These were the same measurements that were used to calculate the streamwise evolutions of the turbulent stresses presented in Figure 5.3. These measurements typically only consisted of about 2000 to 3000 samples, recorded using 'coincident dead-time' mode. The data rate had a mean period of about 40 ms. These records did not exhibit the same noise as the previous data set, which was presumably caused by using the LDV in 'burst' mode or because of the lower sampling rate. Using a resampling rate of 5 ms and a window size of 24 s, the length scales at each position were calculated using the same method as previously, with the exception that no noise filter was applied. The length scale evolution is presented in Figure 5.9.

The precision uncertainty of these results is larger than that of the result of the

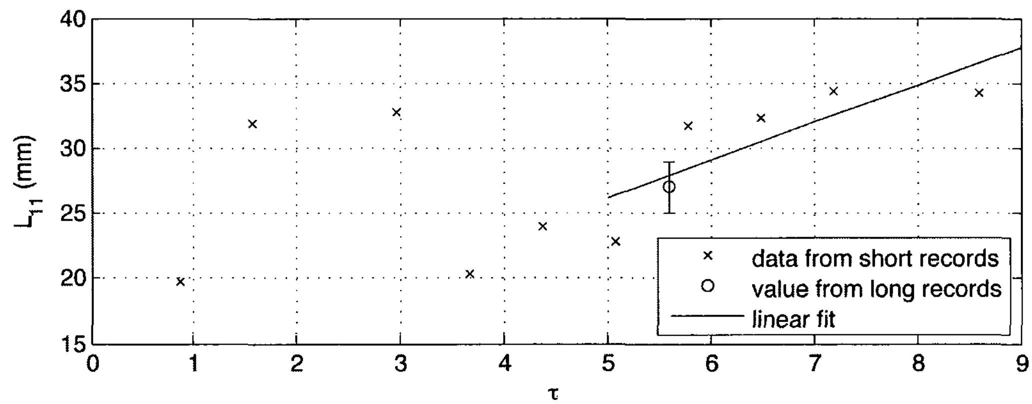

Figure 5.9: Calculated development of the integral length scale $L_{11,1}$ at $x_2/h = 0.634$.

previous record, as reflected in the data scatter. The especially large scatter at $\tau < 4$ may be further attributed to the undeveloped state of the flow near the beginning of the test section. Furthermore, the bias uncertainty of the results was affected by the choice of calculation parameters. Increasing the resampling frequency from 5 ms to 20 ms increased the values of the length scale by 0.5 mm. A reduction of the length of the partitioned records from 24 s to 16 s caused a reduction in the length scale of about 2-3 mm. The application of a low-pass filter increased the length scale by about 1 mm.

A trend line was fit to the data in the range of $5 < \tau < 9$. The evolution of the integral lengthscale described by this trend line can be represented as

$$\frac{L - L_o}{L_o} = a\ \tau, \tag{5.3}$$

where L_o is the value of the integral lengthscale extrapolated to $\tau = 0$. In the present study, these values are found to be $L_o = 12$ mm and $a = 0.24$. Tavoularis and Corrsin [45] also found the integral length scale to grow linearly with downstream position. Tavoularis and Karnik [46] fit a power law to their results and estimated the exponent in the range of 0.8 to 1.0. This exponent indicated a trend that was almost linear.

5.1.4 Turbulent kinetic energy estimates

In this study only two of the three normal stresses were measured. The turbulent kinetic energy was estimated by assuming that the anisotropy coefficients in the present flow were comparable to those in previous studies, which were summarised previously in Equation 2.17. Thus the turbulent kinetic energy was estimated as

$$k = \frac{1}{2}\left(\overline{u_1^2} + \overline{u_2^2} + \overline{u_3^2}\right), \tag{5.4}$$

where the value of $\overline{u_3^2}$ was estimated from the anisotropy coefficients and the measured $\overline{u_1^2}$ as

$$\overline{u_3^2} = \left(\frac{1/3 + m_{33}}{1/3 + m_{11}}\right)\overline{u_1^2} = \left(\frac{1/3 - 0.04}{1/3 + 0.17}\right)\overline{u_1^2} = 0.583\ \overline{u_1^2}. \tag{5.5}$$

This estimate was calculated at ten downstream positions using the same LDV measurements that were used to calculate the streamwise evolutions of the turbulent stresses and of the integral length scale.

The local rate of change of turbulent kinetic energy with streamwise position was estimated from the local slope of the kinetic energy using a central difference discretisation scheme, except at either end of the data where a one-sided first-order discretisation scheme was used. This spatial derivative was then translated to a temporal derivative by multiplying by the mean streamwise velocity of the flow as

$$\frac{dk}{dt} = \overline{U_1}\frac{dk}{dx_1} \tag{5.6}$$

The rate of production of turbulent kinetic energy was calculated as

$$Pr = -\overline{u_1 u_2}\frac{d\overline{U_1}}{dx_2}. \tag{5.7}$$

The average rate of turbulent kinetic energy dissipation ϵ was estimated from the balance of the rate of change of turbulent kinetic energy and the production as

$$\epsilon = Pr - \frac{dk}{dt}, \tag{5.8}$$

based on values of dk/dt and Pr which were initially smoothed using fifth-order and second-order polynomials, respectively, fit to the data at $\tau > 1.5$.

The downstream developments of these properties are plotted in Figure 5.10. As illustrated, the kinetic energy only began to grow near the end of the measurement range. The rate of change of the kinetic energy was positive at $\tau \gtrsim 6$. The balance between the production and dissipation also reflects this result, as the production

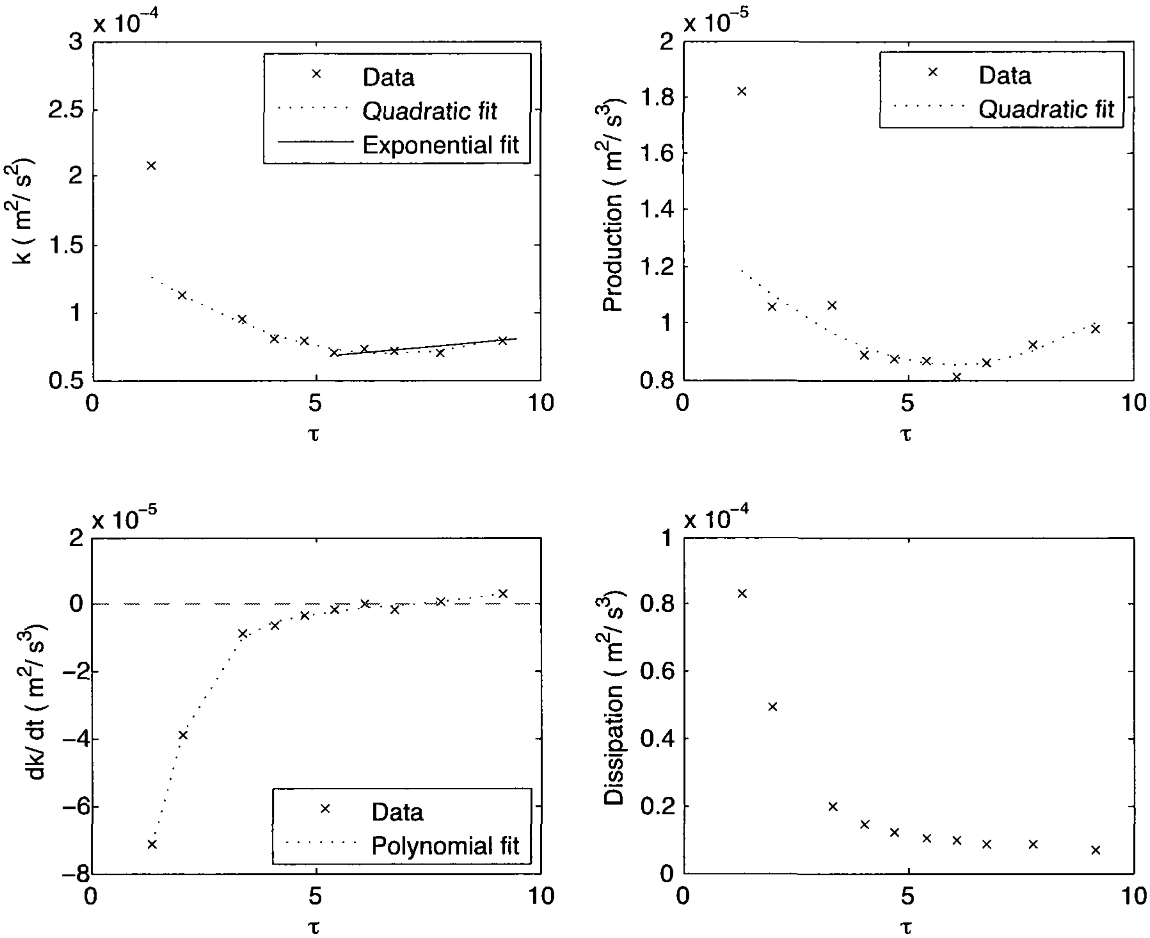

Figure 5.10: The downstream developments of the kinetic energy, the rate of change of kinetic energy, the production, and the dissipation at $x_2/h = 0.634$, $x_3 = 0$.

began to grow at $\tau \approx 6$, while the dissipation still decreased. An exponential fit to the kinetic energy measurements in the range $\tau > 4$ yields the relation

$$k = k_o \, e^{\sigma \tau}, \tag{5.9}$$

where $k_o = (5.5 \times 10^{-5} \ \mathrm{m^2/s^2})$ and $\sigma = 0.04$. This value of σ is rather low, though, as discussed previously, the turbulent kinetic energy averaged over a larger range of x_2 positions would have a greater mean growth rate.

Besides direct measurements, the turbulent length scales were estimated using empirical relations. The integral length scale L_{11}, Taylor microscale λ, and Kolmogorov microscale η were estimated as

$$L_{11} = \frac{0.24 \cdot (2k)^{3/2}}{\epsilon}, \tag{5.10}$$

$$\lambda_{11} = \sqrt{\frac{12 \cdot \nu \cdot (2k)}{\epsilon}}, \tag{5.11}$$

$$\eta = \left(\frac{\nu^3}{\epsilon}\right)^{\frac{1}{4}}, \tag{5.12}$$

where the values of k were obtained from a second-order polynomial fitted to the data at $\tau > 1.5$ [23] [44]. The streamwise developments of these properties are plotted in Figure 5.11. As expected, the length scales are ordered as $L_{11} > \lambda_{11} > \eta$. The estimated integral length scale L_{11} significantly differs from the same value calculated using the autocorrelation. Though the values are comparable at small τ, the estimated length scale grows at more than twice the rate of the measured length scale, reaching a value of 50 mm at the end of the test section. Similarly, the Taylor microscale is shown to double in magnitude over the length of the test section, however, it tended to level off after $\tau = 6$, agreeing with observations by Tavoularis and Corrsin [45] and Tavoularis and Karnik [46] that λ changes little in the fully-developed USF.

The turbulent Reynolds numbers were calculated as

$$Re_L = \frac{u_1' \cdot L_{11}}{\nu}, \tag{5.13}$$

$$Re_\lambda = \frac{u_1' \cdot \lambda_{11}}{\nu}. \tag{5.14}$$

The values of these Reynolds numbers at a range of downstream positions are plotted in Figure 5.12. These values were fairly steady in the range $3 < \tau < 8$, with values of $Re_L = 290$ and $Re_\lambda = 90$.

For convenience, the results at a downstream distance of $\tau = 5.6$ are summarised in Table 5.2, with precision uncertainties estimated from their scatter in the range $\tau > 6$. These results are comparable to the previous measurements taken in this water tunnel by Kislich-Lemyre [23] and Menu [28].

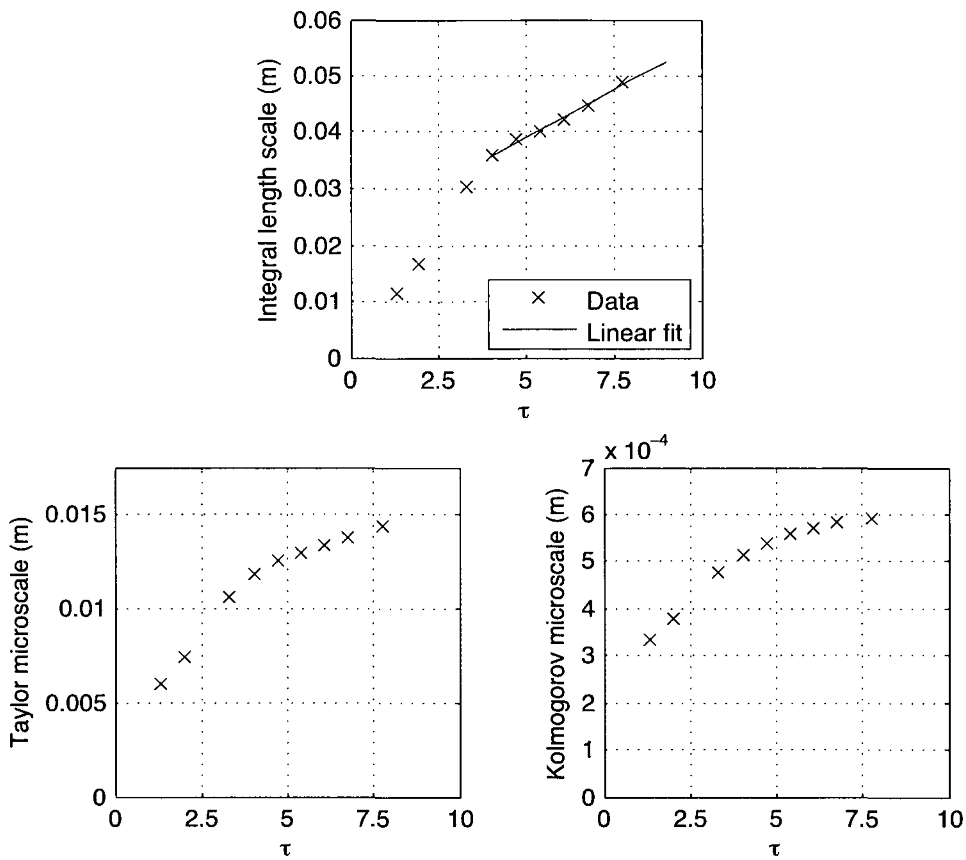

Figure 5.11: The downstream developments of the estimated length scales at $x_2/h = 0.634$, $x_3 = 0$.

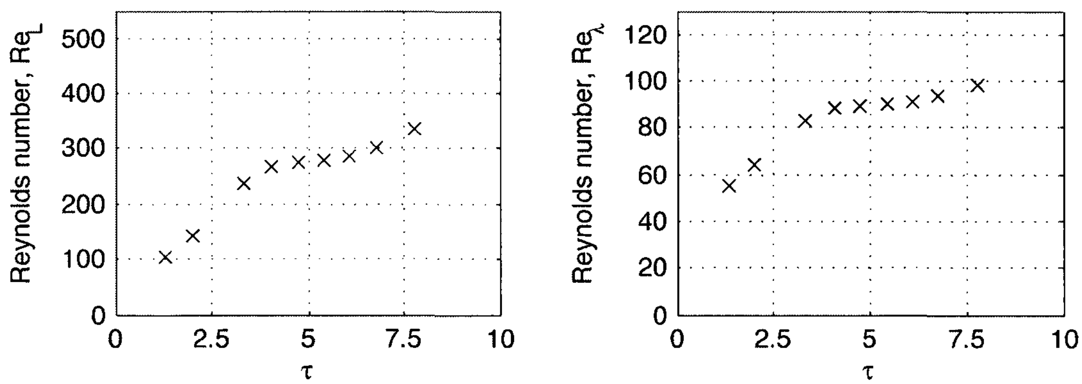

Figure 5.12: The downstream developments of the turbulent Reynolds numbers at $x_2/h = 0.634$, $x_3 = 0$.

Averaged Flow Property	Symbol	Value and Range
Turbulent kinetic energy	k	$(8 \pm 1) \times 10^{-5}$ ($\mathrm{m^2/s^2}$)
Rate of change of turbulent kinetic energy	dk/dt	$(1 \pm 2) \times 10^{-6}$ ($\mathrm{m^2/s^3}$)
Rate of production	Pr	$(9 \pm 1) \times 10^{-6}$ ($\mathrm{m^2/s^3}$)
Rate of dissipation	ϵ	$(8 \pm 3) \times 10^{-6}$ ($\mathrm{m^2/s^3}$)
Calculated value of integral length scale	$L_{11,1}$	0.027 ± 0.002 (m)
	$L_{22,1}$	0.013 ± 0.003 (m)
Empirical estimate of integral length scale	$L_{11,1}$	0.05 ± 0.02 (m)
Empirical estimate of Taylor microscale	$\lambda_{11,1}$	0.014 ± 0.003 (m)
Kolmogorov length scale	η	$(5.9 \pm 0.4) \times 10^{-4}$ (m)
Turbulent Reynolds numbers	Re_L	300 ± 50
	Re_λ	90 ± 10
Shear-rate parameter	S^*	11 ± 6

Table 5.2: Average flow properties in the core region of the USF near $x_1 = 2.0$ m ($\tau = 5.6$).

5.2 Scanning dye visualisation

Dye patterns in the flow were scanned in order to provide insight into the 3D appearance of the vortical structures. Mounted on the scanning cart system, the planar laser sheet scanned the length of the test section in about 1 s, during which time flow changes were deemed to be negligible. The dye pattern was only visible in the plane of the laser sheet and a high speed camera recorded the planar fluorescent dye patterns during the entire scan. The video was afterwards trimmed to remove images taken during the acceleration and braking stages of the scan, which limited the video length to about 0.4 s or about 200 frames in the centre of the test section.

During the scan, the camera recorded the entire part of the flow that was marked by dye, which occupied a cross-sectional area of approximately 250 mm by 250 mm. The edges of the laser sheet were visible on either side of the image and the image of the ruler was recorded in the upper left corner. During post-processing, the image was reflected to facilitate reading of the ruler. The exposure and gamma correction were also adjusted to boost brightness and contrast. A sample image is provided in Figure 5.13. The graininess of the image was due to the limited intensity of the laser light.

5.2.1 Measurements of the cart position and speed

The position of the cart was measured using the image of a ruler. For each data set, the position of one of every 50 frames was visually read off the ruler and recorded. The positions of the other frames were then found by interpolation using a cubic curve fitted to positions of the frames that were known. The uncertainty of this method is estimated to be less than 1% in the middle of the scan, as indicated by the residuals of the curve fit. The uncertainty increased near the beginning of the scan because of the jerks of the gate latch release mechanism and near the end because of the effects of the brake.

The position and velocity variations of a typical scan using a weight with the mass of 9.5 kg are plotted in Figure 5.14. As illustrated, the cart continuously accelerated, reaching a speed of 1 m/s after about 0.55 s. For comparison, the centreline velocity of the flow was about 0.16 m/s, travelling in the opposite direction to that of the

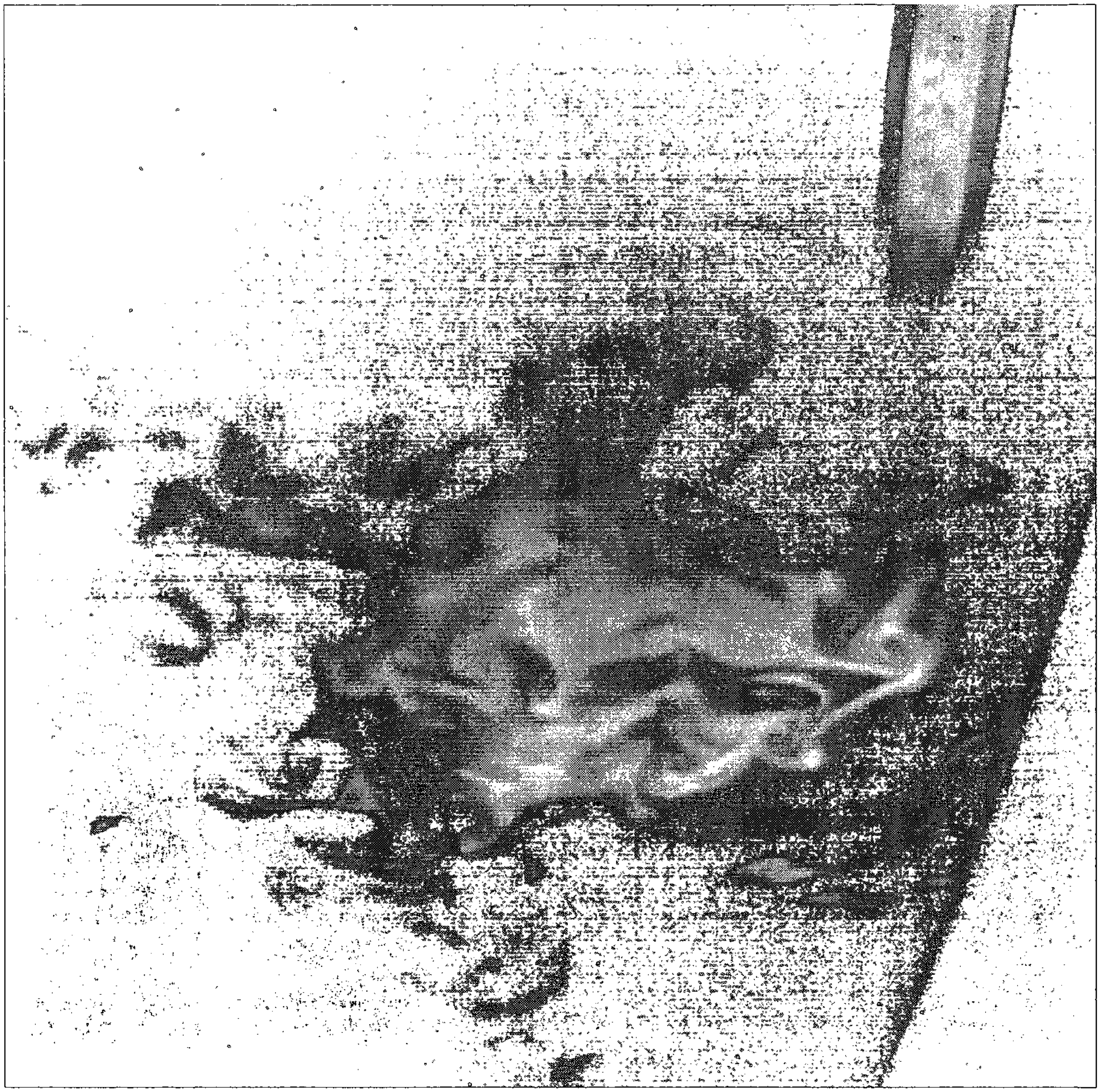

Figure 5.13: Sample image taken mid-scan of the dye pattern formed in USF.

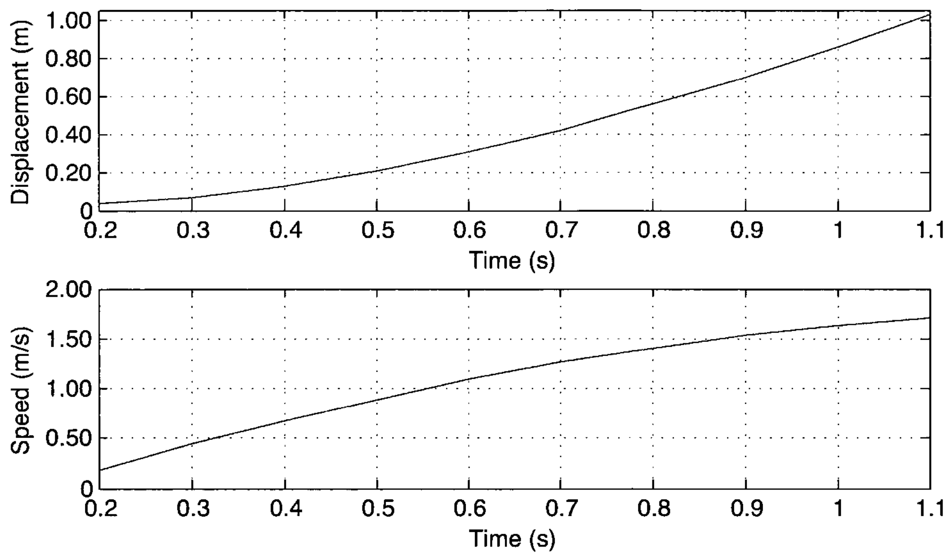

Figure 5.14: Cart displacement and speed measurements of a typical scan set in motion by a 9.5 kg mass. The flow speed was $U_c = 0.16$ m/s, travelling in the opposite direction to that of the cart.

cart. After just over 1 s of travel, the brake was engaged and the cart was quickly brought to a stop.

All analysis used the part of the video from 0.7 to 1.1 s, during which the speed was highest.

5.2.2 Identification of structures

Several recurrent dye patterns were observed in these video images. Because the scan captured instantaneous dye patterns, the motion of such patterns cannot be observed to infer the vortex positions. Vortices were identified by locating dye patterns that had circular or spiral outlines. These were common throughout the flow but were most easily distinguished near the edges of the dye cloud and near the bottom of the image where the laser light was most intense. Several vortex patterns can be observed in the sample image of Figure 5.13, including that of one of the examples discussed in the following.

Vortices were observed to interact with each other and to travel in groups. Pairs were very common and were distinguished by bridges of dye connecting the two vortices, or by dye streaks between the two vortices. Such patterns were typically mushroom-shaped. Observations of these mushroom-shaped dye patterns indicate that the separation distance between the vortices was in the range from 20 to 50 mm. Most dye patterns could only be tracked for a maximum of 20 frames after which they faded or became mixed with other patterns.

A close look at an inverted mushroom-shaped vortex pair is presented in the frame sequence of Figures 5.15 to 5.16. In this case, the vortex pair was tracked for about 25 frames, which corresponds to a streamwise length of 60 mm, or an actual length of 66 mm, when applying the 10% correction for the displacement of the flow during the scan. Dye was drawn between the two vortices just after they became visible. The two vortices moved together away from the dense cloud of dye and were visible because of the dye that was entrained in them. The two vortices began to grow further apart and eventually the bridge of dye between them was broken. After this point, the dye entrained in each separate vortex was visible for a short time before it disappeared. It is inferred that the vortices were counter-rotating, such that a downwards velocity was induced in the space between them. This inverted mushroom-shaped pattern was not a rare specimen as most of the vortex pairs observed tended to face downwards. This may be because the best dye contrast was found at the bottom of the image where the laser intensity is strongest, favouring the downwards-facing vortices which entrained dye out of the dense cloud of dye into the more clear region at the bottom of the image.

A 3D reconstruction of the vortex pair corresponding to this frame sequence is presented in Figure 5.17. This vortex pair was only about 66 mm in length, however, this measurement of the length of the structure is expected to be shorter than its true length due to the difficulty in tracking the structures in the dye images. The two counter-rotating vortices were separated by a distance of about 50 mm. The vortices were both inclined upwards by about 35° with respect to the x_1-direction in the $x_1 - x_2$ plane, and sideways by about 25° with respect to the x_1-direction in the $x_1 - x_3$ plane; this corresponds to an inclination of 56° with respect to the x_3-direction in the $x_2 - x_3$ plane.

The two counter-rotating vortices were interpreted as the legs of a hairpin structure, similar to those observed in the turbulent boundary layer. The shapes and

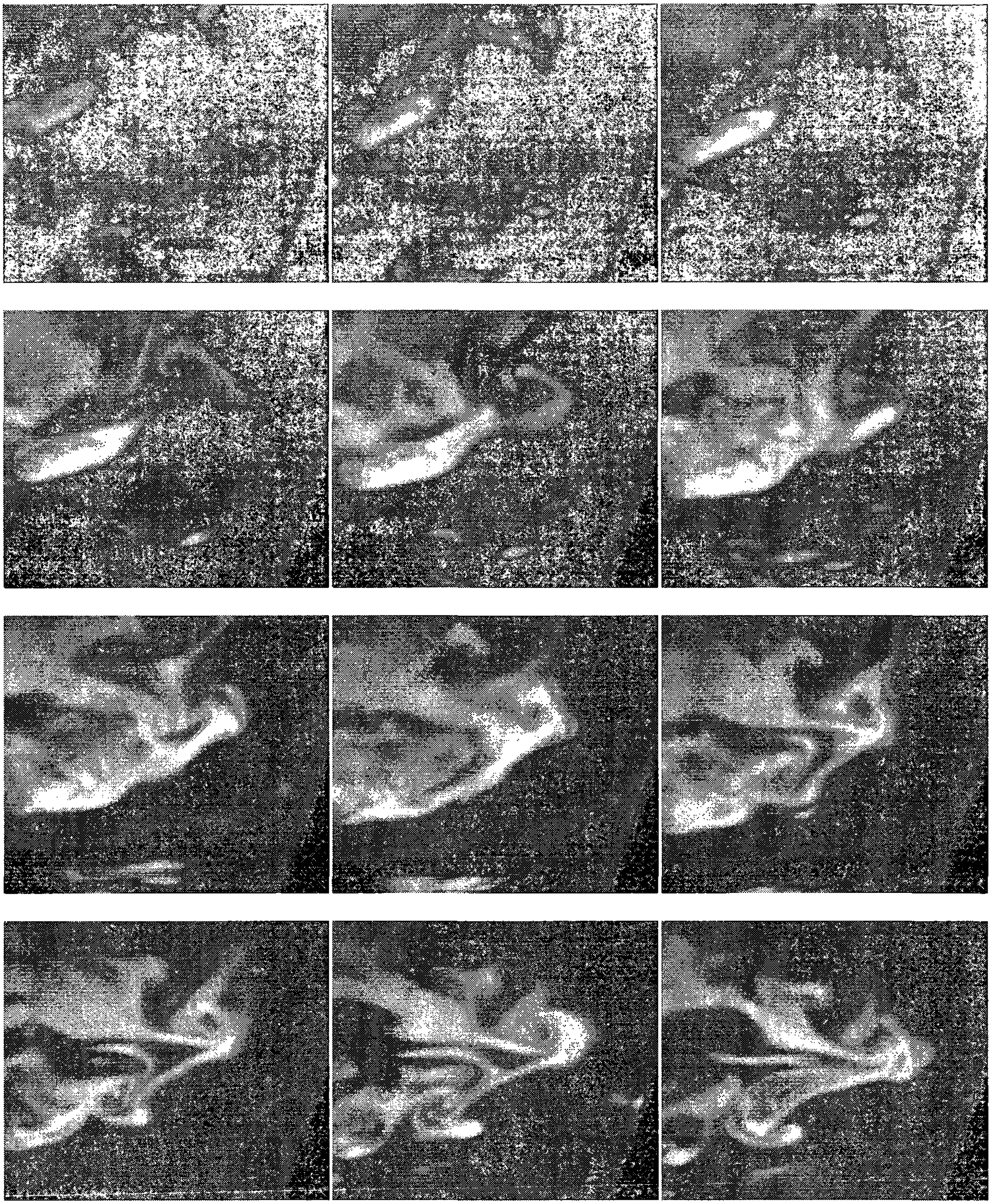

Figure 5.15: Frame sequence 1/2 of a scan through an inverted mushroom-shaped vortex pair.

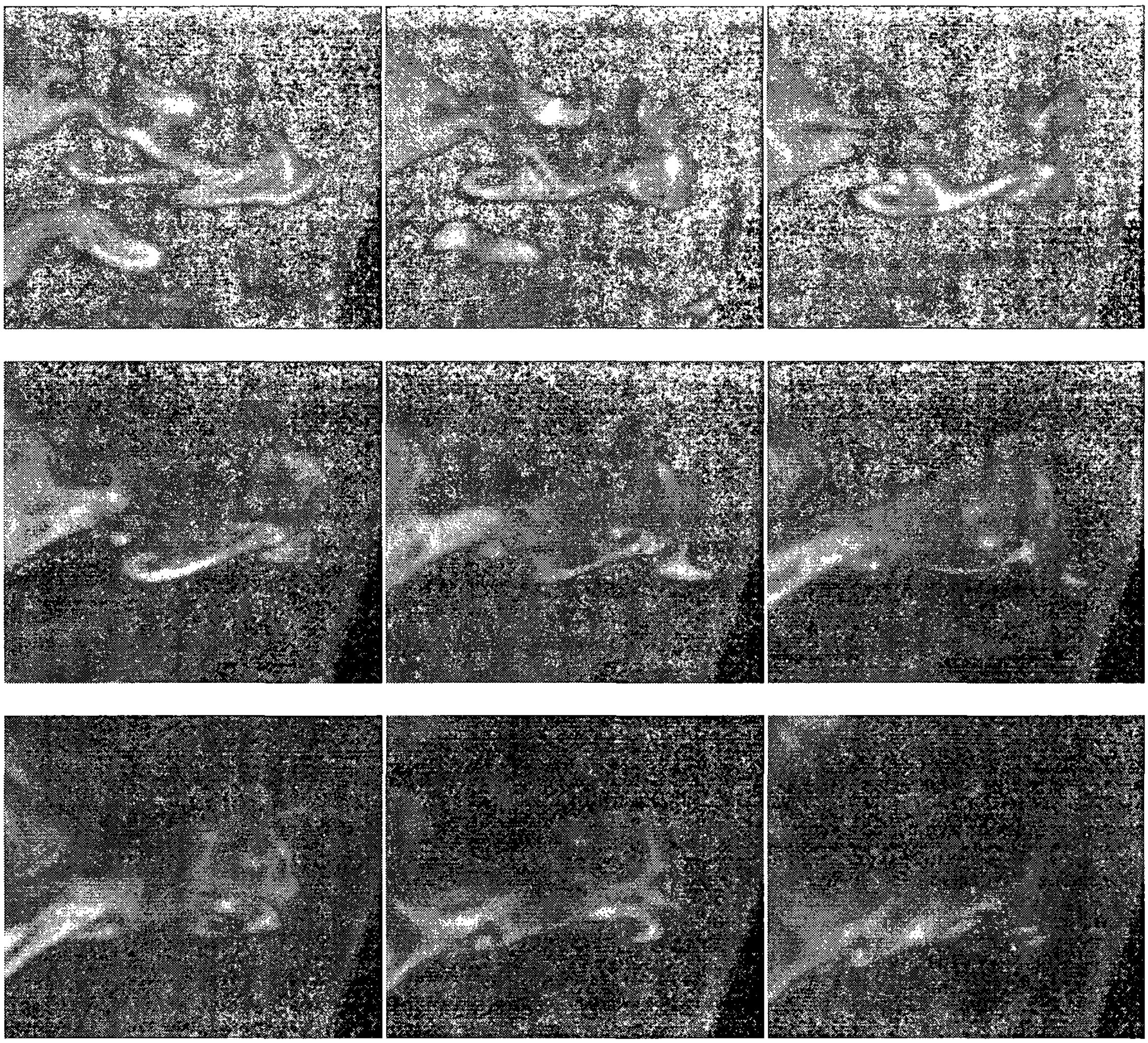

Figure 5.16: Frame sequence 2/2 of a scan through an inverted mushroom-shaped vortex pair. The cropped frame is 11 cm tall and frames are separated by 2/500 s, starting from downstream moving upstream.

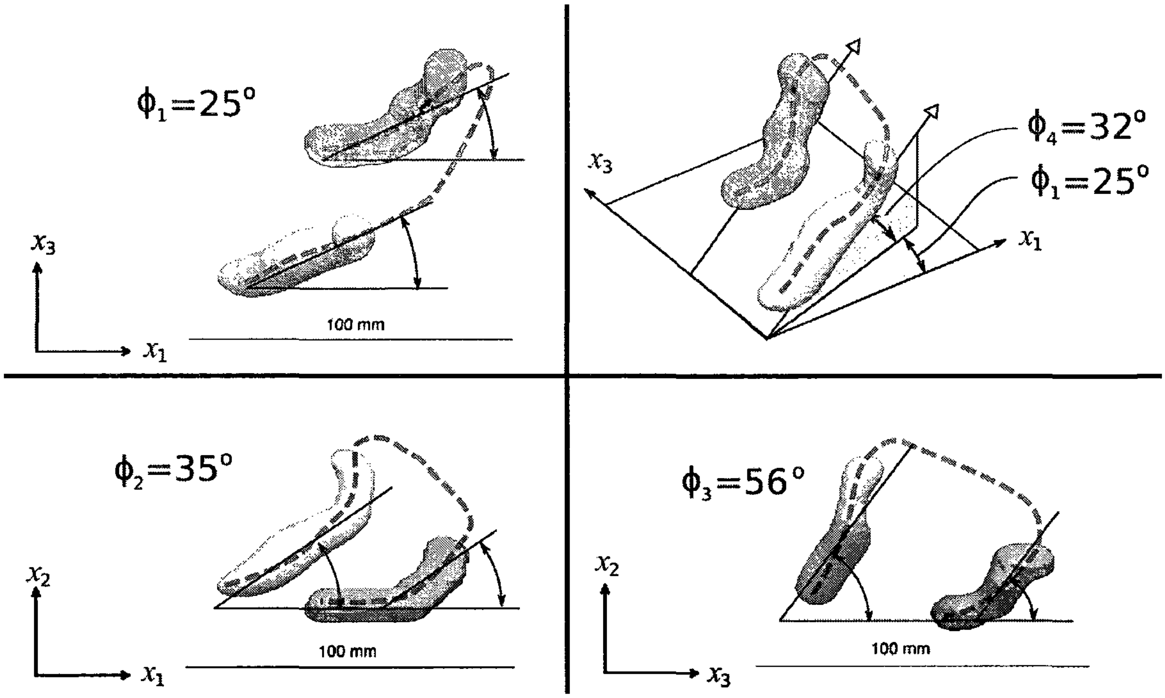

Figure 5.17: A 3D reconstruction of the scanned inverted vortex pair from Figures 5.15 - 5.16. This pair is counter-rotating such as to induce a downwards flow between themselves. A dashed line indicates the likely 3D hairpin structure.

orientations of the dye patterns were comparable in both flows, except for the direction of rotation, which in this example was opposite to that of the hairpin structures of the turbulent boundary layer. Though the head of the hairpin vortex was difficult to discern from the dye pattern, it was expected to be located ahead of the trailing legs like those structures of the turbulent boundary layer. A sketch of the likely configuration of the hairpin is superimposed on the results presented in Figure 5.17. In the smoke visualisations of Head and Bandyopadhyay [16], the heads of hairpins were only clearly distinguished using a laser sheet inclined at $-45°$, in which the dye patterns formed loops. Their images using a laser sheet inclined at $+45°$, such as in the current study, revealed upright mushroom-shaped dye patterns, similar to those observed currently.

An example of an upright vortex pair was tracked in the frame sequence shown in Figures 5.18 to 5.19. This specimen was located near the top left edge of the image where the dye pattern had less contrast from the background than in the previous example. The vortex pair was distinguished by the elongated T-shaped dye pattern, whose arms curl around the two vortices midway through the frame sequence. The dye forming the stem of the 'T' was entrained between the two vortices in an upwards burst, clearly identifying the direction of rotation of the two vortices. As the frame sequence progresses, the T-shaped pattern shrank becoming two spots marking the positions of the two vortices. Evidence of the left vortex then disappeared as it probably moved outside of the light sheet or the region marked by the dye. The dye pattern of the right vortex melded with another coincident dye streak, which appeared to be a sideways bursting mushroom pair; however, the dye pattern was too unclear to lead to firm conclusions. A 3D reconstruction of the two vortices that fit this dye pattern is presented in Figure 5.20. Just as the example of the inverted vortex pair, this pair was inclined at about 35°, however the head of the structure was inclined at a steeper angle of about 70°. This pair was tracked for only 80 mm of downstream distance, corresponding to a length of about 88 mm, and the vortices were separated by about 40 mm.

Both of these examples of vortex pairs had sizes that were relatively long compared to the average. Smaller vortices were more common but more difficult to pair to another vortex with confidence as they could not be tracked for many frames.

5.2.3 Summary of observations

The main flow feature of interest identifiable from the high speed video was the mushroom-shaped vortex pair. These were fairly numerous and had widths in the range from 20 to 50 mm. Structures were often observed bursting downwards from the dye cloud. The dye structures could typically only be tracked for up to 20 frames of the video, corresponding to a time step of only 1/25 s and a streamwise length of about 70 mm. This length was probably limited by dye visibility rather than the true length of the vortices. Furthermore, all the flow structures tended to move downwards in the inclined frame of reference of the video images. In most cases the flow structures were inclined upwards by about 45° with respect to the x_1-direction in the $x_1 - x_2$ plane, although instances with inclinations in the range of 30° to 70° were observed.

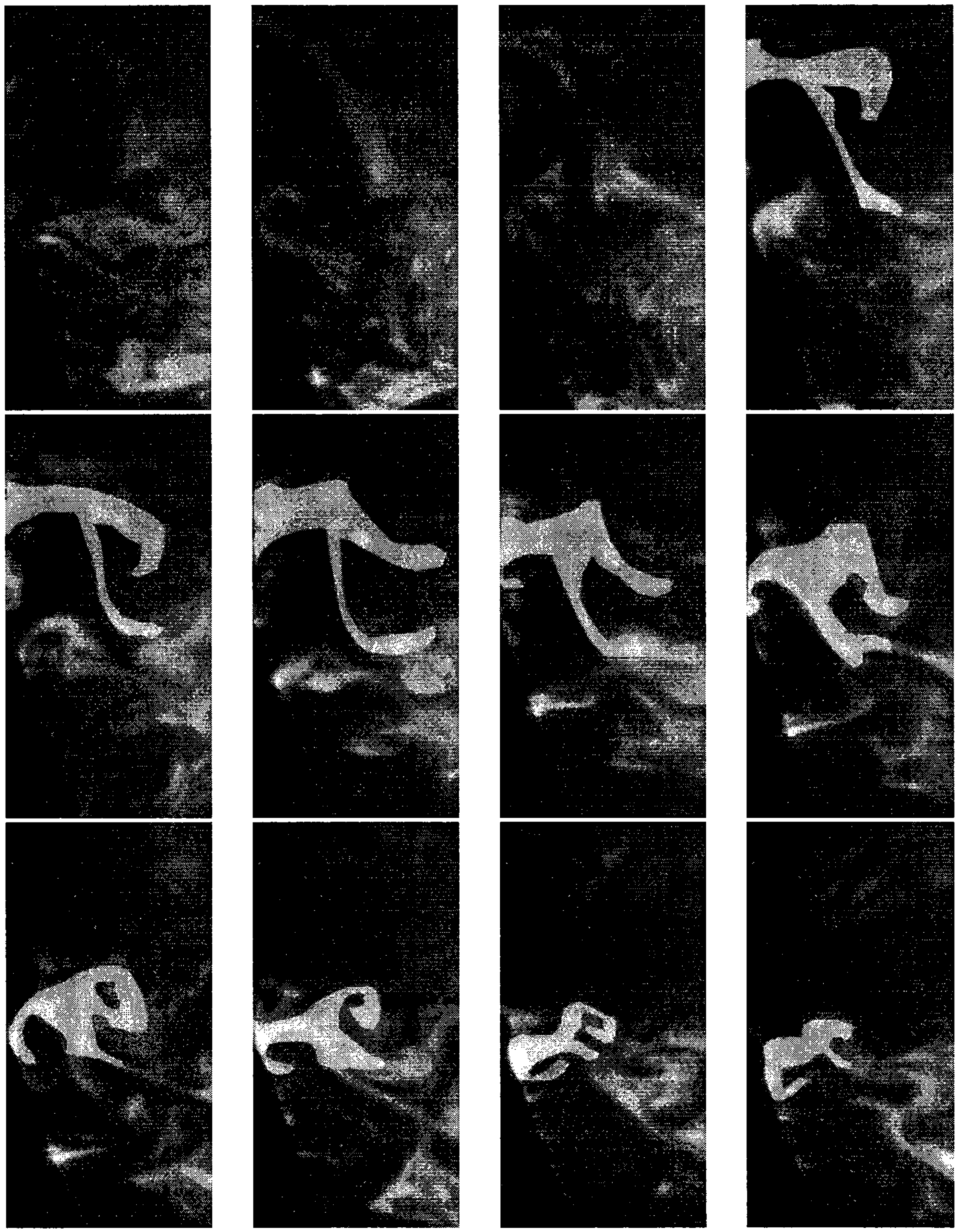

Figure 5.18: Frame sequence 1/2 of a scan through an upright vortex pair.

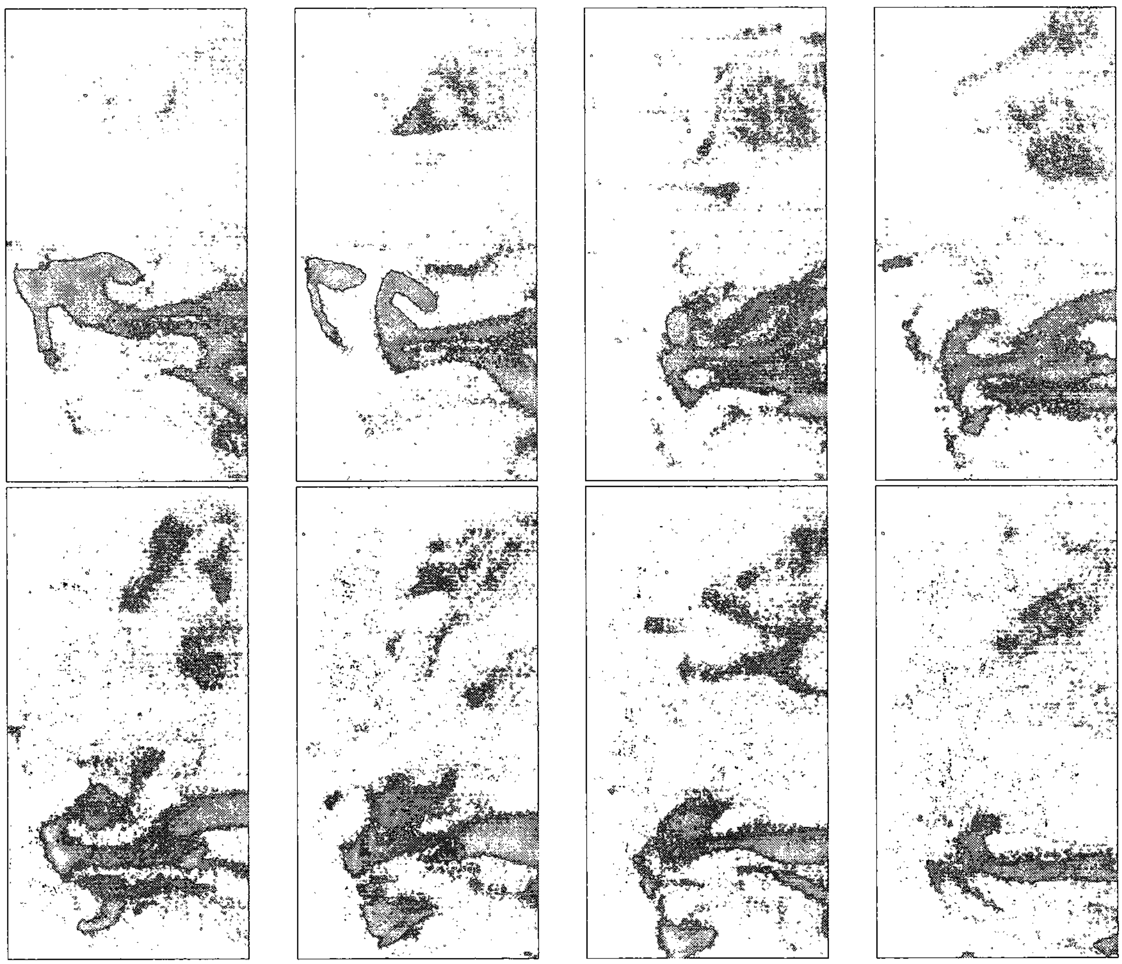

Figure 5.19: Frame sequence 2/2 of a scan through an upright vortex pair, characterised by the T-shape dye pattern. Because of the poor contrast in this area of recording, the flow feature of interest has been highlighted in the key frames. The cropped frame is 15 cm x 8 cm and frames are separated by 2/500 s, starting from downstream moving upstream.

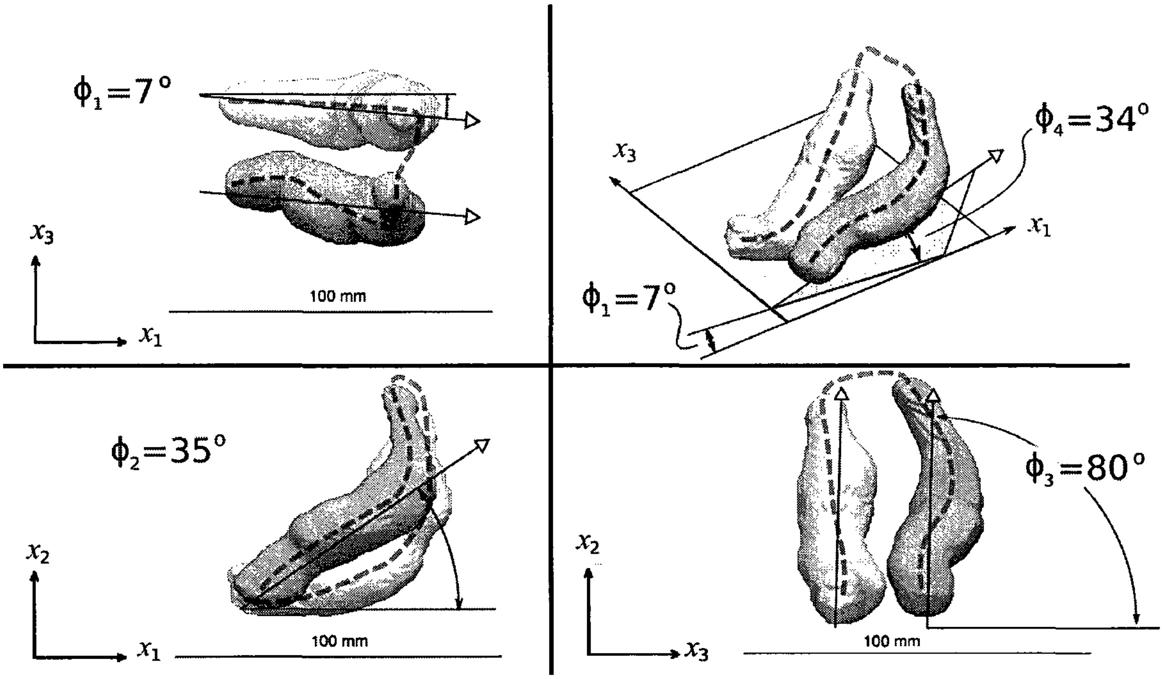

Figure 5.20: A 3D reconstruction of the scanned upright vortex pair from Figures 5.18 - 5.19. This pair is counter-rotating such as to induce a upwards flow between themselves. A dashed line indicates the likely 3D hairpin structure.

Mushroom-shaped vortex pairs were interpreted as the legs of hairpin vortices, similar to those identified in the turbulent boundary layer. The direction of rotation of the vortices was inferred by the direction of the entrained fluid between the pairs. Inverted, downwards-facing vortex pairs were observed rotating in the opposite direction of the type of hairpin that is typical in boundary layers. Furthermore, vortex pairs were observed to deviate from spanwise symmetry by as much as 30° from the $x_1 - x_2$ plane. They were also observed to be inclined upwards within a range of $45° \pm 25°$, irrespective of their directions of rotation or spanwise symmetries. This suggests that the hairpin vortices form at a wide range of angles in USF. The location of the head of the vortex was difficult to identify from the dye patterns. It is expected that the counter-rotating vortex pairs were connected by an arched head at the most downstream end of the pair. However, it is also possible that no connecting arch existed, or that it was located at the upstream end of the vortex pair. This would have to be investigated using other experimental means.

5.3 Hydrogen bubble flow visualisation results

With the hydrogen bubble visualisation technique, vortices can be easily observed as the bubbles are drawn towards the axes of the vortices by centrifugal forces because they are lighter than water. Bubbles cannot be used in excess so that the image is not cluttered; however, the flow is not visible where there are no bubbles. One advantage of flow visualisation using hydrogen bubbles is that the flow structures can be viewed from all directions and not only in one plane as with laser sheet visualisation.

5.3.1 Vertical wire configuration

In the first experimental configuration the cathode wire was placed in a vertical position, such that one arm of the wire holder was touching the bottom of the tunnel, and the centre of the wire was just below mid depth. Because of the length of the arms, the wire could not be placed in the centre of the tunnel, but it was positioned at about 50-100 mm off centre in the x_3 direction. The wire was place at about $x_1 =$ 2 m, and bubble images were recorded in the approximate range 2.0 m $< x_1 <$ 2.5 m $(5.6 < \tau < 7.0)$. Images were recorded at centreline velocities of about 0.16 m/s and 0.08 m/s.

Figure 5.21 shows typical timelines for the flow with $U_c = 0.08$ m/s. The image were taken very close to the wire before the bubbles lines had become fully mixed, and the wire is visible at the left-most edge of the frame. The velocity gradient is evident by the growing inclination of the timelines. High speed flow at the top of the image carried the bubbles downstream faster than the lower speed flow near the bottom. Moreover, the instantaneous timelines were not straight but contorted due to the turbulent velocity fluctuations. The most common vortical structures in this configuration were clockwise vortices, which appeared to have vorticity in the $-x_3$ direction. Figure 5.21 shows two large clockwise vortices, with diameters in the range of 20-30 mm as they begin to develop.

Figure 5.22 shows a frame sequence of timelines about 0.5 m downstream of the bubble wire, in the flow with $U_c = 0.16$ m/s. The timelines were widely spaced by decreasing the pulse frequency to the wire. The increased mixing in the higher speed flow increased the scattering of the bubbles, making the bubble timelines difficult

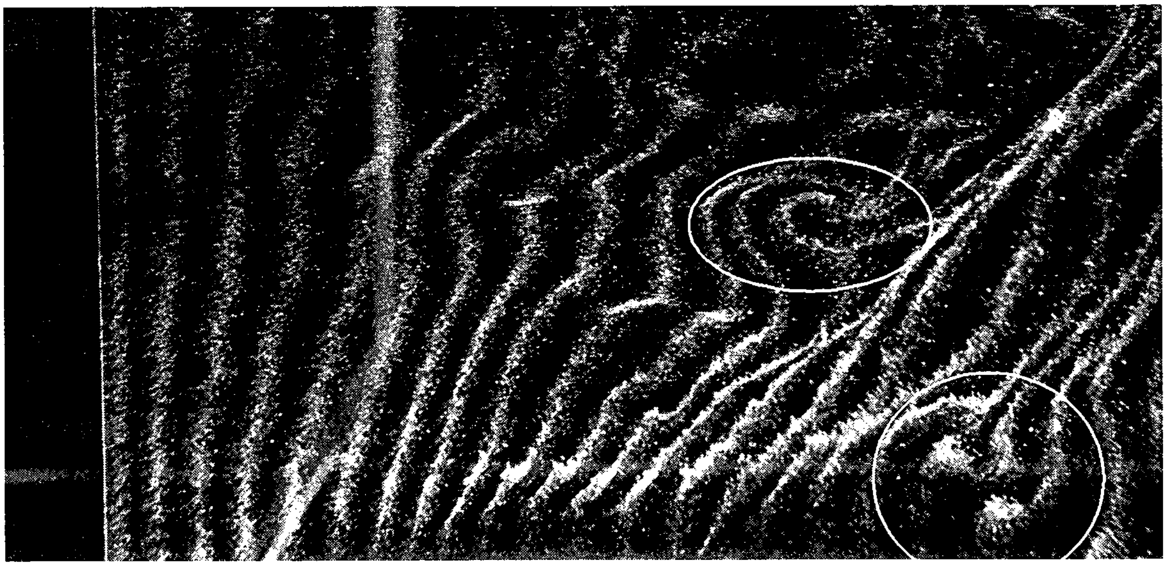

Figure 5.21: View from the side of the lower half of the vertical bubble sheet, where $U_c = 0.08$ m/s.

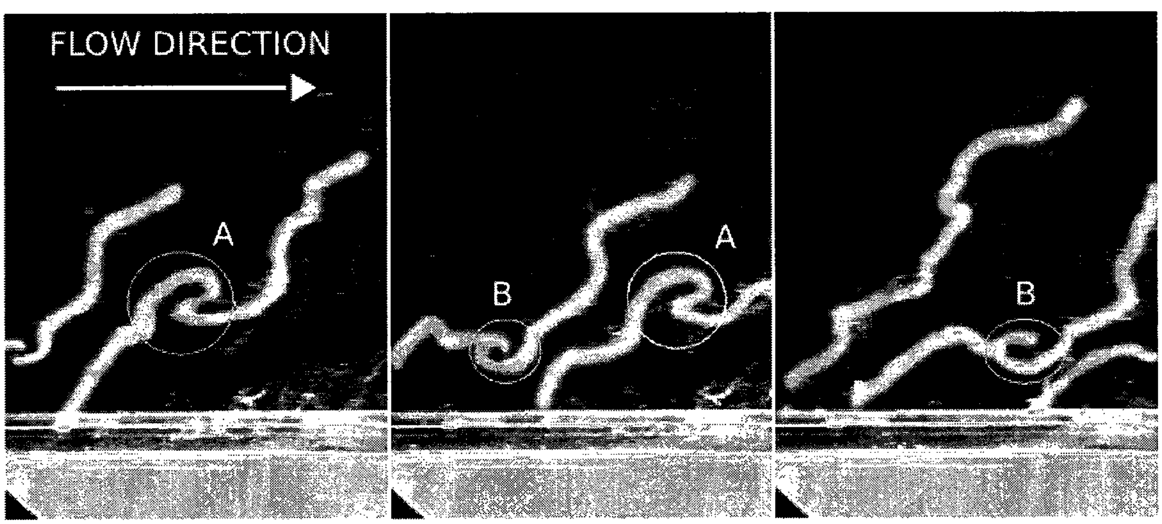

Figure 5.22: Frame sequence of the vertical bubble sheet in flow with $U_c = 0.16$ m/s. View is from the side of the vertical bubble sheet slightly below mid-depth, where timelines have been highlighted for clarity. Two clockwise vortices are identified, labelled A and B.

to follow visually because of their reduced concentrations of bubbles. The timelines have been highlighted for clarity in Figure 5.22, which shows that clockwise vortices were present in the higher speed flow as well. Furthermore, the instantaneous velocity profile inferred by the inclinations of the timelines showed that these vortices were located along shear layers, which were characterised by a steep gradient in the velocity. Both vortices were located along the same shear layer, as identified by the two timelines along which they were located. The third timeline, however, had a more uniform velocity gradient, illustrating the fact these shear layers were of relatively short streamwise length.

Further downstream, the timelines became increasingly mixed and the bubbles became highly scattered. Those sections of the timelines that remained coherent tended to be relatively short (about 20 mm) and were observed to form arches or vertical vortices (or combinations of both) that were stretched and contorted as they were convected downstream. These structures were better visualised in the horizontal wire configuration and are further discussed in the following subsection. The typical distance over which these structures could be identified was only about 200 mm ($\Delta\tau = 0.5$).

5.3.2 Horizontal wire configuration

In the second experimental configuration, the cathode wire was placed horizontally, spanning the width of the tunnel at a height just below mid-depth.

At $U_c = 0.16$ m/s, the bubbles were seen to quickly mix about 250 mm downstream of the wire. Figure 5.23 shows that timelines were convected at distances of approximately 26 mm. The timelines, which originated as straight lines, quickly formed wiggles within a downstream distance of about 100 mm. Mixing was not as strong at $U_c = 0.08$ m/s, as shown in Figure 5.24, in which timelines were only separated by about 13 mm.

Figure 5.25 provides a close view of the downstream bubbles for $U_c = 0.08$ m/s. This image contains evidence of the presence of horseshoe-shaped vortices. The legs of these structures were identified by the quasi-streamwise alignment of bubble lines across several timelines. The heads of the structures were clearly identified in the

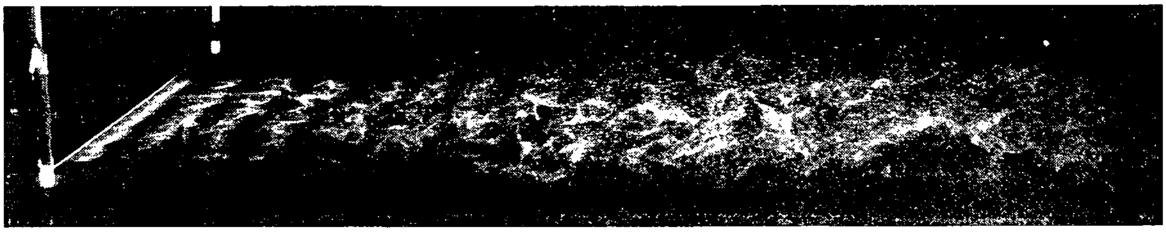

Figure 5.23: View from the side, looking down at the bubble sheet, with $U_c = 0.16$ m/s. Timelines are approximately 26 mm apart.

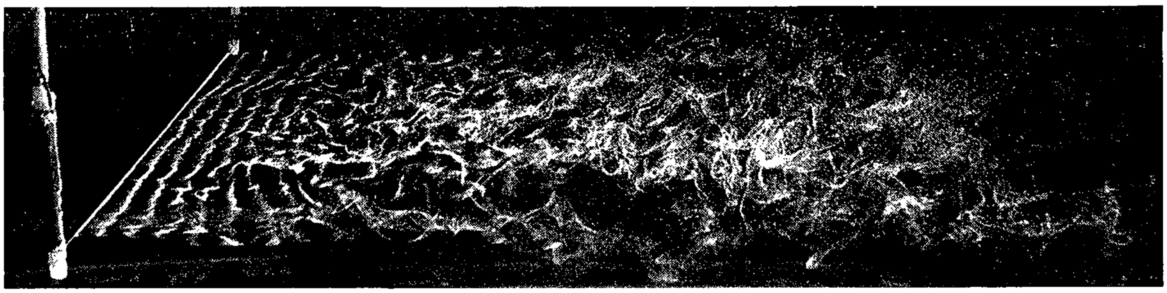

Figure 5.24: View from the side, looking down at the bubble sheet, with $U_c = 0.08$ m/s. Timelines are approximately 13 mm apart.

bubble patterns and resembled arches that were connected to elongated legs. Three horseshoe shapes were identified in this image, roughly aligned in the streamwise direction. The vertical orientation of these structures is difficult to discern from the figure, but it appeared that they were typically inclined upwards by roughly 45° with respect to the x_1-direction. As the structures traveled downstream, they continued stretching along the +45° inclined plane until the bubble lines became very thin and they could no longer be identified. The length of the structures varied from 40 to 80 mm, and the spacing of the legs was on average about 30 mm.

Horseshoe structures were also identified for the flow with $U_c = 0.16$ m/s, as illustrated in Figures 5.26 and 5.27. These structures were much more difficult to identify than in the lower speed flow because the mixing was stronger in the higher speed flow. Furthermore, the horseshoe structures were on average both narrower and shorter than in the lower speed flow, although they were more frequent. The structures appeared in a range of sizes, with a typical leg spacing varying between 5 and 20 mm, though some large structures had a width of up to 50 mm. The structures often spanned several timelines, with typical lengths in the range of 20 to 30 mm,

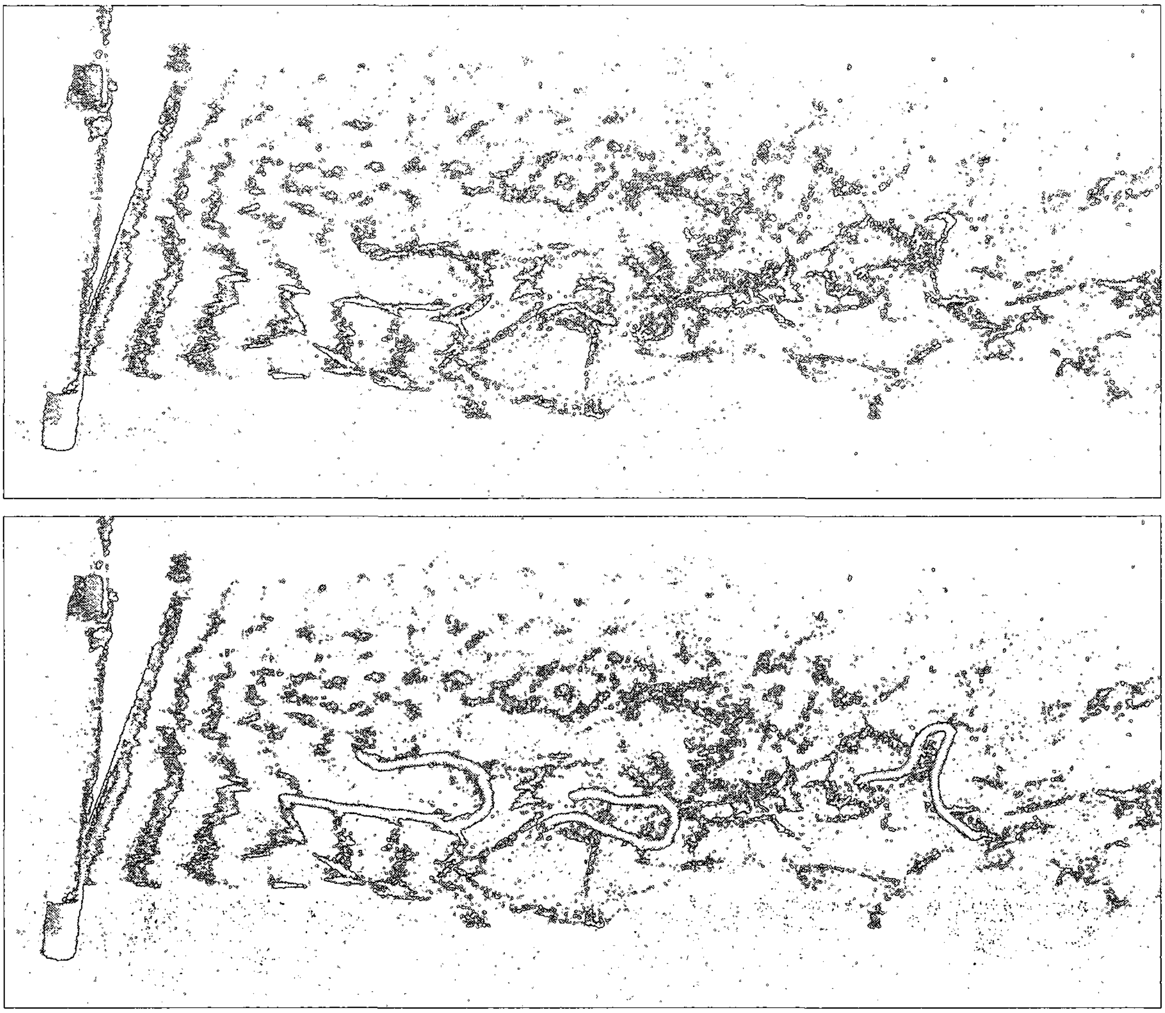

Figure 5.25: View from the side of the horizontal bubble sheet, with $U_c = 0.08$ m/s. The locations of several hairpin-shaped vortices are identified in the lower copy of the image.

however some structures reached lengths of up to 60 mm. The structures appeared in different forms, sometimes with only one leg, sometimes with more than one arch, and sometimes facing in directions other than forward.

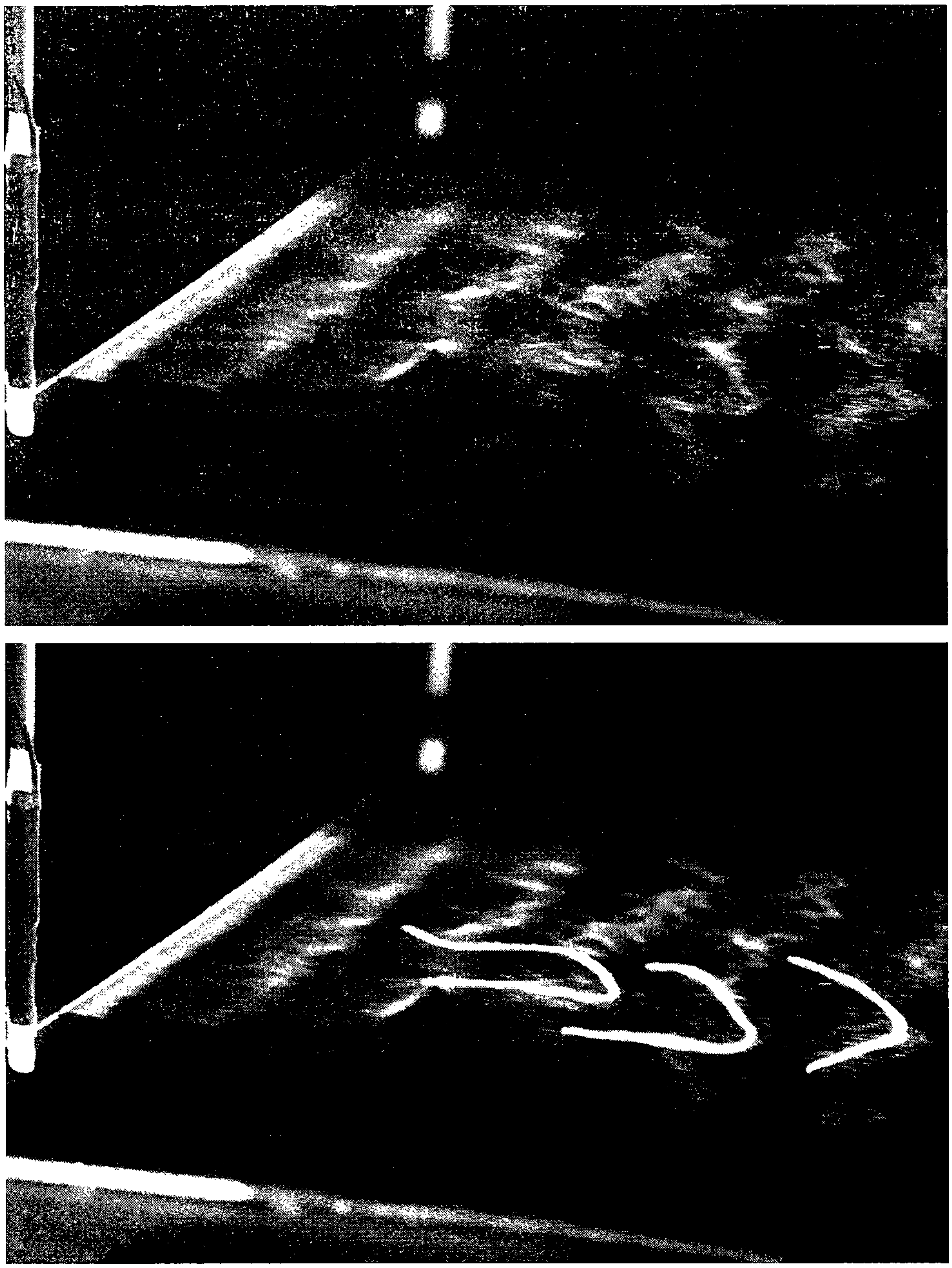

Figure 5.26: View from the side of the horizontal bubble sheet, with $U_c = 0.16$ m/s. The locations of several hairpin-shaped vortices are identified in the lower copy of the image.

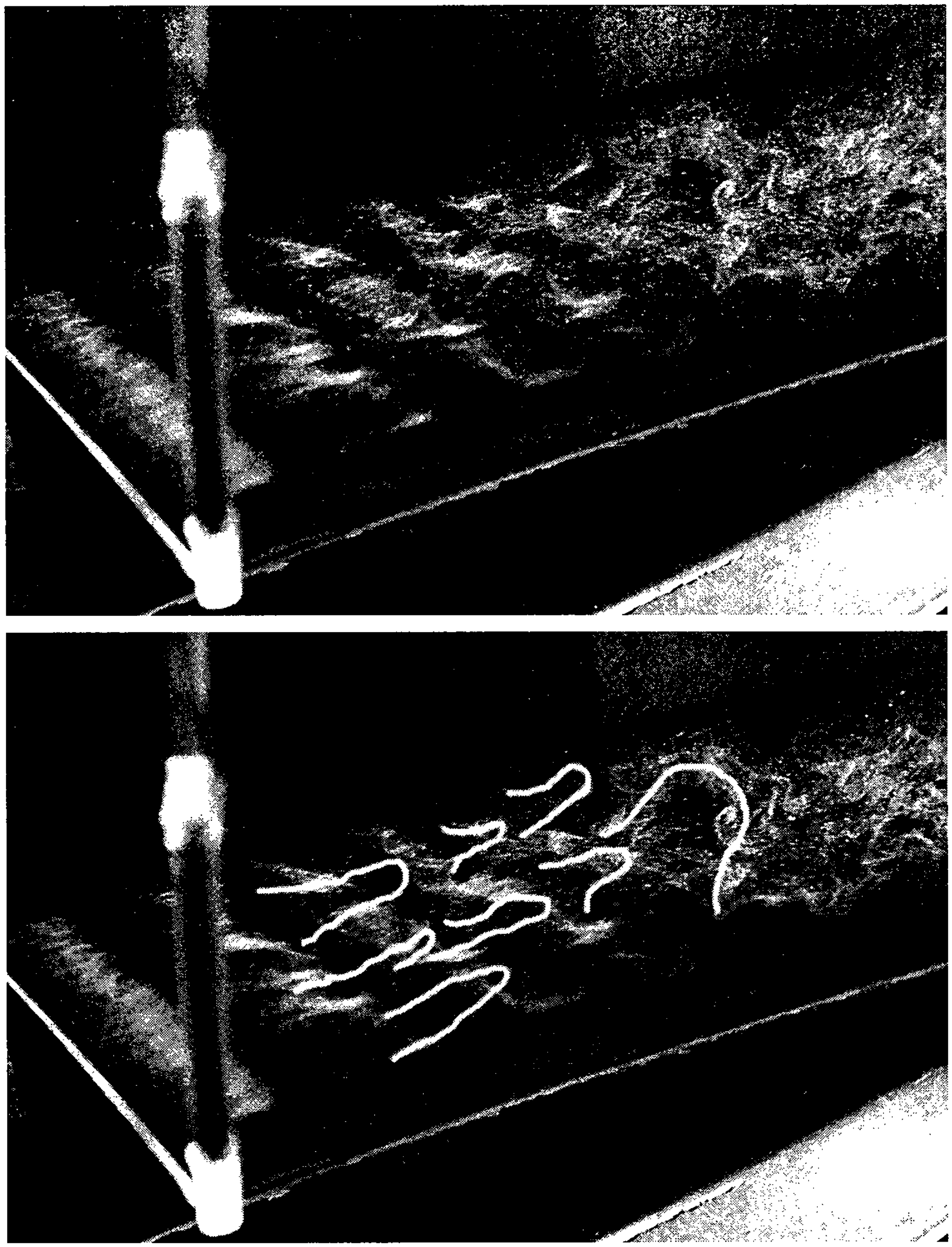

Figure 5.27: View from the side of the horizontal bubble sheet, with $U_c = 0.16$ m/s. The locations of several hairpin-shaped vortices are identified in the lower copy of the image.

5.4 Particle image velocimetry results

Particle image velocimetry (PIV) was used to record instantaneous flow fields. This method only provides information in a single plane at a time, but measurements were collected in a vertical, a horizontal, and an inclined plane. All of the measurements were taken in the fully-developed region near $x_1 = 2$ m ($\tau = 5.6$) and $x_2/h = 0.5$, with the exception of some exploratory investigations that were conducted near the exit of the flow separator in the vertical configuration. These results are presented in separate subsections, in which the typical flow structures that could be identified in each case are discussed. Statistics were collected of the strength and size distributions of the typical vortices found in each configuration. In the case of the horizontal and inclined configurations, counter-rotating vortex pairs were found to be fairly common and so their properties were recorded as well.

PIV results can be displayed using vector maps or contour maps of scalars such as the streamwise velocity component, normal vorticity component, 2D swirling strength, and rate of strain tensor components. Examples of these maps are displayed in Figure 5.28. These show a typical vortex in the vertical plane, with the flow from left to right. The velocity vectors have been offset so that the large central vortex becomes apparent. The velocity map shows a sudden change in velocity at about the same location as the vortex identified by the relative velocity vectors. The vorticity magnitude peaks at approximately the centre of the vortex, which coincides with the location of the swirling strength peak. The rate of strain map also clearly shows a region with a sudden velocity change. In order to concisely present the results in a single map, only the velocity vectors within the cores of vortices are displayed, superimposed on contour maps of the streamwise velocity field, as in Figure 5.28f. The velocity vectors are offset by the mean convection velocity of each vortex, which was calculated as the average absolute velocity within the vortex core. The identified vortices are enclosed by black ellipses if rotating clockwise (CW) and white ellipses if rotating counter-clockwise (CCW). This format was used for all of the subsequent PIV flow fields.

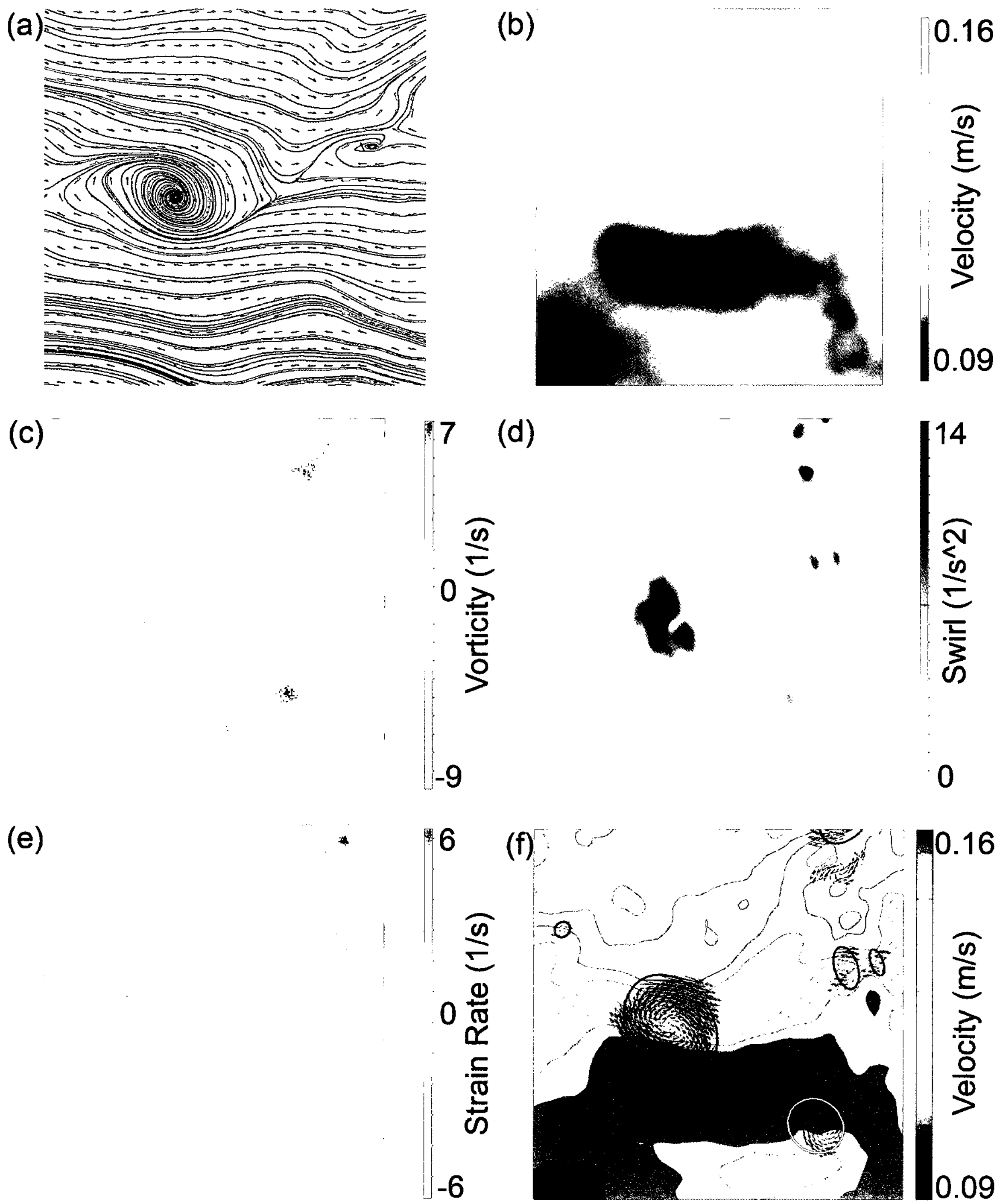

Figure 5.28: Sample PIV output for a typical vortex in the vertical plane: (a) streamlines in a convected frame matching the velocity of the large central vortex, (b) velocity map with vectors in a convected frame, (c) vorticity map, (d) swirling strength map, (e) strain rate, and (f) output of the matlab vortex identification algorithm showing discrete vortices superimposed on the velocity map.

5.4.1 Vertical plane measurements

The vertical measurement plane was parallel to both the streamwise velocity vector and the direction of the velocity gradient. PIV measurements were recorded at three positions, having x_1 = 0.10 m, 0.40 m, and 1.9 m, corresponding to dimensionless development times of $\tau = 0.3$, 1.1, and 5.2 when $U_c = 0.16$ m/s. All images were taken in the midplane of the tunnel at $x_3 = 0$. In most cases $U_c = 0.16$ m/s; however, at the downstream position of $x_1 = 1.9$ m measurements were also taken for a centreline velocity of approximately 0.12 m/s.

Measurements at the beginning of the test section at $\tau = 0.3$ (Figure 5.29) show that the velocity profile at the exit of the flow separator was not at all linear or smooth. Four zones of high speed, located at depths of $x_2/h = 0.41$, 0.48, 0.55, and 0.61, corresponded to the streams exiting the individual channels of the flow separator. These high-speed zones were separated by lower-speed zones, which were the wakes of the glass plates of the flow separator. Roughly equal numbers of clockwise and counter-clockwise vortices were generated at the interfaces of the wakes and jets. These vortices had a mean diameter of 5.8 mm, which corresponds to roughly one quarter of the spacing between the glass plates in the flow separator.

At the downstream position of $\tau = 1.1$ (Figure 5.30), the vertical velocity profile was considerably smoother. The concentration of vortices at $\tau = 1.1$ was nearly half that at $\tau = 0.3$. The vortices at $\tau = 1.1$ had approximately the same mean diameter as at $\tau = 0.3$, but their mean strength was reduced significantly. The numbers of clockwise and counter-clockwise vortices were no longer equal, with the counter-clockwise vortices being significantly fewer.

At a downstream distance of $\tau = 5.2$, the velocity profile was much smoother, as illustrated in Figure 5.31. Although the time-averaged velocity profile was linear at this downstream position, as previously presented in Section 5.1.1, the instantaneous velocity profile was somewhat stepwise. The instantaneous velocity field tended to form zones of roughly uniform velocity, separated by thin shear layers with large velocity gradients. The zones of roughly uniform velocity appeared at different vertical positions, such that the shear layers appeared as ramps separating these zones. These shear layers did not line up horizontally with the plates in the flow separator. Large

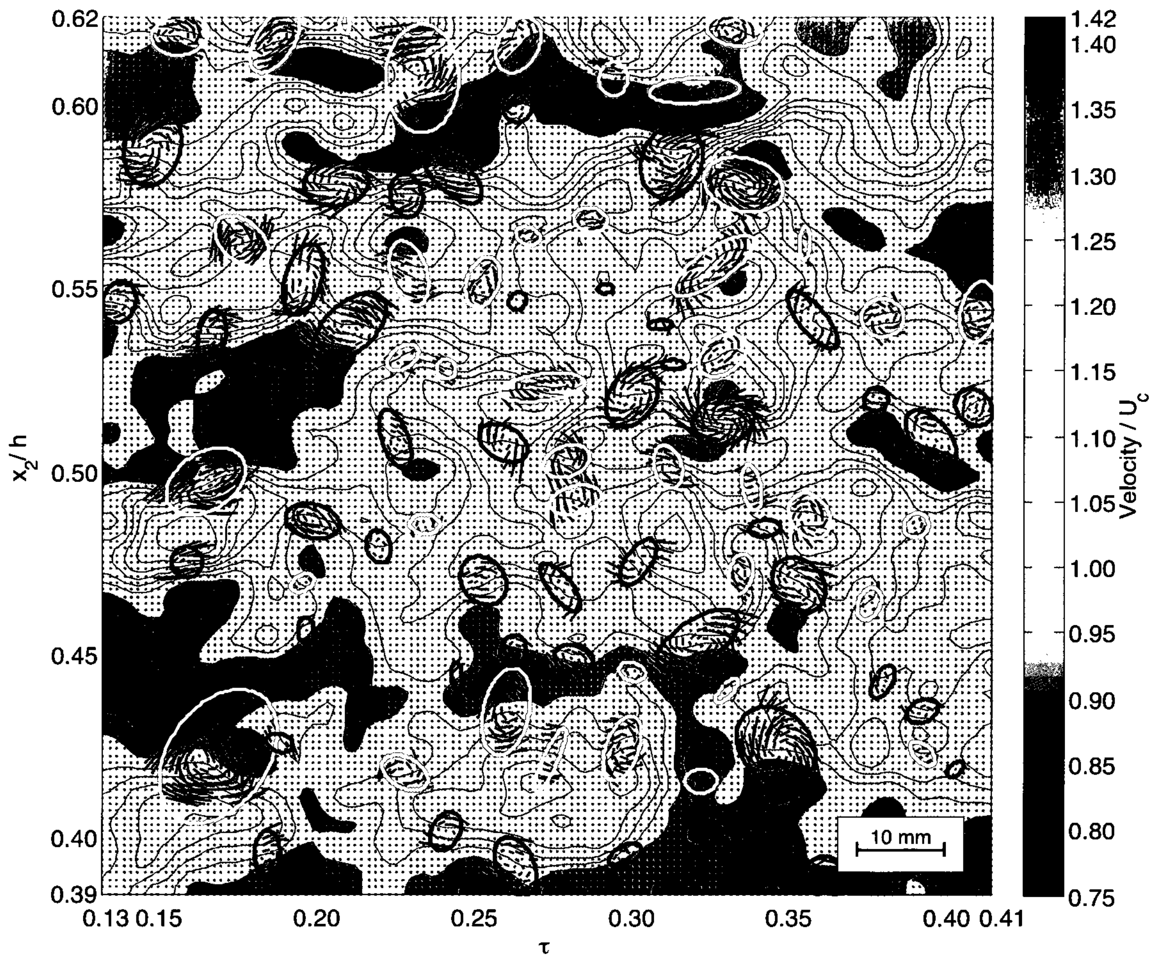

Figure 5.29: Sample velocity map in a vertical streamwise plane at τ = 0.3. Flow is moving from left to right. Vortices are identified by the surrounding vectors relative to the vortex convection velocity and are enclosed by drawn black ellipses if turning CW and white ellipses if turning CCW.

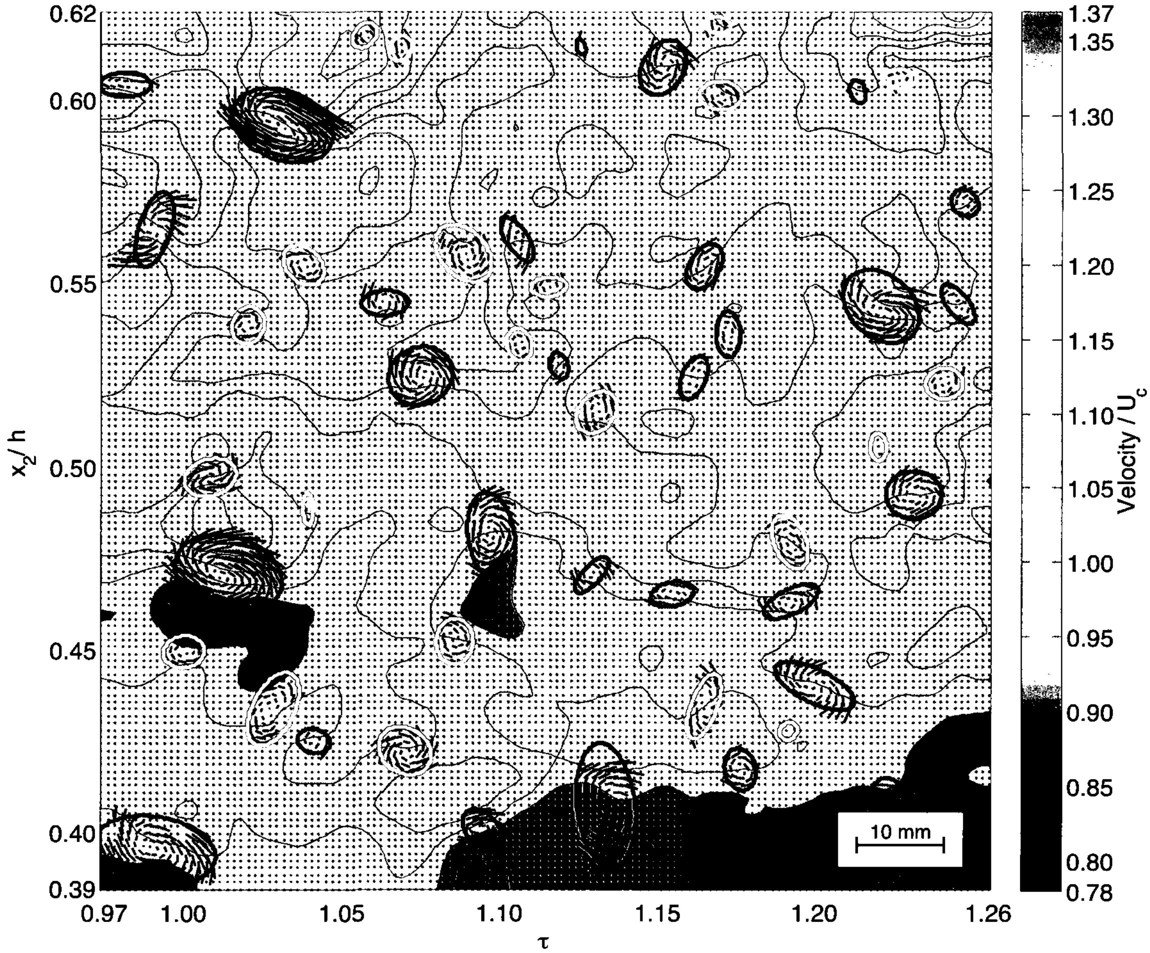

Figure 5.30: Sample velocity map in a vertical streamwise plane at $\tau = 1.1$. Vortices are identified by the surrounding vectors relative to the vortex convection velocity and are enclosed by drawn black ellipses if turning CW and white ellipses if turning CCW.

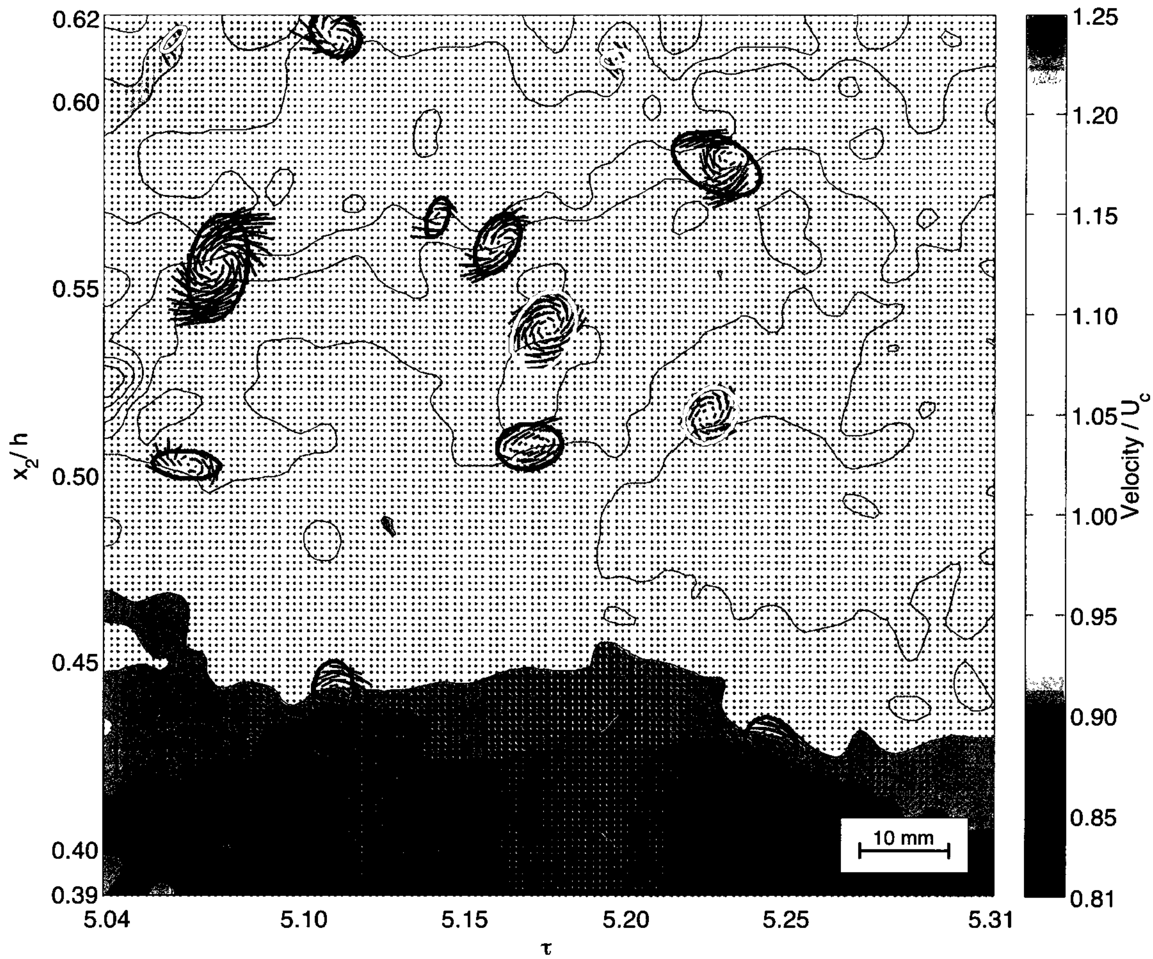

Figure 5.31: Sample velocity map in a vertical streamwise plane at $\tau = 5.2$. Vortices are identified by the surrounding vectors relative to the vortex convection velocity and are enclosed by drawn black ellipses if turning CW and white ellipses if turning CCW.

Plane	Vertical				Horiz.	Inclined
x_1 (m)	0.1	0.4	1.9	1.9	1.9	2.2
τ	0.3	1.1	5.2	-	5.2	6.1
U_c (m/s)	0.16	0.16	0.16	0.12	0.16	0.16
Average number of vortices[a]	84	49	35	13	39	15.5
% of clockwise vortices	54	63	76	76	50	56
Mean vortex strength[b] (mm^2/s)	178	98	55	92	159	165
Max. vortex strength[b] (mm^2/s)	1242	715	416	866	1029	1184
Mean vortex diameter (mm)	5.8	5.9	4.9	6.8	11.7	12
Max. vortex diameter (mm)	21.2	21.1	20.7	23.4	45	38

[a]per 100 mm x 100 mm viewing area
[b]regardless of direction of rotation

Table 5.3: Properties of vortices in the three PIV planes.

clockwise vortices were found to be common along these shear layers. Some counter-clockwise vortices also appear in the flow, always at locations where the velocity gradient was inverted, which occurred when a region of high-speed fluid appeared under a region of low-speed fluid.

The same patterns were even more clearly visible in the lower speed flow (U_c = 0.12 m/s), as illustrated in Figure 5.32. The shear layers were separated by larger depths and had larger velocity gradients, roughly 5 s^{-1}, compared to about 2 s^{-1} in the flow with $U_c = 0.16$ m/s. The clockwise vortices that formed along the shear interfaces were less frequent but were much stronger, with a mean strength almost twice that found at $U_c = 0.16$ m/s. Larger regions of high speed fluid were observed in low speed areas with greater frequency, with the result that the counter-clockwise vortices were slightly more frequent and stronger than those at $U_c = 0.16$ m/s. The average vortex concentrations and the mean and maximum absolute vortex strengths and diameters from all of the measurement configurations are summarised in Table 5.3.

In all cases vortices were very abundant and could be identified in every PIV map; however, their properties changed with downstream position. The average number of vortices along with each vortex's size and strength were recorded for each measurement position. All measurements in the vertical plane used the same swirling strength threshold values in order to allow comparison of the results at different downstream positions. These results are summarised in Table 5.3 and presented graphically in

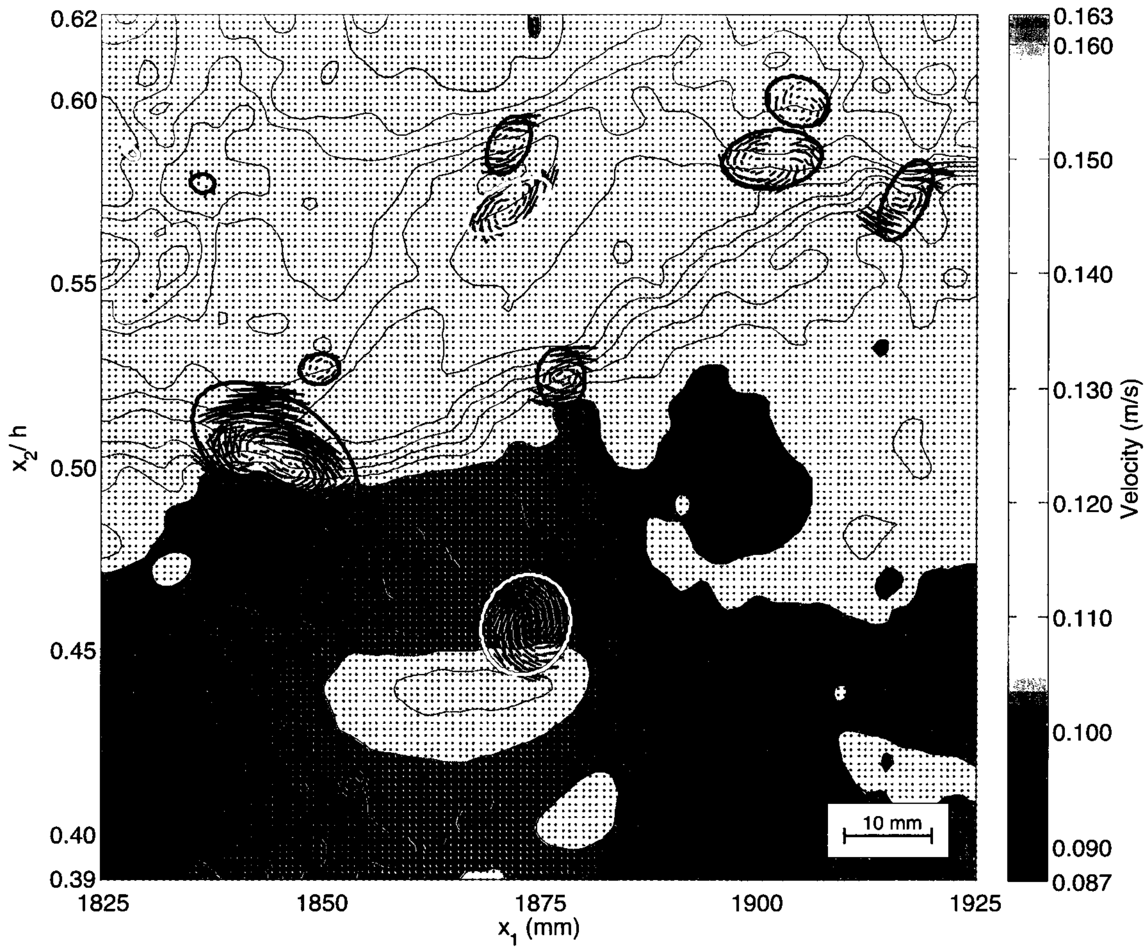

Figure 5.32: Sample velocity map in the vertical configuration at $x_1 = 1.9$ m with a reduced flow rate. Vortices are identified by the surrounding vectors relative to the vortex convection velocity and are enclosed by drawn black ellipses if turning CW and white ellipses if turning CCW.

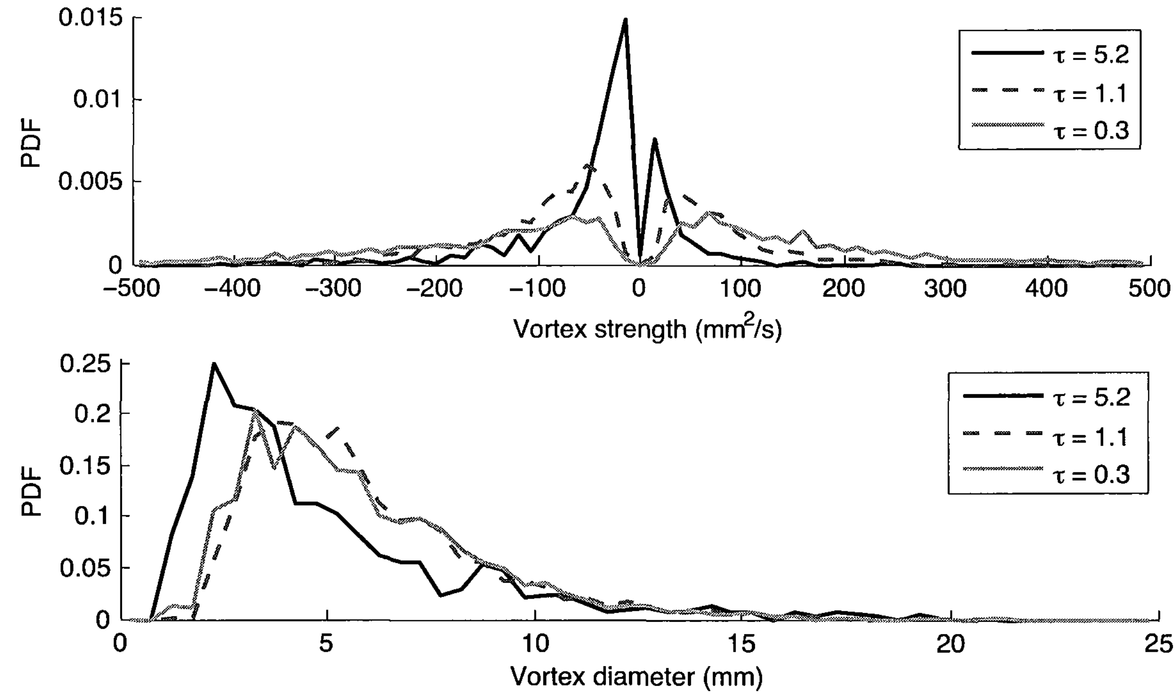

Figure 5.33: Measured probability density functions of the vortex strength and diameters at three downstream positions for $U_c = 0.16$ m/s. Negative vortex strength corresponds to a vortex with CW rotation.

Figure 5.33. The bin sizes of the probability density functions were carefully chosen to optimize the measurement resolution while ensuring that all bins contained sufficient samples. These results indicate that the mean strengths and sizes of the vortices decreased with downstream distance. The distribution of the vortex diameters at $\tau = 5.2$ shows that a small population of vortices still exists in a range from 8 to 9 mm.

5.4.2 Traversing measurements in the vertical plane

Some traversing measurements were collected as an extension of the vertical plane setup, to track the vortices formed at the shear generator through the flow. The goal was to see whether quasi-two-dimensional vortices generated at the exit of the flow separator died out and new structures formed before the end of the tunnel.

A sample frame sequence following vortices in the range with $0.6 < \tau < 1.8$ near the beginning of the test section is presented in Figures 5.34 and 5.35. A similar frame sequence recorded near the centre of the test section in the range with $4.7 < \tau < 6.5$ is presented in Figures 5.36 to 5.38. The ranges of the recordings were limited by the memory capacity of the PIV or were interrupted by the frame of the water tunnel, which blocked the view in the range 0.65 m $< x_1 <$ 0.83 m ($1.8 < \tau < 2.3$).

These velocity maps agree with those in the fixed frames. A large amount of vortices were observed near the exit of the flow separator. As the flow moved downstream, the smaller vortices died out, presumedly due to viscous dissipation, and the larger vortices began to become organized, which resulted in a much more structured vortex map. The larger vortices were sometimes observed to merge with other vortices or to break down. The merging of several vortices would result in a large strong vortex, and the splitting of vortices would result in many of the fragmented vortices dying out due to viscous dissipation. Some instances of these events are labelled in the frame sequence of Figures 5.36 to 5.38. The large vortices were rarely observed to be generated spontaneously, but instead they were usually related to a large vortex that was generated by the shear generator. The vortices observed downstream seem to have been generated at the beginning of the test section and then reorganized.

The velocity fields in these frame sequences also developed in conformity with those in the fixed frames. The flow pattern started out with alternating jets and wakes at the exit of the flow separator. Although the velocity profile became smoother with streamwise distance, many areas of slow speed flow were found above higher speed areas, in such a way as to create a local velocity gradient that was opposite to the mean gradient. These areas corresponded to wake regions originating at the flow separator. As the flow moved downstream, shear layers between high and low speed regions gradually spread and the local low speed regions eventually disappeared. The shear layers appeared at a range of depths and appeared to have a ramp-like shape in the convected frame, similar to the observations of shear layer in the turbulent boundary layer [1]. The large vortices were always located within strong shear layers.

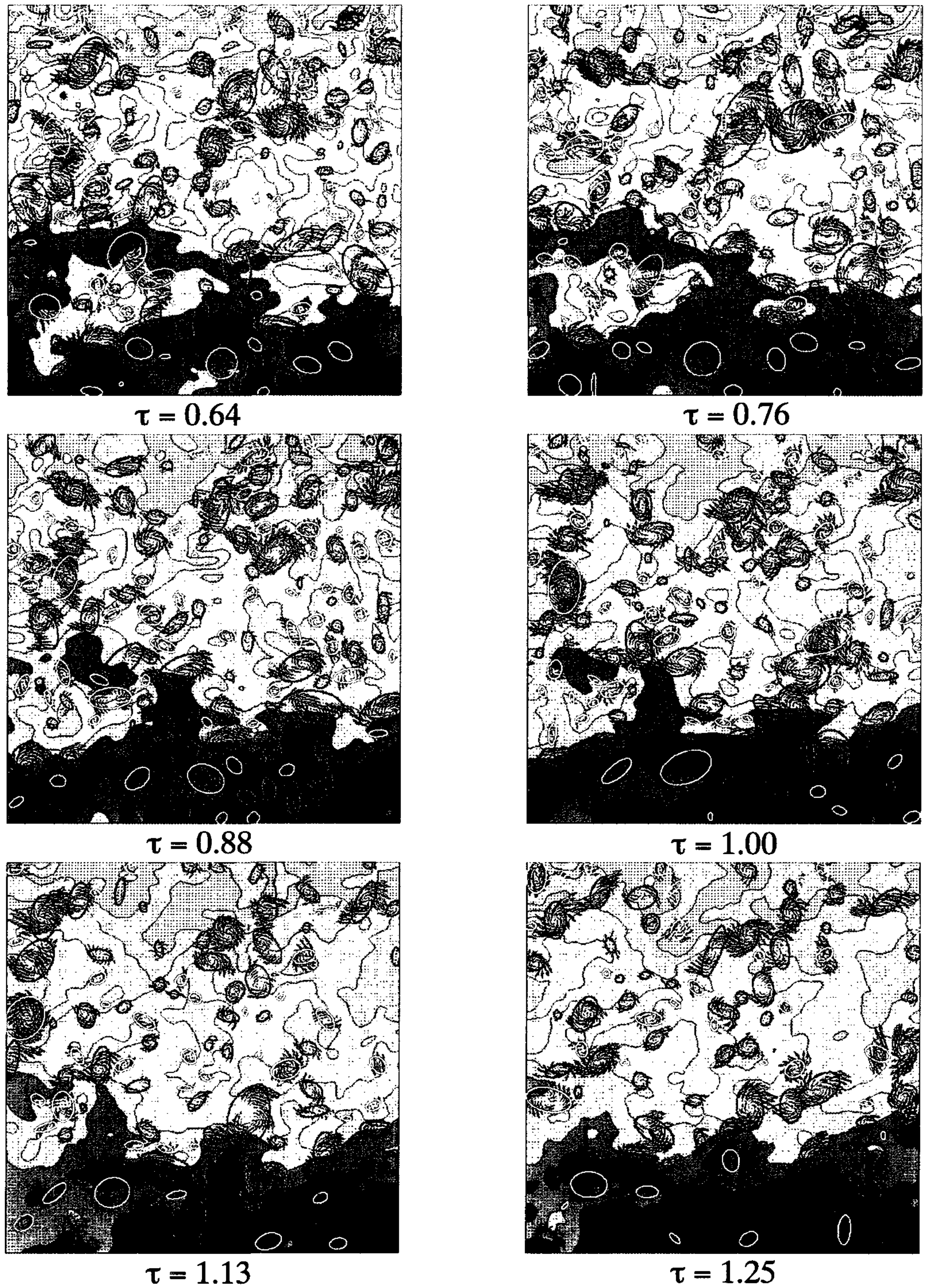

Figure 5.34: Frame sequence 1/2 of a traversing recording near the beginning of the test section.

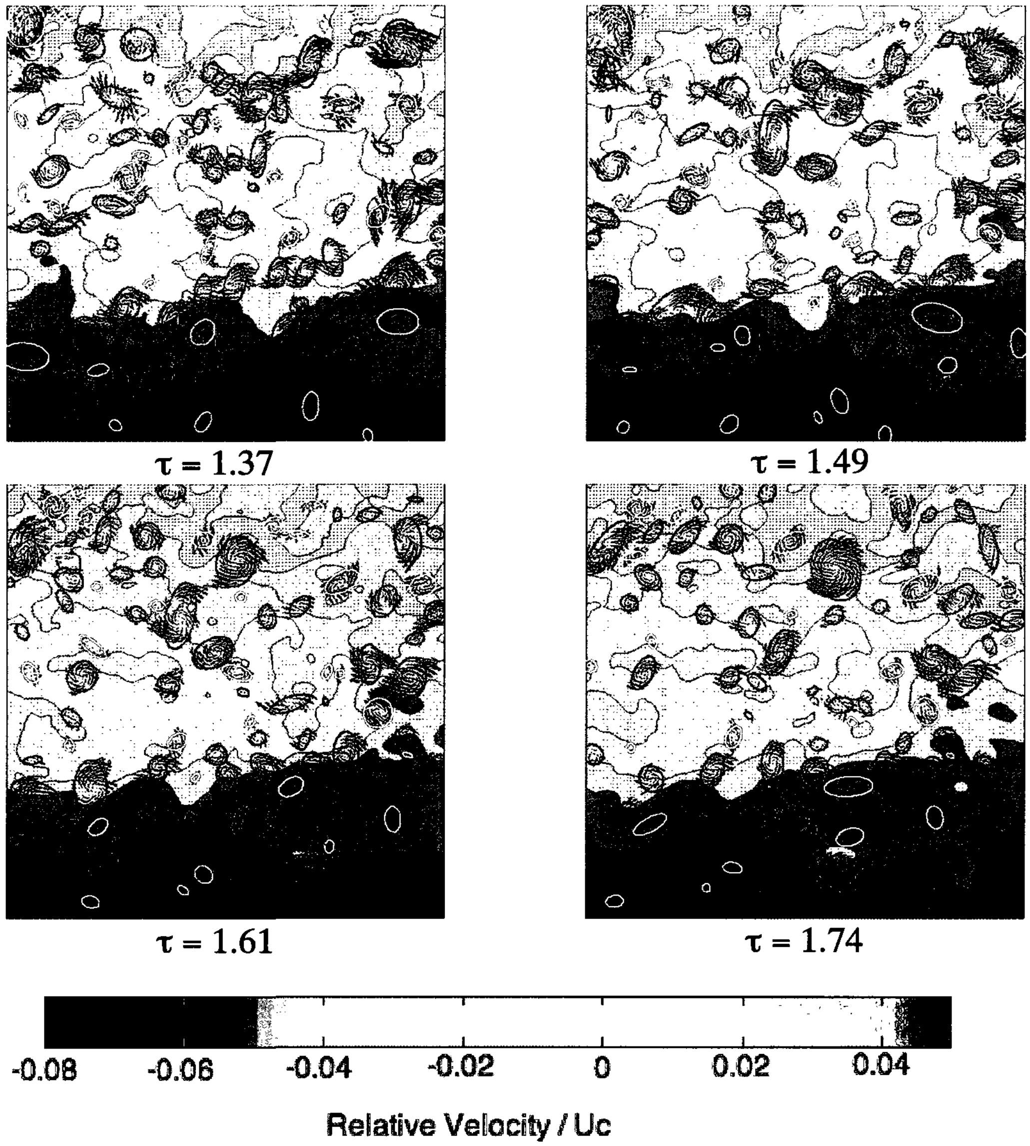

Figure 5.35: Frame sequence 2/2 of a traversing recording near the beginning of the test section, centred at a height of $x_2 = 0.5$ and the same scale as Figures 5.29 to 5.32. Vortices are identified by the surrounding vectors relative to the vortex convection velocity and are enclosed by black ellipses if turning CW and white ellipses if turning CCW.

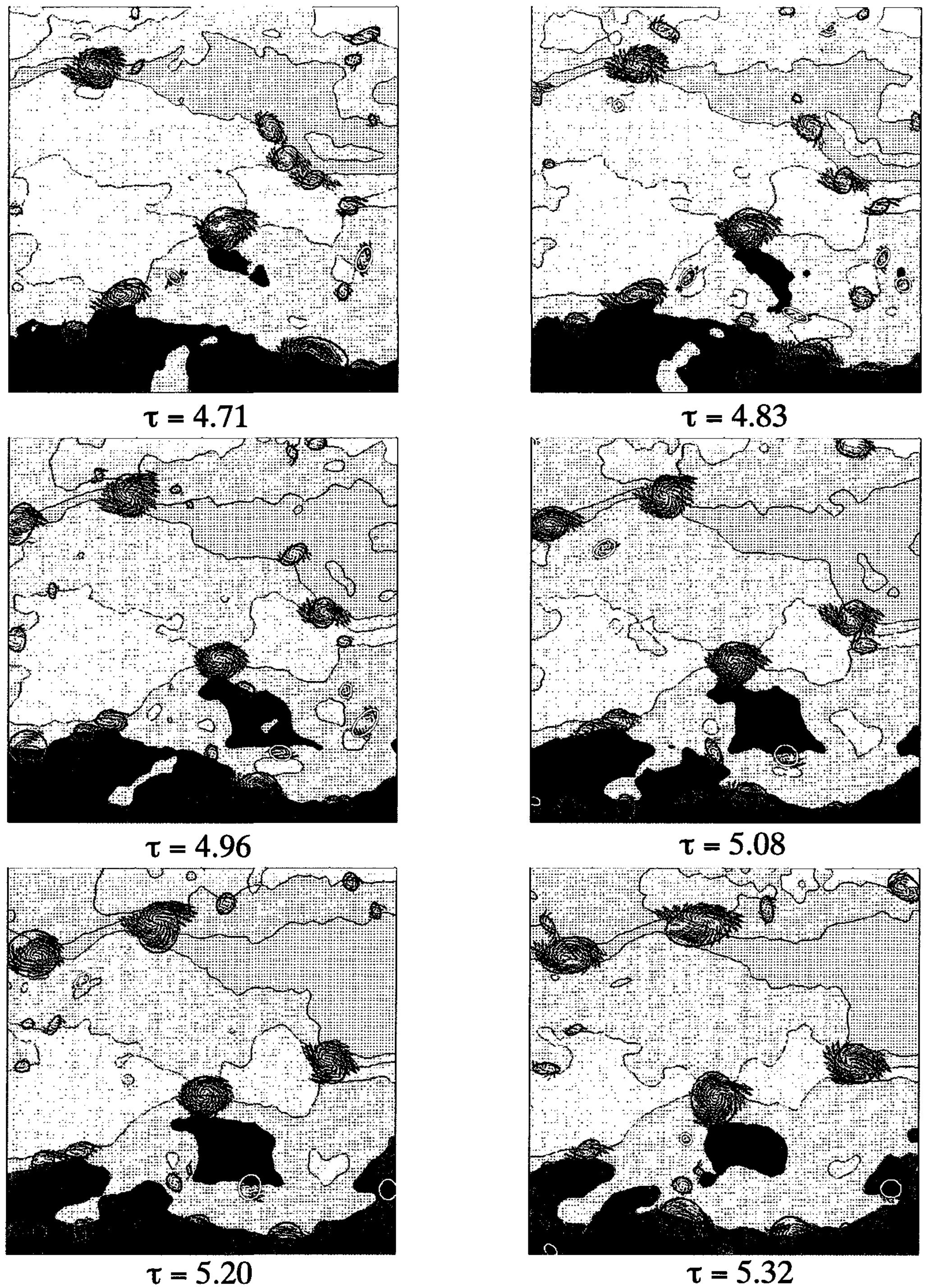

Figure 5.36: Frame sequence 1/3 of a traversing recording near the centre of the test section.

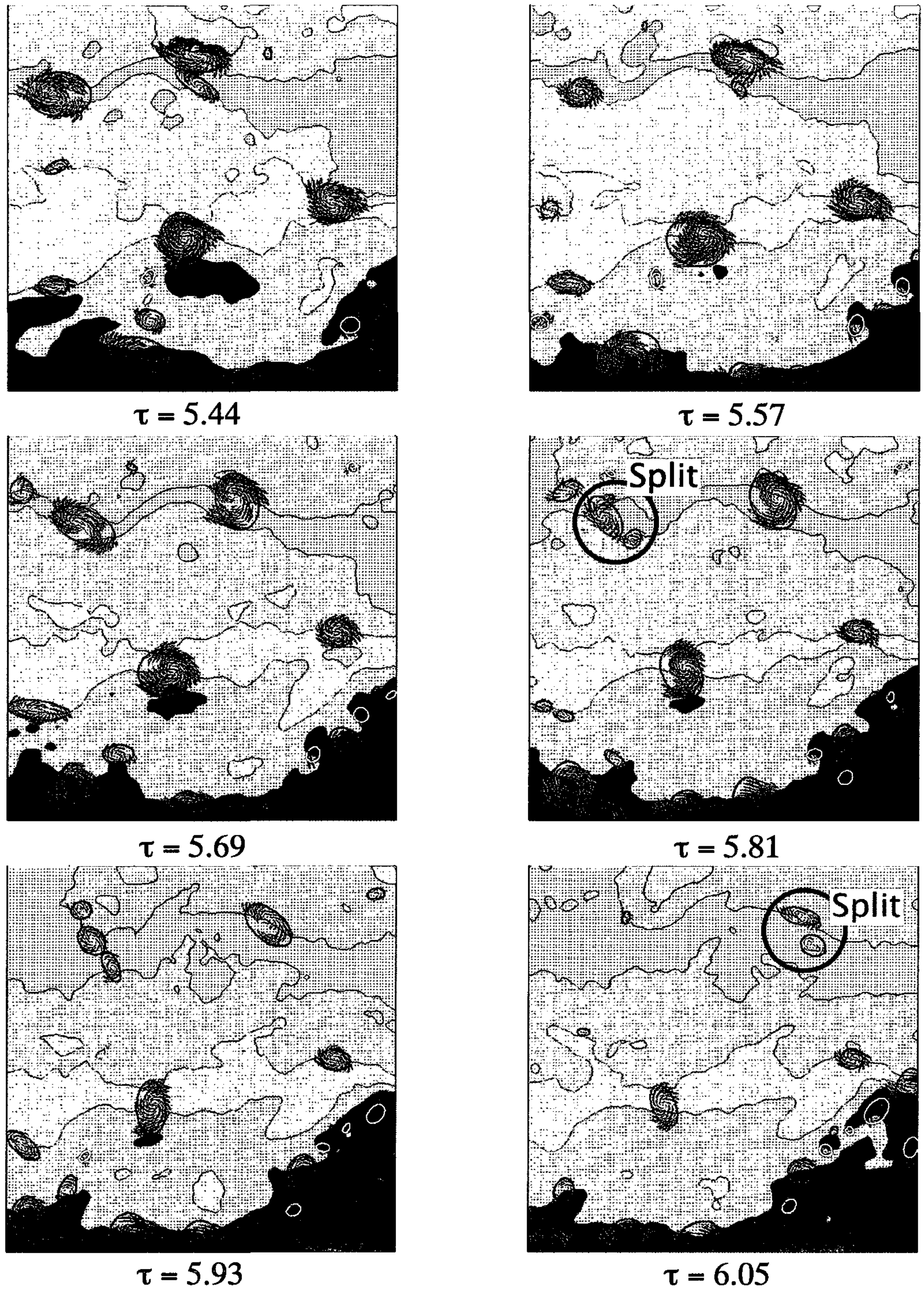

Figure 5.37: Frame sequence 2/3 of a traversing recording near the centre of the test section.

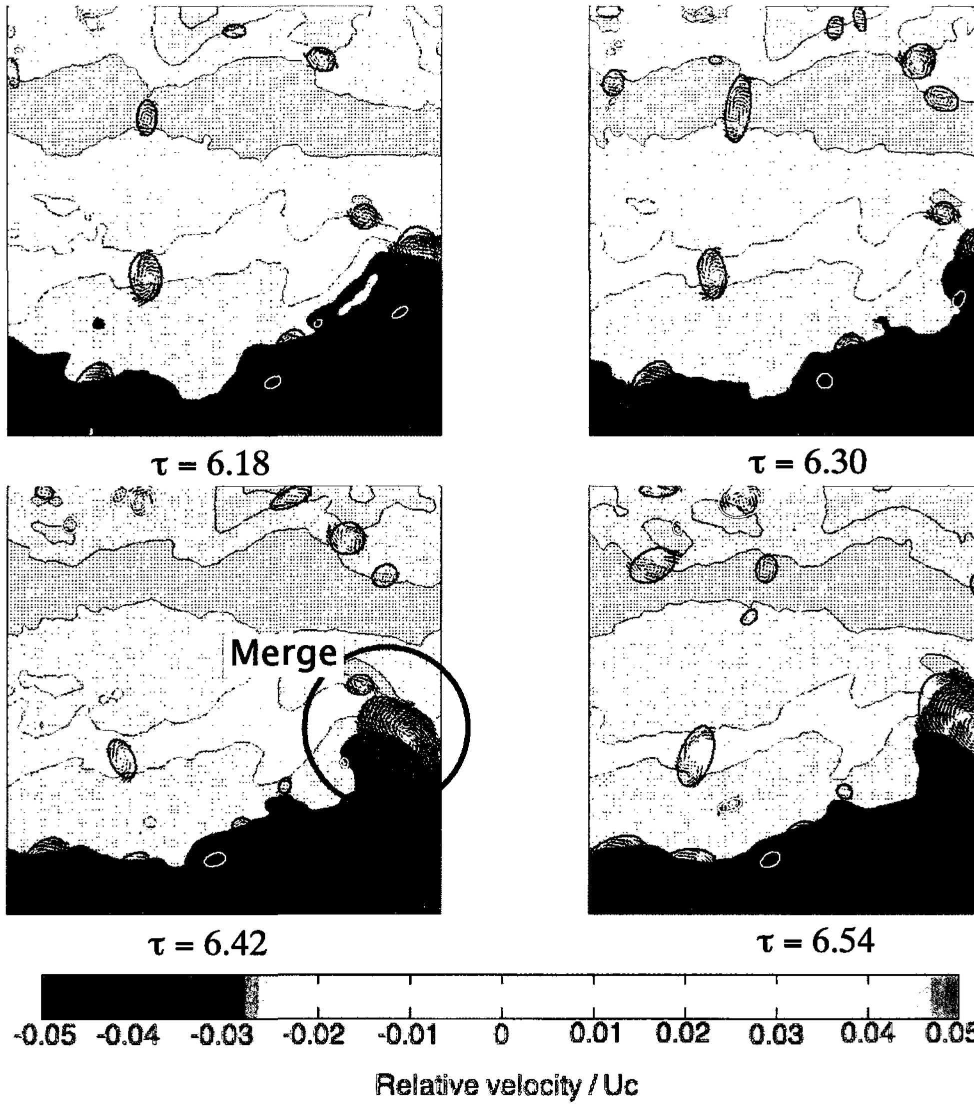

Figure 5.38: Frame sequence 3/3 of a traversing recording near the centre of the test section, centred at a height of $x_2 = 0.5$ and the same scale as Figures 5.29 to 5.32. Vortices are identified by the surrounding vectors relative to the vortex convection velocity and are enclosed by black ellipses if turning CW and white ellipses if turning CCW. Two splitting events and a merger event have been highlighted within bold circular outlines.

5.4.3 Horizontal plane measurements

The horizontal measurement plane was parallel to the streamwise velocity vector and perpendicular to the direction of the velocity gradient. Measurements were recorded in the horizontal plane near the centre line of the test section ($x_2/h = 0.56$, $x_3 = 0$). Flow patterns in the horizontal plane were easier to analyse than those in the other planes because the mean velocity was uniform in this plane, making it easier to identify and track vortices in the image.

The velocity field in the horizontal plane was characterised by low and high-speed streaks, elongated in the streamwise direction. The streaks were typically 100 mm long and were not limited to a given spanwise position. Vortices were found between the streaks, coinciding with relatively large spanwise gradients of the streamwise velocity. An example flow field is presented in Figure 5.39.

The concentration and strengths of the vortices in the horizontal plane were very different from those in the vertical plane. Most of the vortices travelled at the average convection velocity, often lining up in the streamwise direction between low and high-speed streaks. There were roughly an equal number of clockwise and counter-clockwise rotating vortices. The sizes of the vortices were larger than those in the vertical plane, and had a mean diameter of 10 mm. These statistics are summarised in Table 5.3 and in Figure 5.40.

Some clockwise vortices can be paired with counter-clockwise vortices located across the low or high-speed streaks. The previously described pair-matching algorithm was applied in order to help determine vortex pairs free of subjective bias. An example of the result of this pair-matching algorithm is presented in Figure 5.39, in which the vortex pairs are connected by solid black lines. The algorithm matched an average of 9 pairs per frame. The probability distribution of the angle of the pair, presented in Figure 5.40, suggests that there was a wide range of orientations of the vortex pairs. A small peak in the PDF occurs near 180°, which corresponds to the clockwise vortices occurring on the right side of the pair and is associated with the high-speed streak.

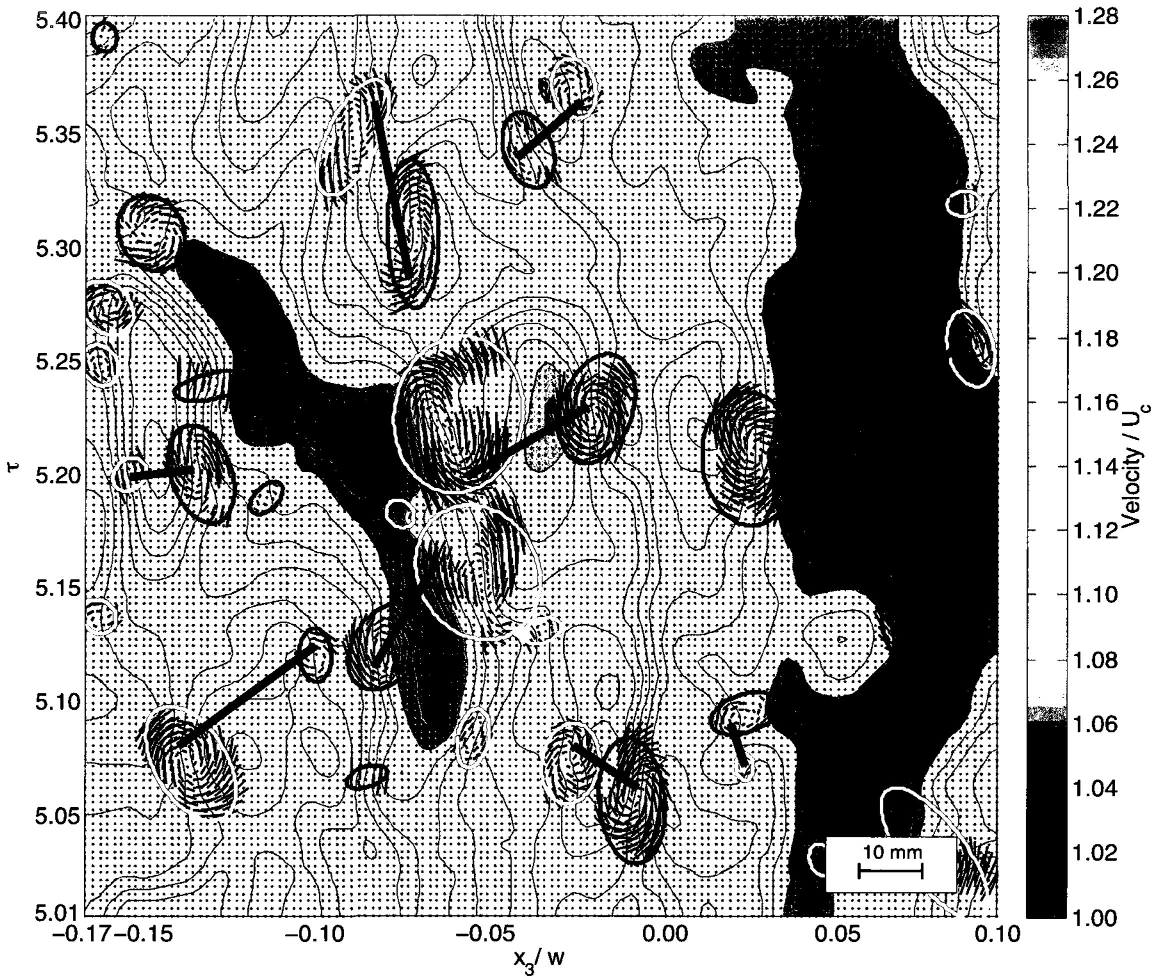

Figure 5.39: Sample velocity map in the horizontal streamwise plane. Flow is moving from bottom to top. Vortices are identified by the surrounding vectors relative to the vortex convection velocity and are enclosed by drawn black ellipses if turning CW and white ellipses if turning CCW. Pairs identified by the matching algorithm are connected by solid black lines.

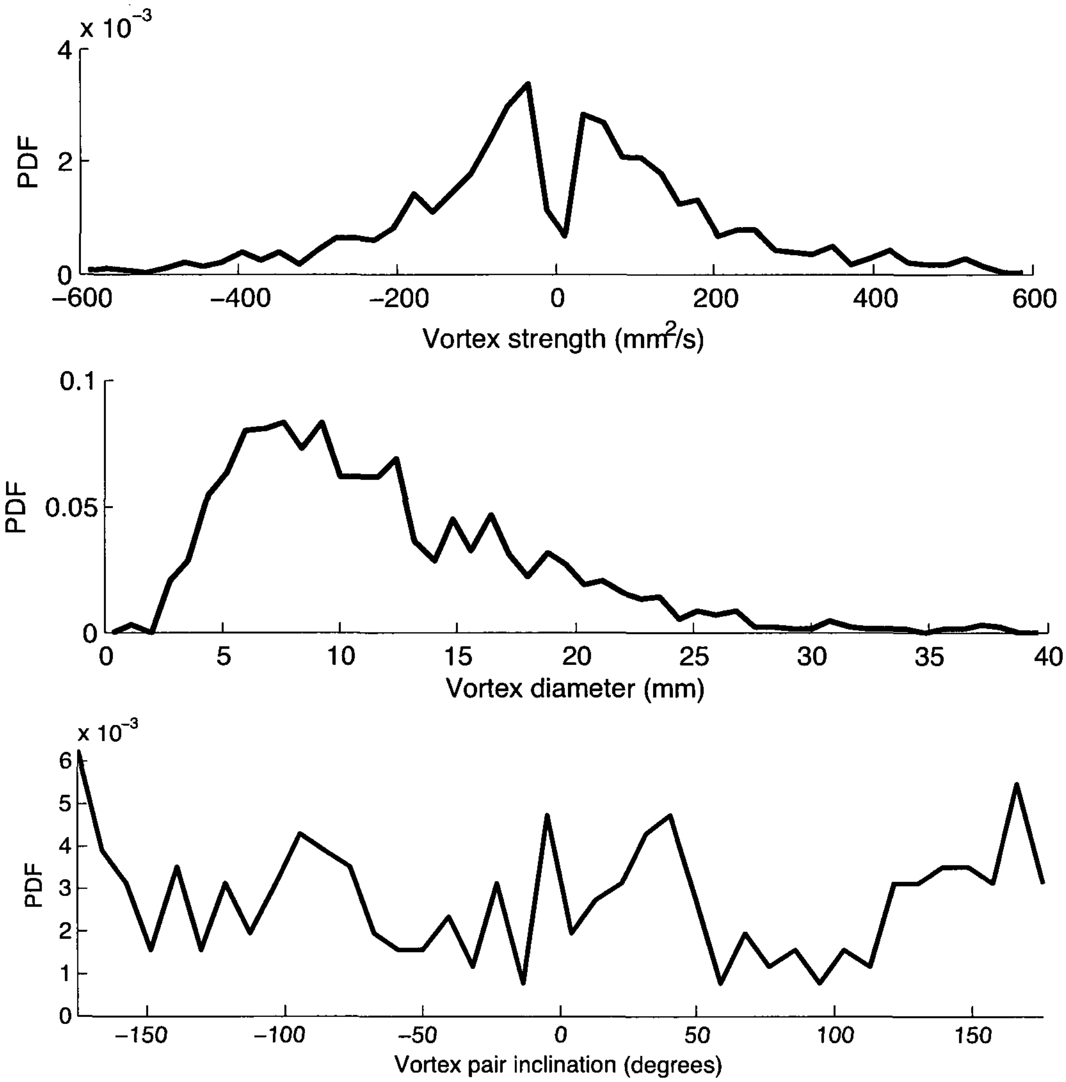

Figure 5.40: Probability density functions of the vortex strengths and diameters, and the vortex pair inclinations in the horizontal plane. Negative vortex strength corresponds to a vortex with CW rotation. Refer to Figure 4.5 for the definition of the vortex pair inclination.

5.4.4 Inclined plane measurements

PIV measurements were taken in a plane inclined by 45° with respect to the flow direction, as in the scanning dye visualisation. Some images were taken with simultaneous dye injection in order to allow comparison with results of previous dye visualisations.

Measurements in this plane measure only a component of the streamwise velocity. Because of this inclination, the mean in-plane velocity is towards the bottom of the image. This velocity component exhibits a mean uniform gradient proportional to the streamwise velocity gradient in the x_2-direction.

The recorded dye patterns are similar to those recorded by Kislich-Lemyre [23] and by the scanning dye visualisation. Mushroom-shaped ejections at a range of angles are the best identifiable structures. These are the dye patterns created by two parallel counter-rotating vortices, which induce fluid motion between them. A velocity map is presented in Figure 5.41, and the corresponding dye visualisation is shown in Figure 5.42. A large upright mushroom-shaped dye pattern is identified, coinciding with a counter-rotating pair of vortices of large strength. These images show that low speed fluid from the bottom of the image is induced upwards between the vortex pair, transporting with it both dye as well as its relatively low velocity.

Vortices identified using the PIV vortex identification algorithm did not always coincide with suitable patterns in the dye. One must keep in mind that dye patterns are not always correlated with the local velocity field. For example, dye patterns created by vortex structures could remain in the fluid even after the vortex has dissipated [18]. Moreover, the vortex identification algorithm has its limitations. All things considered, the positions, sizes, and strengths of the vortices may not be exact, but it is assessed that the statistics of these properties are sufficiently accurate to provide at least a qualitative description of the vortex field.

The statistics of the vortex properties are summarised in Table 5.3 and Figure 5.43. There are about half as many vortices detected as were in the horizontal plane, which may be partially attributed to the strong out-of-plane velocity component that increases the difficulty in finding matching vortices in adjacent time frames. There is an approximate balance of clockwise and counter-clockwise vortices. The mean

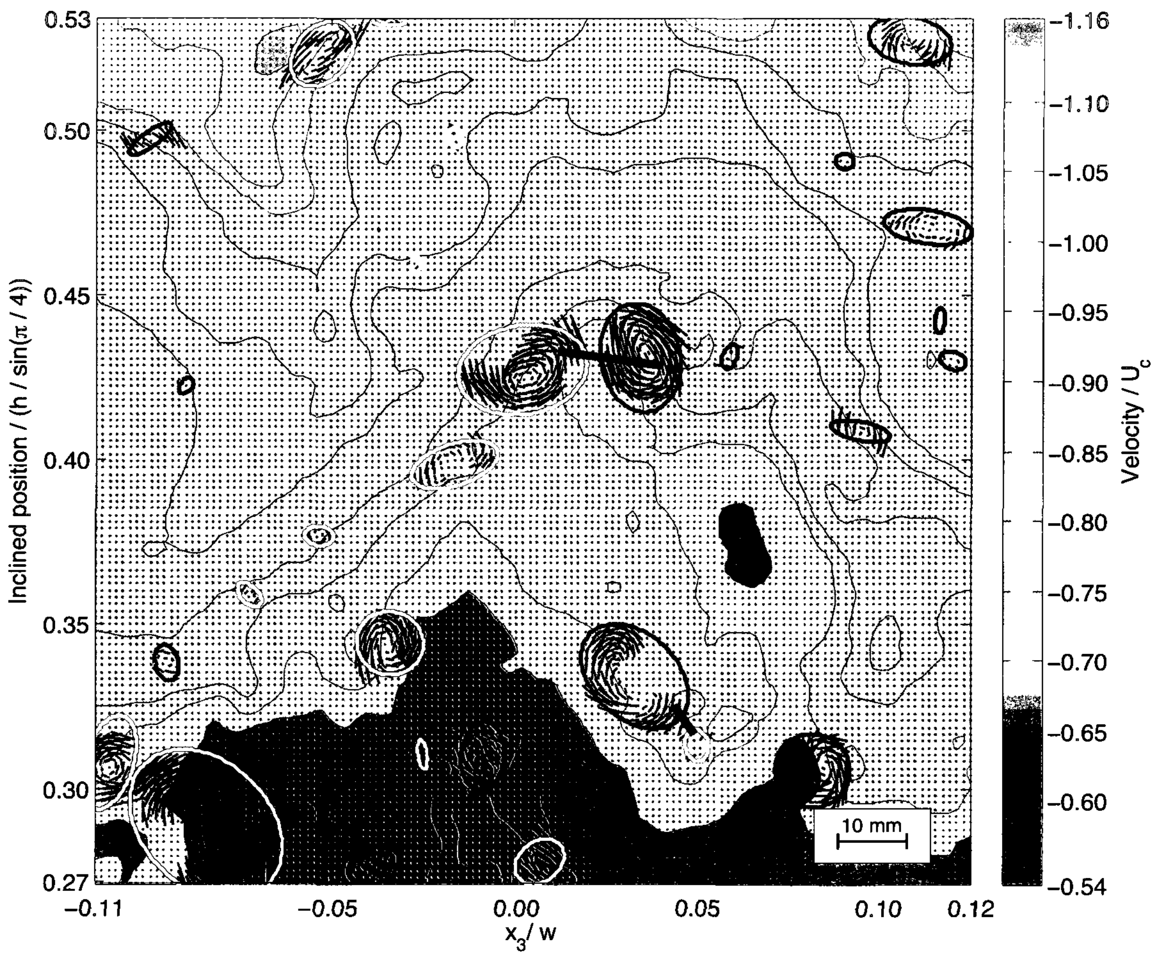

Figure 5.41: Sample velocity map in the inclined plane. Vortices are identified by the surrounding vectors relative to the vortex convection velocity and are enclosed by drawn black ellipses if turning CW and white ellipses if turning CCW. Pairs are connected by solid black lines.

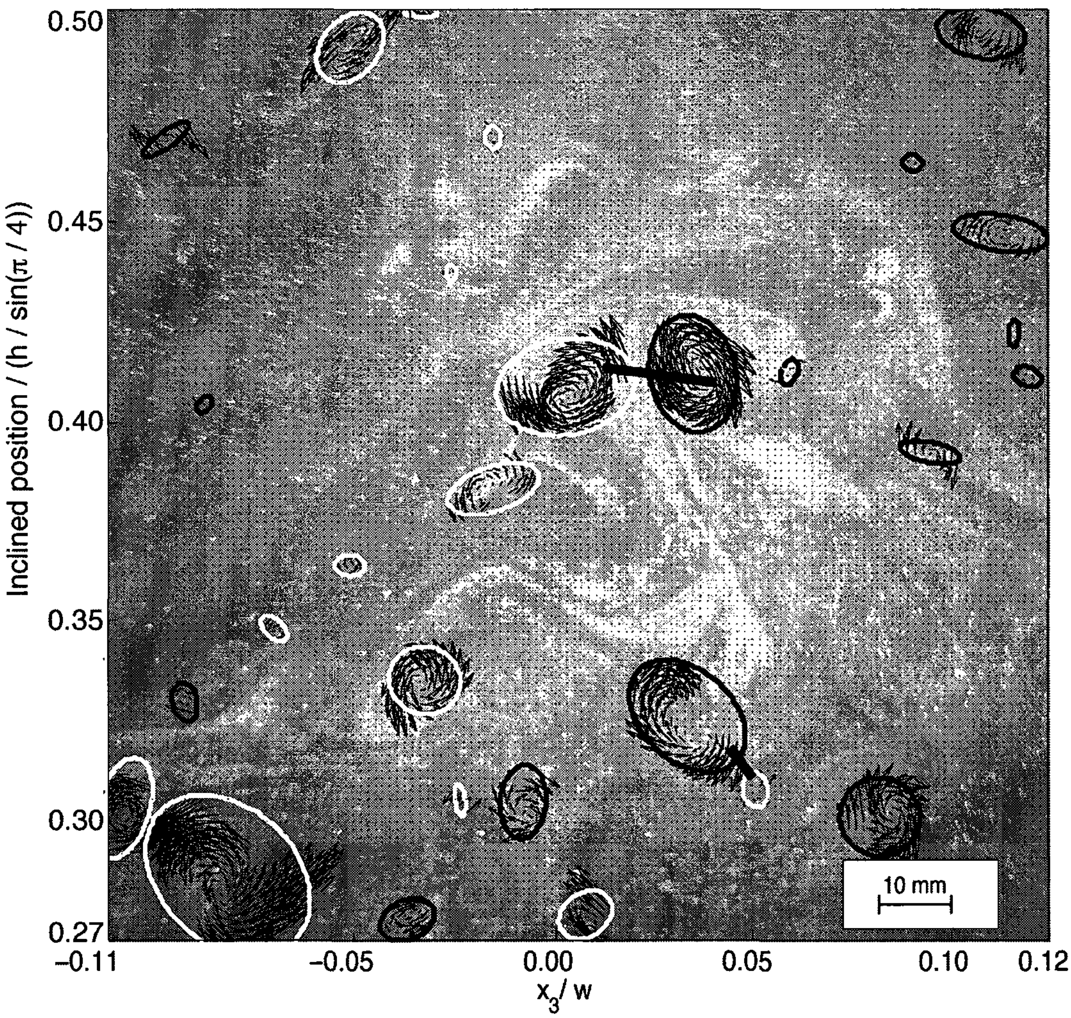

Figure 5.42: Sample dye pattern in the inclined plane. Vortices are identified by the surrounding vectors relative to the vortex convection velocity and are enclosed by drawn black ellipses if turning CW and white ellipses if turning CCW. Pairs are connected by solid black lines.

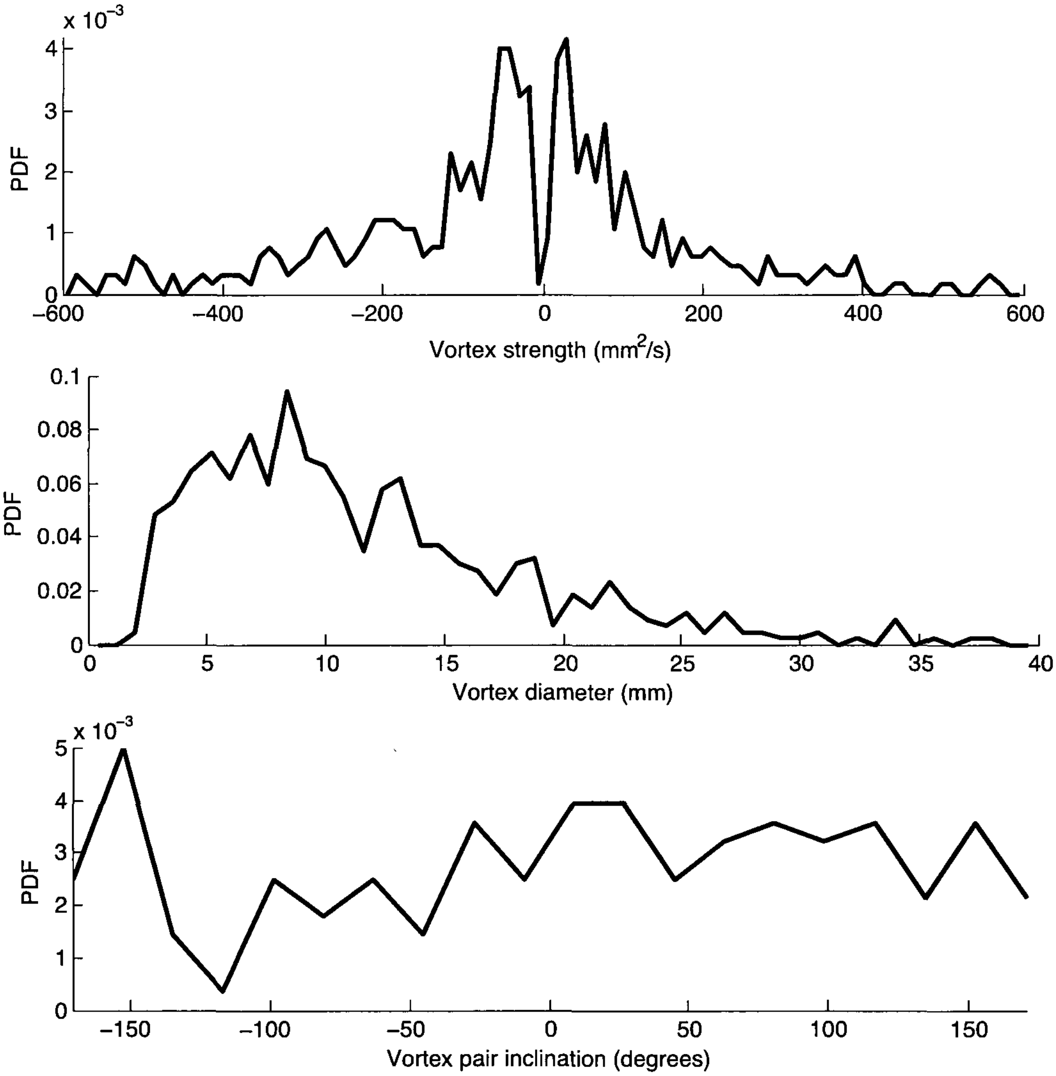

Figure 5.43: Probability density functions of the vortex strengths and diameters, and the vortex pair inclinations in the inclined plane. Negative vortex strength corresponds to a vortex with CW rotation. Refer to Figure 4.5 for the definition of the vortex pair inclination.

strength and size of the vortices were slightly larger than those found in the horizontal plane.

The pair-matching algorithm identified fewer pairs than in the horizontal configuration, with an average of four pairs per frame. The probability density function of the pair inclinations, presented in Figure 5.43, shows a roughly even distribution of pair angles, with a peak near $-160\,°$.

5.4.5 Tracking vortices in the inclined plane

Structures were difficult to track as they were swiftly convected through the inclined plane. Typically vortices were only coherent for two to three frames before they were broken up or had completed passed by the camera's field of view. A few images were collected in the reduced speed flow ($U_c = 0.12$m/s), in which vortices were easier to identify and track than at the higher speed. Vortices in these recordings could be tracked for up to twenty frames. An example of such a frame sequence in which a vortex pair is clearly being convected though the plane is presented in Figures 5.44 to 5.47. This frame sequence shows that some of the vortices broke up and were reorganized, however their vorticity was still traceable and their sense of rotation was maintained. The shapes of the velocity contours around the vortex pair were also relatively stable, exhibiting the same region of low-speed flow being induced upwards between the vortex pair as in the stationary example of Figures 5.41 and 5.42.

Using Taylor's frozen flow hypothesis and neglecting any change the structures undergo in the time it takes them to completely pass through the frame, one may reconstruct the structures in 3D space. The images were processed in a similar way to the scanning visualisations as described in Section 4.3, however, the planes of consecutive images were separated by a uniform distance, which was equal to the ratio of the mean convection velocity through the plane and the sampling rate. Because each frame only extended 70 mm in depth, the change in velocity from the top to the bottom of the frame was small and one may neglect transverse straining. The reconstruction of this vortex pair is presented in Figure 5.48. This vortex pair consisted of two counter-rotating vortices that were nearly parallel to each other and may be confidently regarded as the legs of a hairpin vortex. Unfortunately, the PIV system was unable to capture the head of the hairpin because the vorticity vector at the head was parallel to the recording plane. This vortex pair was approximately 90 mm wide and 330 mm long.

Another sequence of images at the lower flow rate (U_c = 0.12m/s) captured an inverted vortex pair. The frame sequence and 3D reconstruction of this vortex pair are shown in Figures 5.49 to 5.52 and 5.53. The vortices in this frame sequence also exhibited some splitting and reforming, but the downward burst of high speed fluid revealed by the velocity contours was stable until the final breakup of the pair. Near the middle of the frame sequence, a second vortex pair appeared, which may be another structure being formed and split off from the original hairpin, or a nearby structure that was aligned with the larger hairpin. The inverted structure was approximately 70 mm wide and 350 mm long, namely very close in size to the upright vortex pair described previously. Other than the direction of rotation, this vortex pair was quite similar to the upright pair.

These two examples represented the longest observed vortices in the lower speed flow. The same two frame sequences showed many more vortices, which, however, were not as long in the streamwise direction, typically only about 150 mm. These vortices were more difficult to track with certainty, as their vorticity and local velocity contours were less stable.

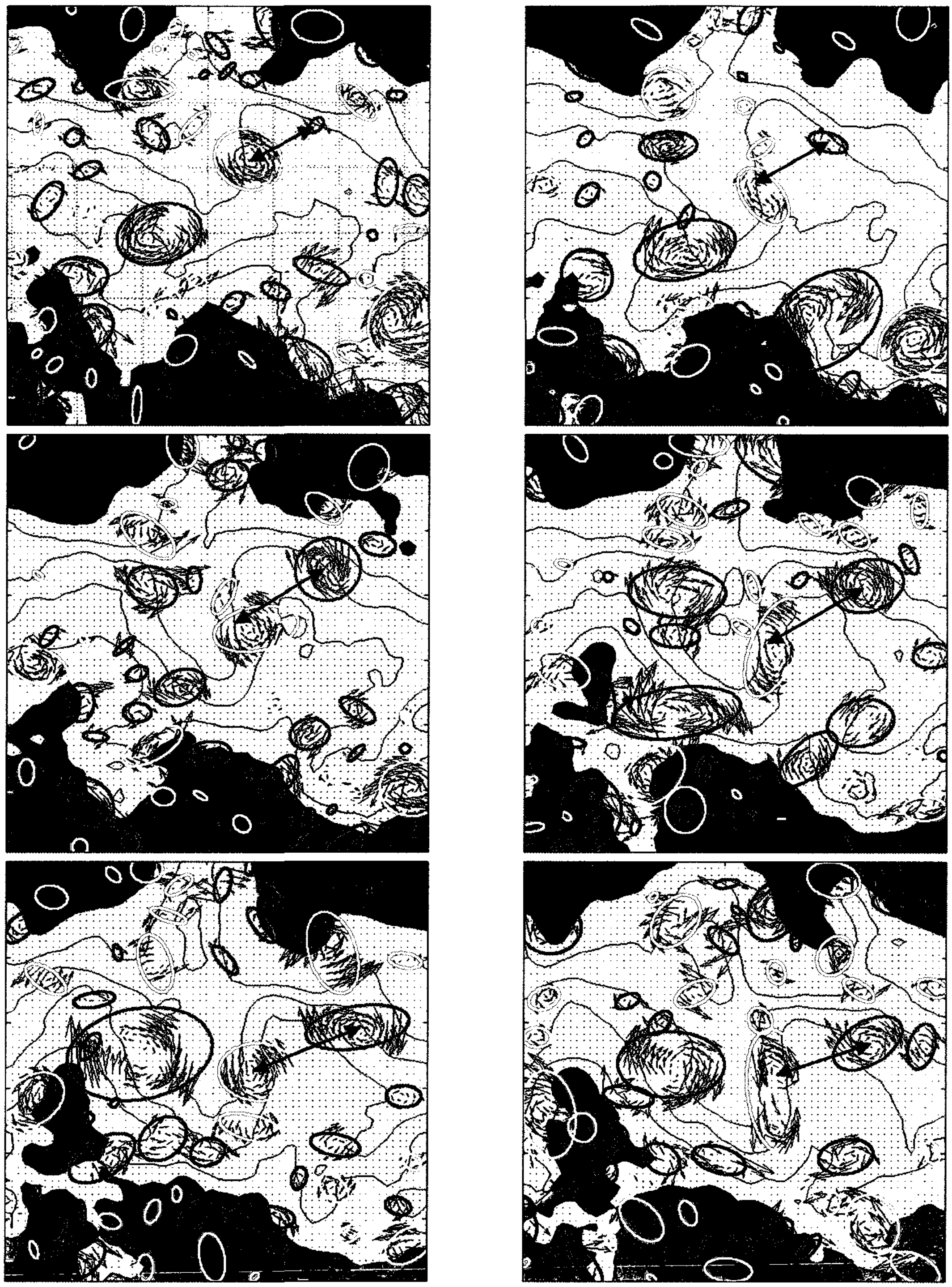

Figure 5.44: Frame sequence 1/4 of a manually tracked vortex pair in a reduced flow rate inclined recording.

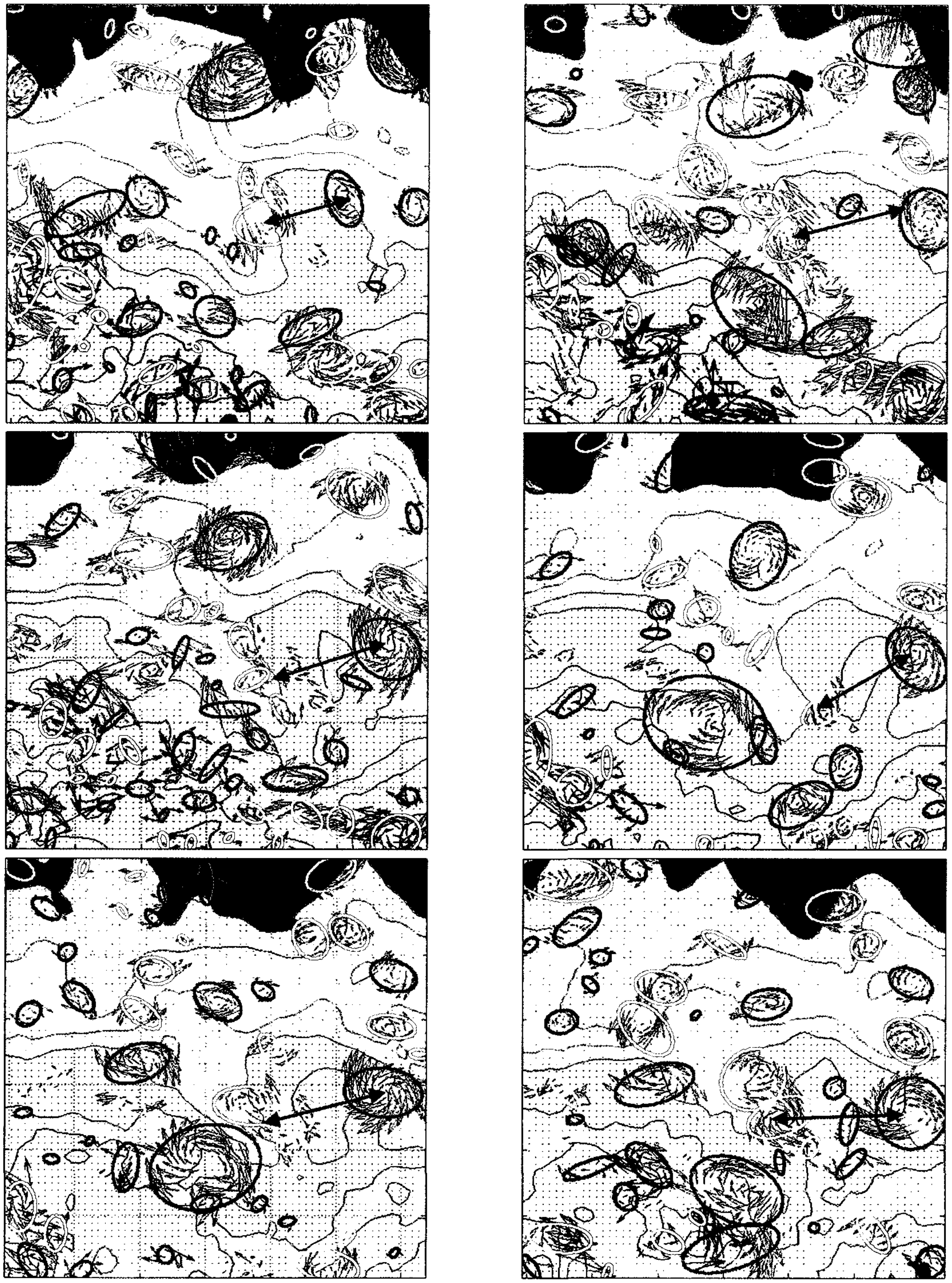

Figure 5.45: Frame sequence 2/4 of a manually tracked vortex pair in a reduced flow rate inclined recording.

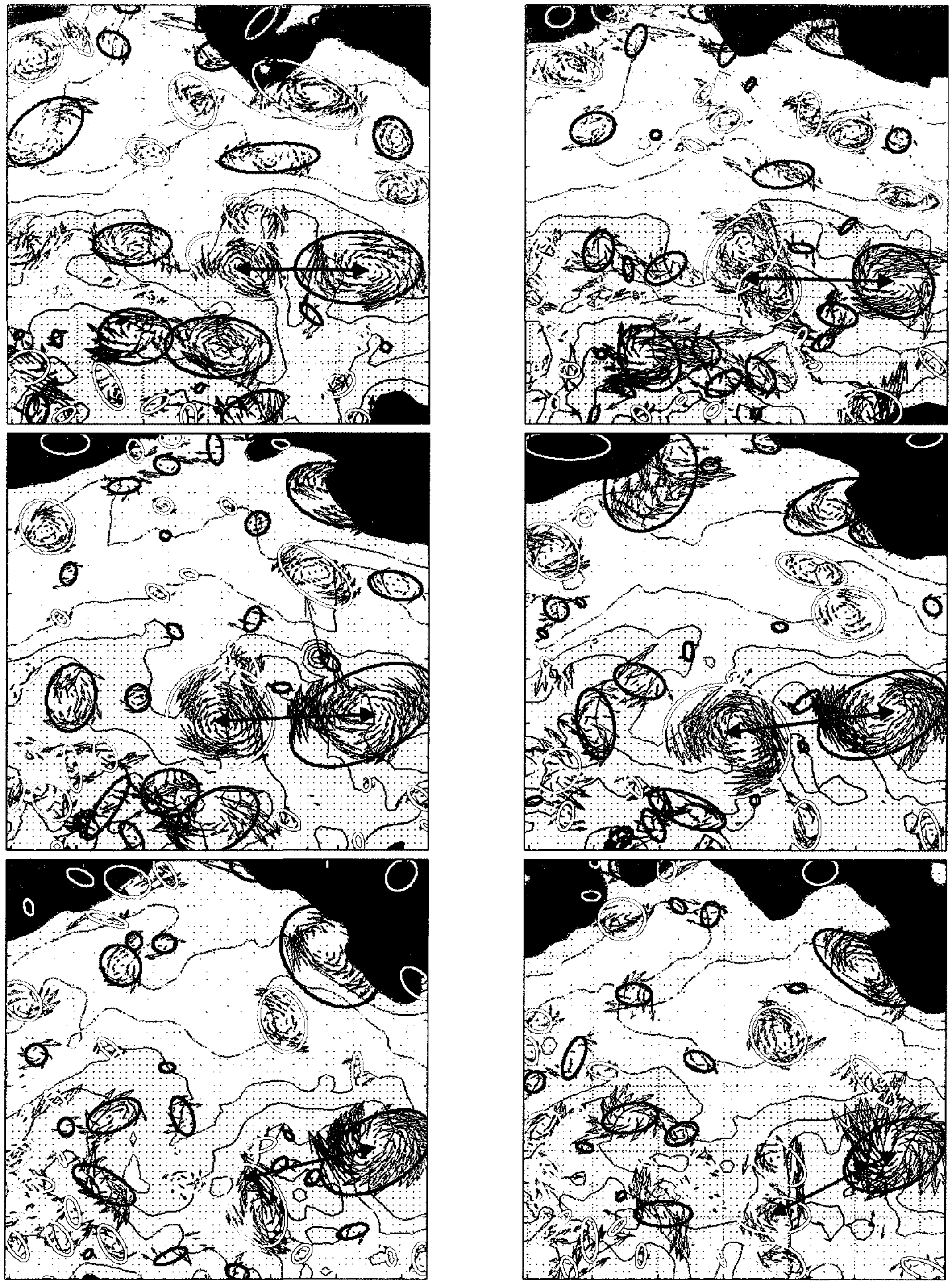

Figure 5.46: Frame sequence 3/4 of a manually tracked vortex pair in a reduced flow rate inclined recording.

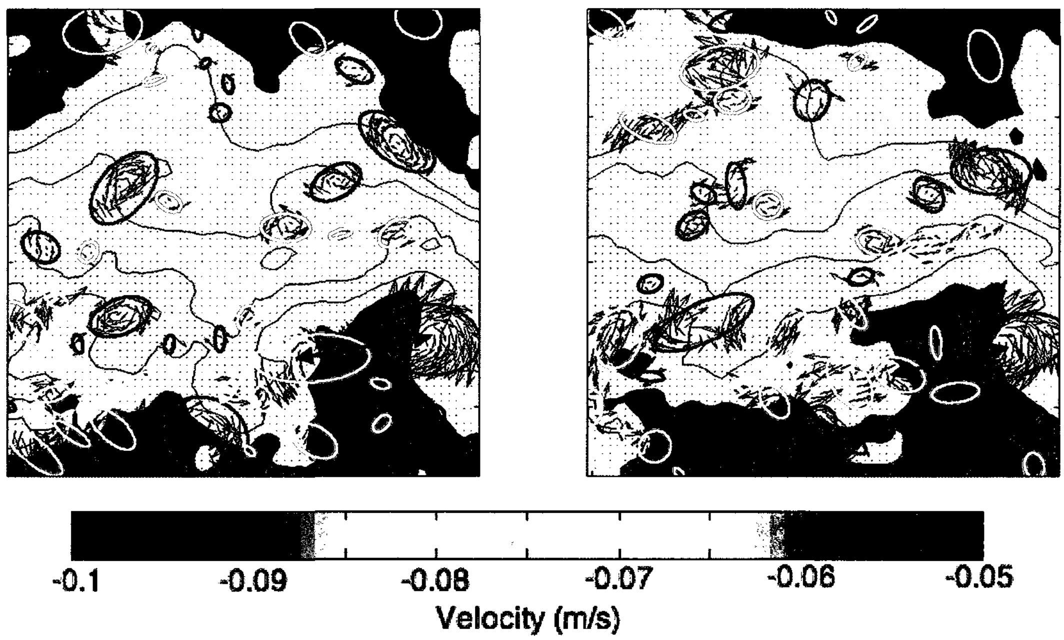

Figure 5.47: Frame sequence 4/4 of a manually tracked vortex pair in a reduced flow rate inclined recording. Image scale is the same as for previous inclined measurements in Figures 5.41 and 5.42. Vortices are identified by the surrounding vectors relative to the vortex convection velocity and are enclosed by black ellipses if turning CW and white ellipses if turning CCW. The manually tracked vortex pair is identified by the dark arrow.

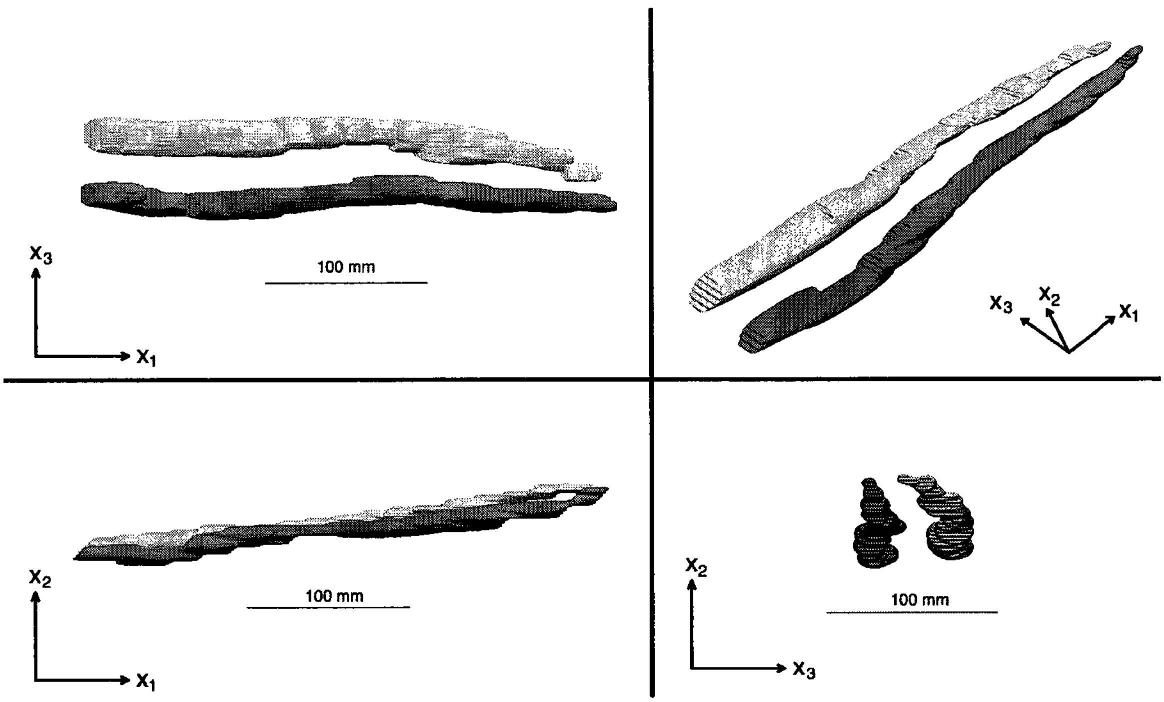

Figure 5.48: A 3D reconstruction of the vortex pair tracked through the inclined plane in reduced speed flow from Figures 5.44 - 5.47. This pair is counter-rotating such as to induce an upward flow between themselves.

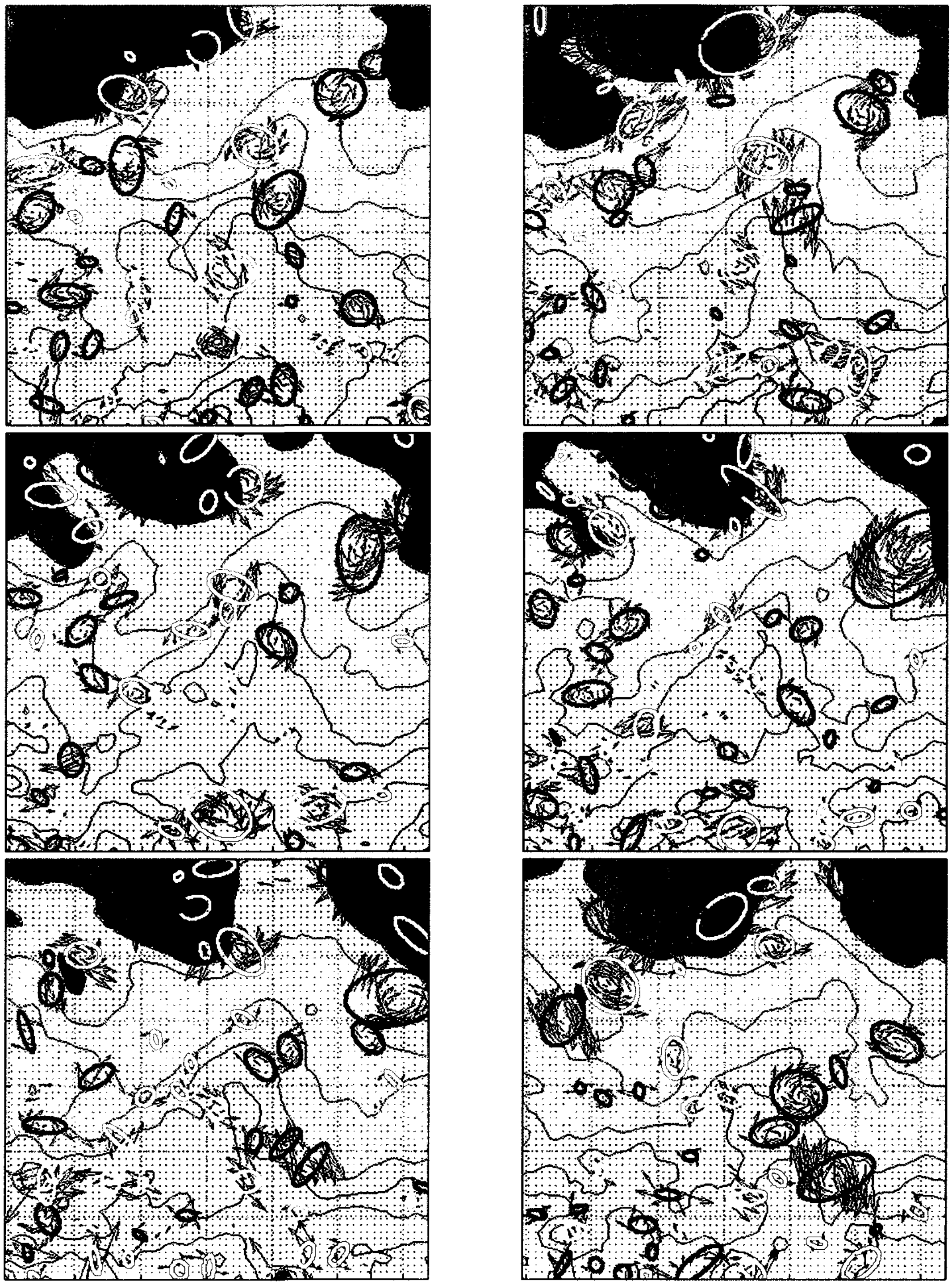

Figure 5.49: Frame sequence 1/4 of a manually tracked vortex pair in a reduced flow rate inclined recording.

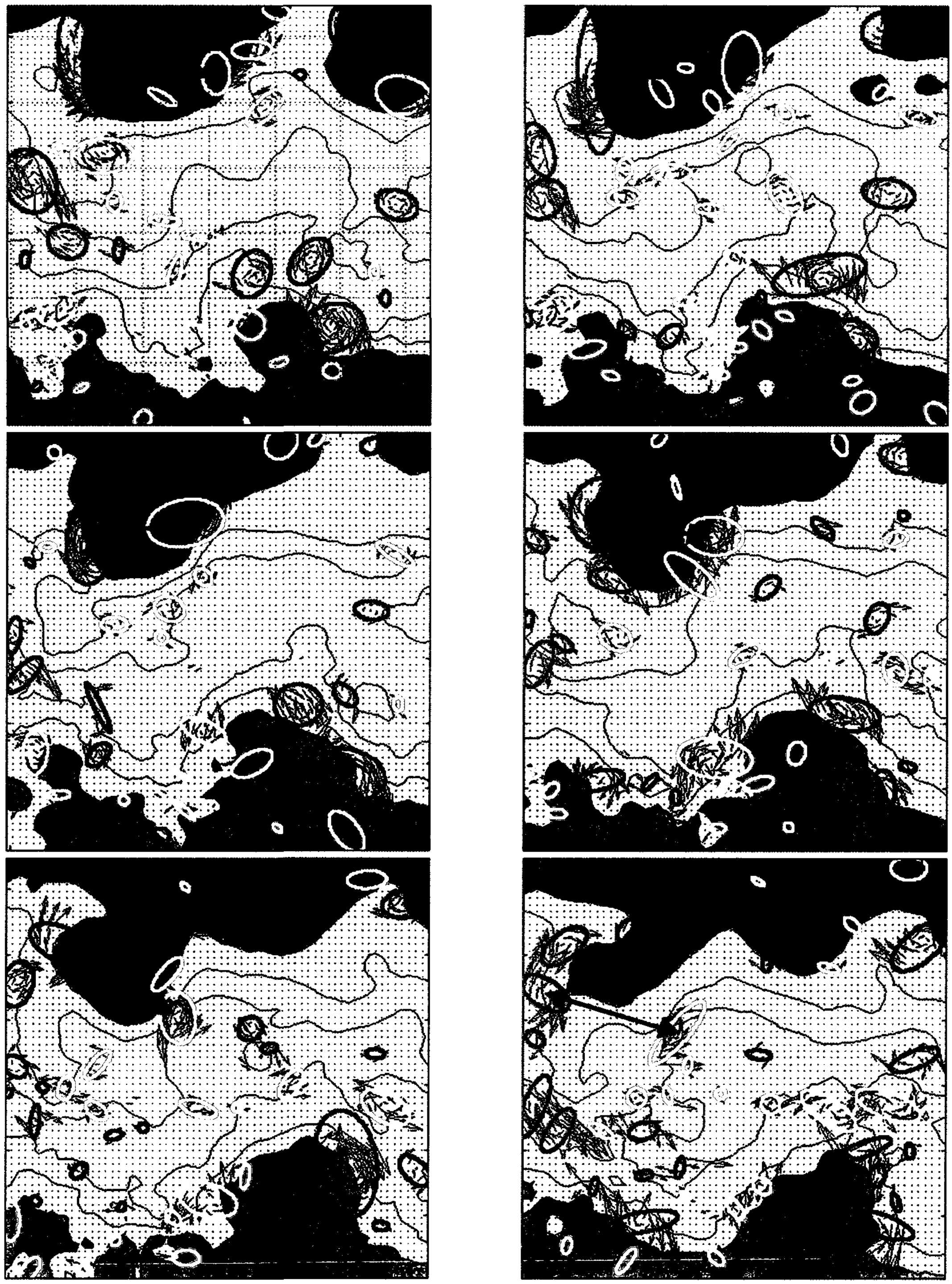

Figure 5.50: Frame sequence 2/4 of a manually tracked vortex pair in a reduced flow rate inclined recording.

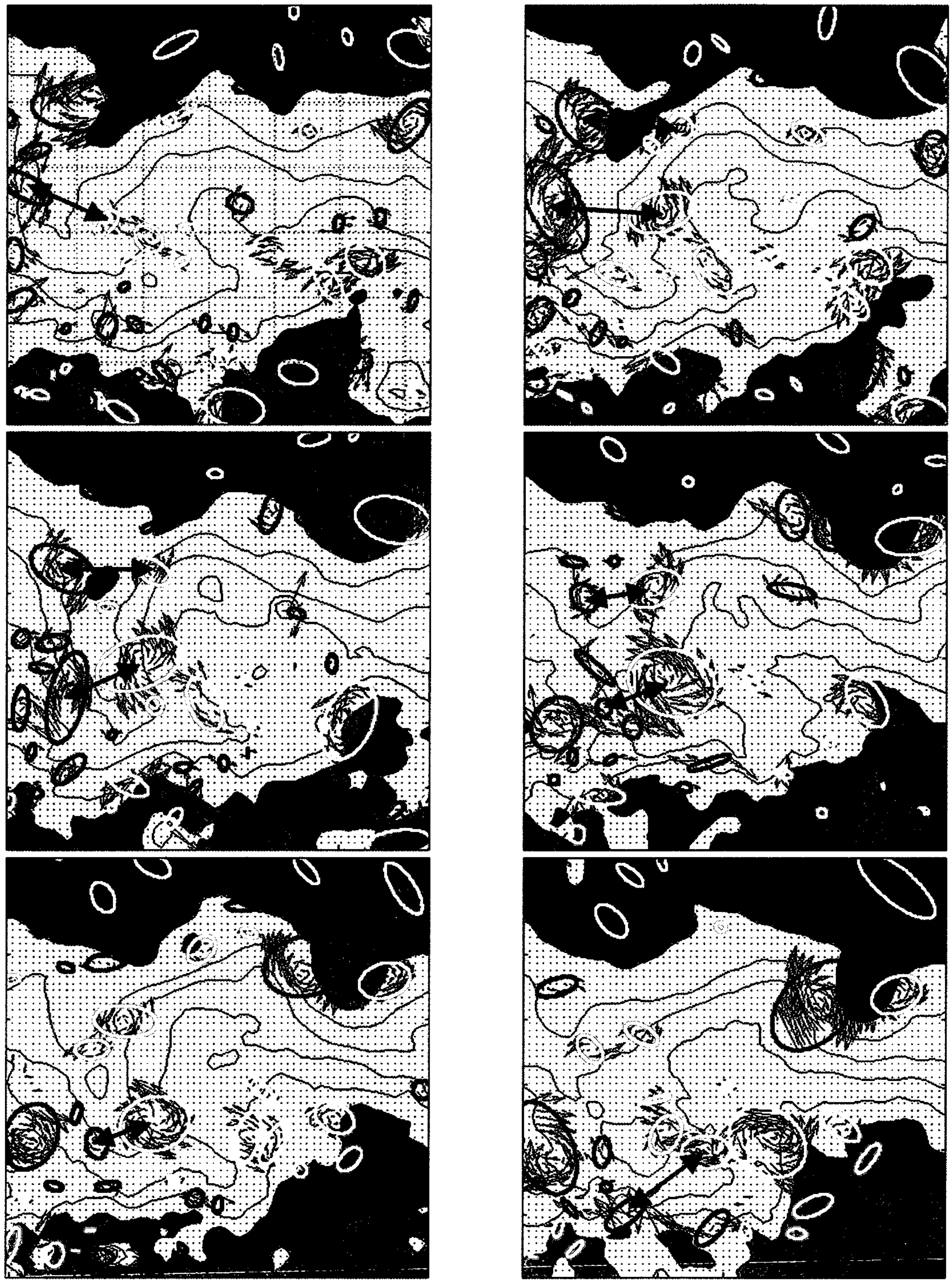

Figure 5.51: Frame sequence 3/4 of a manually tracked vortex pair in a reduced flow rate inclined recording.

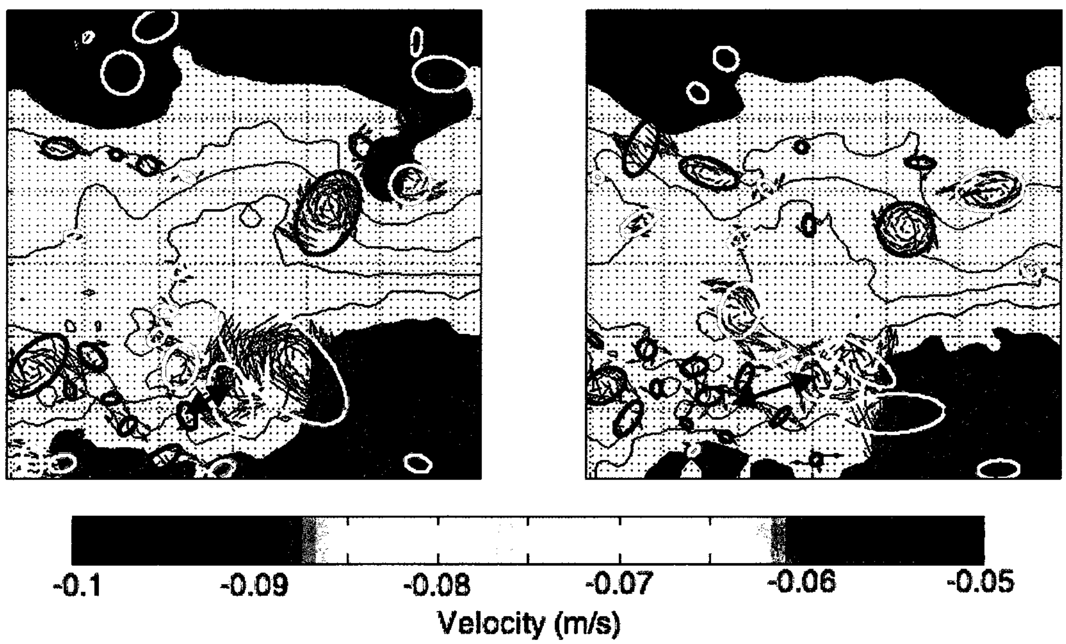

Figure 5.52: Frame sequence 4/4 of a manually tracked vortex pair in a reduced flow rate inclined recording. Image scale is the same as for previous inclined measurements in Figures 5.41 and 5.42. Vortices are identified by the surrounding vectors relative to the vortex convection velocity and are enclosed by black ellipses if turning CW and white ellipses if turning CCW. The manually tracked vortex pair is identified by the dark arrow.

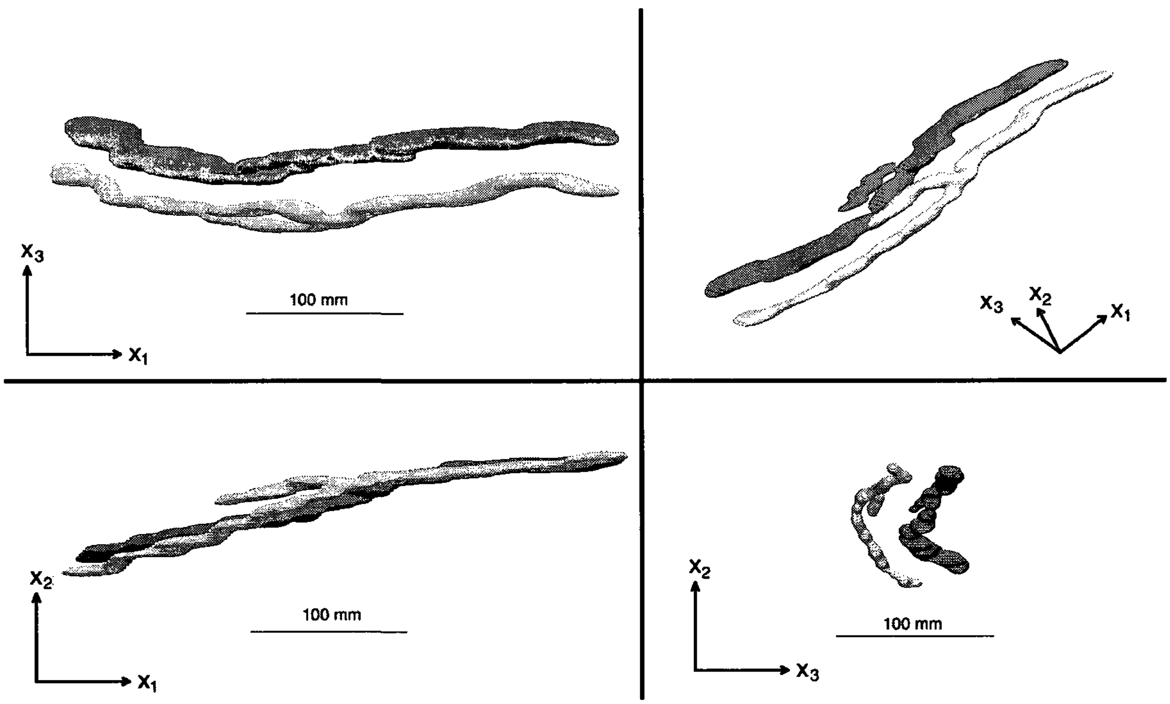

Figure 5.53: A 3D reconstruction of the vortex pair tracked through the inclined plane in reduced speed flow from Figures 5.49 - 5.52. This pair is counter-rotating such as to induce a downwards flow between themselves.

Chapter 6

Discussion

This chapter evaluates and compares the results collected from the four experiments. First of all, the discussions of the flow visualisation and PIV results are expanded on, comparing the measurements in the multiple planes and interpreting the structures captured in the 2D fields. Some discussion is included regarding the observed dissimilarities between flows at high and low speeds. The length scales from the PIV are then compared to those collected in the three other experiments. Finally, the characteristics of these structures are compared to those of the hairpin vortices found in the turbulent boundary layer.

6.1 Evidence of coherent structures

6.1.1 Evidence in flow visualisation results

The main conclusions from the scanning dye visualisations were that mushroom-shaped vortices were common dye patterns in the flow, and that they indicated the presence of elongated, slightly-inclined vortex tubes. These mushroom-shaped vortices were interpreted as the legs of horseshoe vortices, following the association between these dye patterns and hairpin or horseshoe vortices that was established in turbulent boundary layer studies [16]. The names hairpin and horseshoe refer to the same type of coherent structures; the difference between them is the relative elongation of the structures [16]. A comparison between the mushroom-shaped dye patterns in USF to those in the turbulent boundary layer is presented in Figure 6.1. The main difference between the patterns of the two flows is the much wider range of inclinations observed in the USF. Simultaneous PIV and dye visualisation in the inclined plane confirmed the association between the mushroom-shaped dye pattern and the presence of two counter-rotating quasi-streamwise coherent vortices.

Figure 6.1: Comparison of the mushroom-shaped dye patterns in the turbulent boundary layer (left, reproduced from [16]) to those in USF (right, ref. Fig. 5.13).

Though the heads of the vortices were unclear in the dye patterns, they were clearly observed in the hydrogen bubble visualisation images taken with the use of a horizontal cathode wire. In several examples, a piece-wise outline of a horseshoe vortex was identified from the combination of bubbles from several timelines in the flow. Though the patterns corresponding to the elongated legs often were disjointed, the heads were clearly composed of bubbles of a single timeline that had reorganized into an arch. These arches were usually observed downstream of the elongated legs.

In view of the fact that both the heads and the legs of horseshoe vortices were clearly observed in the flow visualisations, albeit not always together, the hypothesis that this type of vortex is the predominant large-scale structure of USF is supported. This hypothesis is also supported by the literature, which has previously speculated towards this conclusion [35] [26] and often points out the likeness between USF and turbulent boundary layer flow [8] [26].

6.1.2 Evidence in PIV results

Insofar as possible with 2D planar measurements, the PIV results also support the hypothesis that hairpin or horseshoe vortices occur in abundance in USF. The measurements in the three planes captured cross-sections of the horseshoe vortices and the associated hairpin signatures in the velocity maps.

The measurements in the vertical plane were comparable to corresponding measurements collected in the turbulent boundary layer, which had been shown to contain hairpin vortices. Representative velocity maps in the two flows are presented for comparison in Figure 6.2. Large clockwise vortices were observed in both flows, located along the shear layers that separate zones of relatively uniform velocity. In turbulent boundary layer studies, these vortices were interpreted as the heads of hairpin or horseshoe vortices. The streamwise alignment of multiple heads was indicative of the size and number of vortices which formed large-scale packets. Both flows also contained smaller vortices scattered over the measurement area, which did not seem to be the heads of horseshoe or hairpin vortices.

PIV measurements of USF in the inclined plane captured the cross-sections of the legs of horseshoe vortices. This was best illustrated by the simultaneous PIV and dye visualisation presented in Figures 5.41 and 5.42, which showed an upright mushroom-shaped dye pattern coincident with two counter-rotating vortices. Though the streamwise length of the two vortices could not be measured with the stationary PIV because of the insufficient temporal resolution, it was inferred to be sufficiently long such that the vortex pair had enough influence on the flow to induce such a large upwards burst, as identified by the dye pattern and the velocity map. These large bursts were fairly common in the inclined plane. These observations of legs in the inclined plane were further supported by similar observations in the horizontal plane.

6.1.3 The quintessential vortex shape

Following previous discussion, it is now possible to describe the three-dimensional shape and size of the typical horseshoe vortices in USF (refer to Figure 6.3). From the average length of the structures observed by the scanning dye visualisation, the length of the legs is estimated to be approximately 70 mm, inclined upwards by approximately 45° from the direction of the flow. This corresponds to a vertical height of about 50 mm, which compares with the average separation distance between shear layers, measured with PIV in the vertical plane. The legs are separated by about 25 mm, as estimated by the dye visualisation, bubble patterns, and PIV measurements in the horizontal and inclined planes. The shape is more representative of a horseshoe than a hairpin, due to its relatively low ratio of the length to the width.

These horseshoe vortices were observed to twist and turn in the flow, appearing

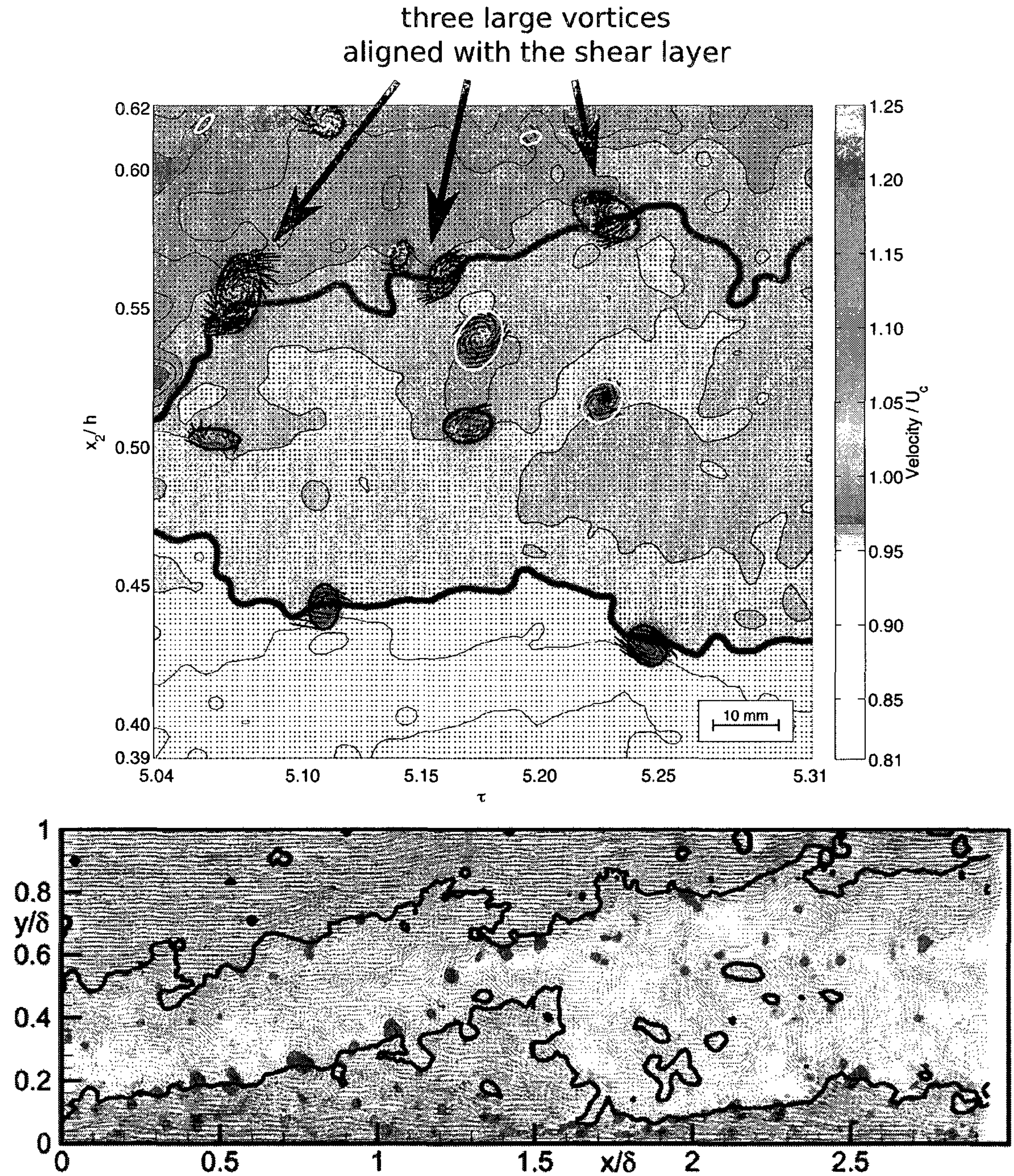

Figure 6.2: Comparison of PIV measurements in the vertical plane in USF (top, ref. Fig. 5.31) to measurements in a wall-normal plane in the turbulent boundary layer (bottom, ref. Fig. 2.4 [1]). Zones of relatively uniform velocity are boldly outlined, and vortices identified by peaks in swirling strength are shaded.

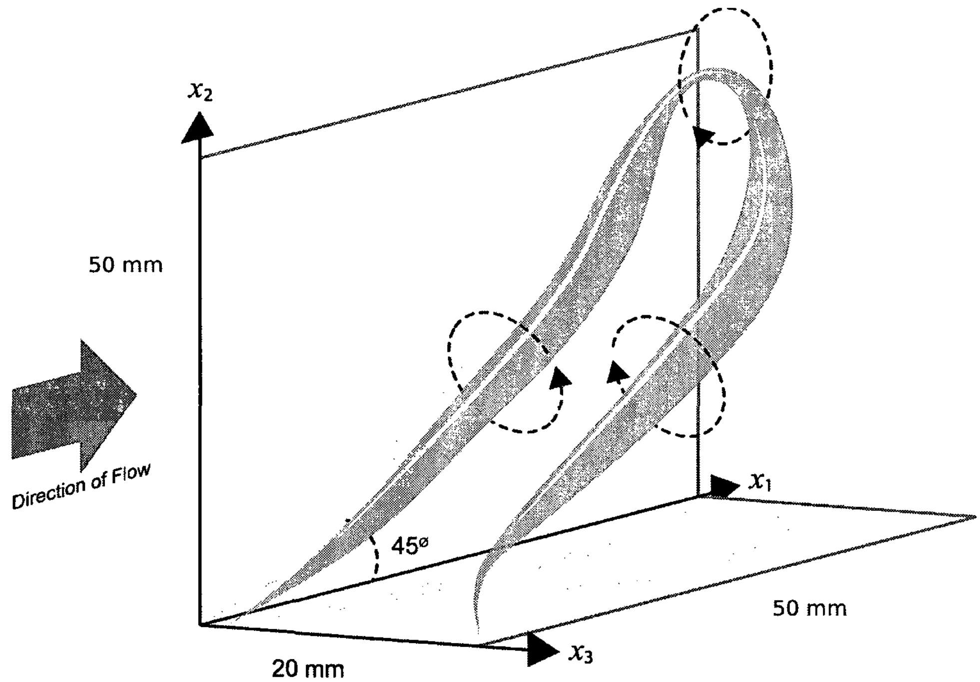

Figure 6.3: Sketch of the quintessential upright hairpin vortex of USF (illustration created by C. D. McKnight-MacNeil, 2009).

at a large range of inclinations. They were not limited to the upright configuration sketched in Figure 6.3, which is typical of the hairpin structures of the turbulent boundary layer. However, regardless of orientation, these structures were often observed to be aligned in the streamwise direction, as demonstrated by the results of the bubble visualisations and the PIV.

6.2 The statistical distributions of the vortex properties

The properties of the vortices identified using PIV in the three planes of the flow also agree with the presence of horseshoe vortices.

In the vertical plane, there was a ratio of 0.76 between the concentrations of clockwise and counter-clockwise vortices. The clockwise vortices also tended to have greater strengths than the counter-clockwise vortices. The large clockwise vortices could correspond to the cross-sections of the heads of horseshoe vortices, however, not all vortices in the vertical plane were vortex heads. Some of the small-scale vortices in this plane are likely to have been generated by the mean shear and had not yet

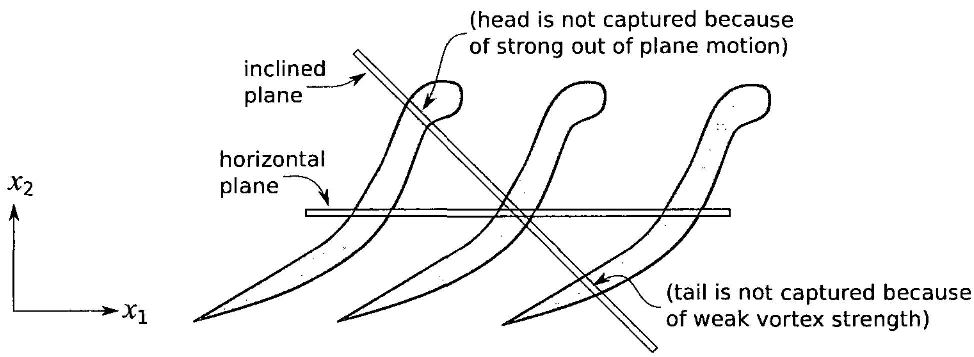

Figure 6.4: Sketch of the horizontal and inclined planes in relation to a group of streamwise-aligned horseshoe vortices, illustrating a possible explanation for the reduced average number of vortices in the inclined plane.

developed into large-scale structures. The contributions of this population of small-scale vortices make the mean size and mean strength of the vortices in the vertical plane small compared to those in the other planes.

The large-scale vortices in the horizontal and inclined planes were interpreted as the cross-sections of the legs of horseshoe vortices. The presence of counter-rotating vortex pairs was supported by the almost even population of clockwise and counter-clockwise vortices. The vortices in the inclined plane were slightly stronger on average than those found in the horizontal plane, which is consistent with the fact that the legs were inclined upwards, roughly orthogonal to the inclined plane. The greater average number of vortices in the horizontal plane compared to that in the inclined plane may also be related to the inclination of the vortex structures as well as the fact that they tended to be aligned in the streamwise direction, as illustrated in Figure 6.4. While both planes may have intersected multiple horseshoe structures, the vortex pairs identified in the inclined plane would have had varying strengths and may not have met the threshold for identification, unlike those that would have been identified in the horizontal plane.

The inclinations of vortex pairs in the horizontal and inclined planes were widely distributed. Sharp peaks in the probability density functions occurred at 180° in both configurations, coinciding with the orientation of the upright horseshoe vortex as illustrated previously in Figure 6.3. A smaller peak occurred in the range from 0° to 45°, corresponding to inverted hairpins whose legs rotated in directions opposite to those of the upright vortex pair. The evenness of the distributions, however, indicated that the vortex pairs were not limited to these two configurations and appeared at all inclinations.

6.3 Zones of roughly uniform velocity

The instantaneous velocity maps suggest the presence of zones of roughly uniform velocity, which in the turbulent boundary layer are associated with hairpin vortex packets (refer to Figure 6.5) [1]. These zones of roughly uniform velocity were observed in the proximity of large vortices in all three measurement planes, though they took different forms in each plane. These zones were bordered by shear layers along which vortices were identified. These locally uniform zones influenced the instantaneous velocity profiles, which underwent relatively large step changes, in contrast to the near-linearity of the time-averaged velocity profile.

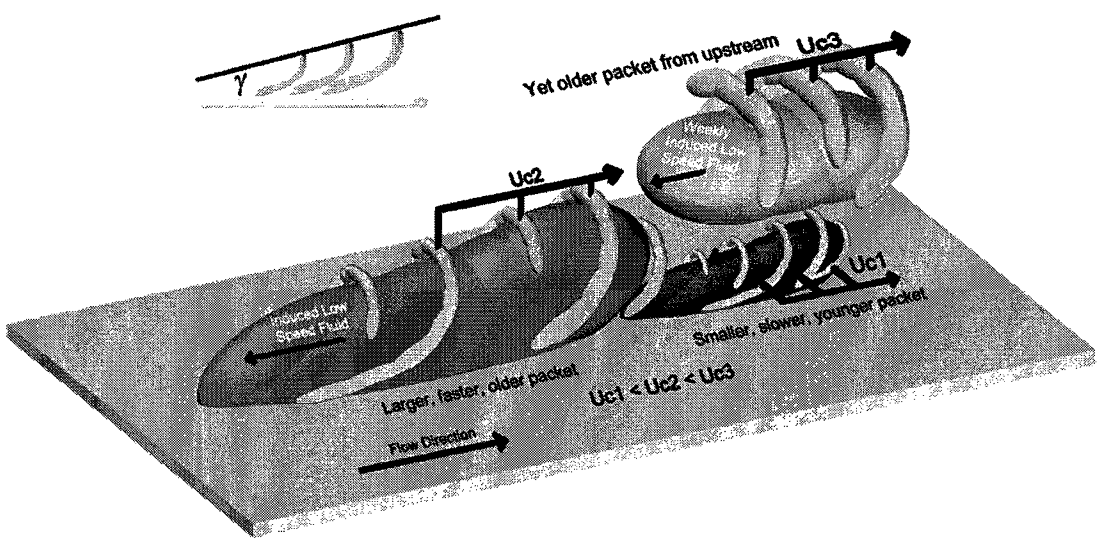

Figure 6.5: Illustration of the zones of roughly uniform momentum associated with hairpin packets in the turbulent boundary layer (ref. Fig. 2.5 [1]).

In the vertical plane, the zones of locally uniform velocity were sandwiched between upper and lower shear layers and were typically about 50 mm tall, as illustrated in Figure 6.6 and previously in Figure 6.2. They had a streamwise length that was

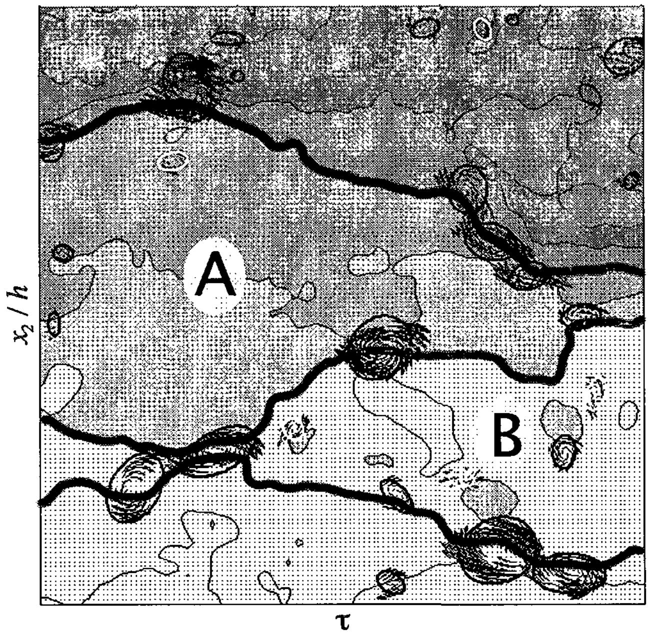

Figure 6.6: PIV measurements in the horizontal plane (ref. Fig. 5.36). Two zones of relatively uniform velocity are outlined by thick lines.

longer than the width of the field of view, which was about 100 mm, meaning that these zones were much longer than they were tall. Videos of the flow convecting past the stationary vertical plane showed that the shear layers separating these zones moved up and down in a saw-tooth or ramp-like pattern.

The instantaneous velocity maps in the horizontal plane also identified similar zones, which had average velocities greater or lower than the mean velocity in the plane. These zones had a typical spanwise spacing of only about 25 mm, compared to a streamwise length of about 100 mm, making them look like streaks. Examples of these zones are illustrated in Figure 6.7. These zones were bordered on either side by relatively steep spanwise gradients in the streamwise velocity, along which several vortices were located. The vortices were often paired to counter-rotating vortices located on the other side of the zones.

This pattern was also observed in the inclined plane, even though the plane did not include the streamwise direction. An example of one of these zones is illustrated in Figure 6.8. The pattens in the inclined plane were similar to those in the vertical plane in the sense that the mean velocity changed linearly from top to bottom. The inclined

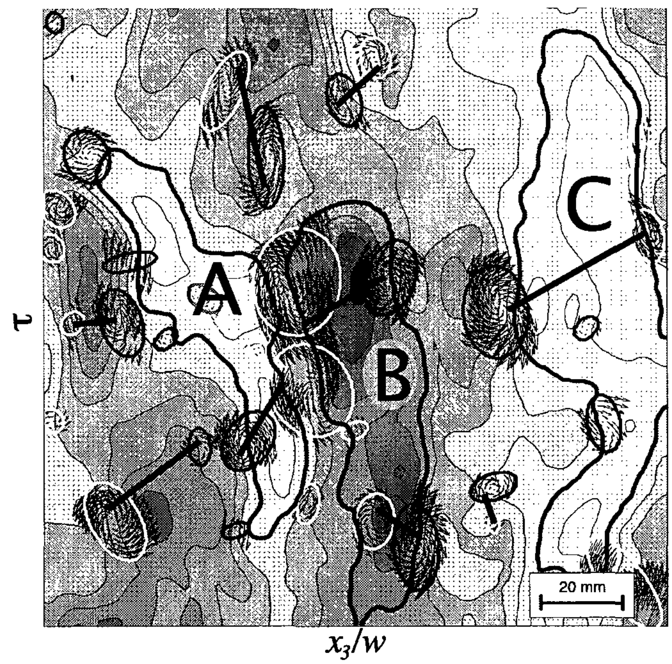

Figure 6.7: PIV measurements in the horizontal plane (ref. Fig. 5.39). Three streak-like zones of relatively uniform velocity are outlined by thick lines.

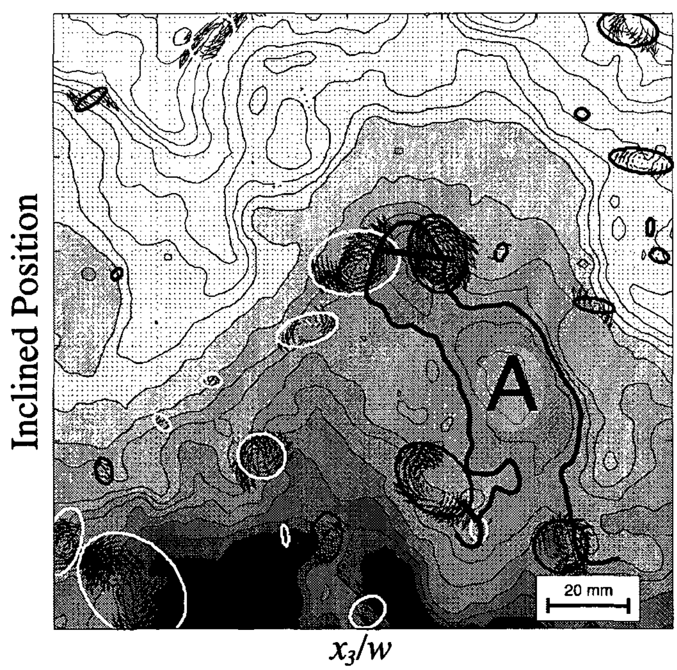

Figure 6.8: PIV measurements in the inclined plane (ref. Fig. 5.41). The large vortex pair induces an upwards burst which is interpreted as the cross-section of a zone of relatively uniform velocity and is outlined by a thick line.

plane maps also exhibited ramping shear interfaces, however these were deeper and narrower than those in the vertical plane. The zones within each saw-tooth were about 30-40 mm wide and 40-50 mm tall, consistent with the vertical and spanwise dimensions measured in the other two planes. Some vertical and horizontal wandering of the uniform pocket was apparent in the inclined plane, suggesting that, like the vortex filaments, these pockets can twist and turn in space and do not have to be perfectly aligned in the streamwise direction.

These zones of uniform velocity are comparable to those zones present in the turbulent boundary layer study by Adrian (2007) [1], and are a sign characteristic of the presence of hairpin vortices. The low-speed pockets are representative of the induced flow between several quasi-streamwise aligned upright hairpin vortices. The current zones of uniform velocity were about twice as tall as they were wide, suggesting a somewhat elongated shape to the corresponding hairpins. The fairly long streamwise length of the uniform pockets was formed by the streamwise alignment of two or more hairpin structures. This configuration is illustrated in Figure 6.9, which displays a zone of typical proportions with several fitted hairpin vortices in a configuration that would result in a low-speed pocket of fluid.

6.4 Dissimilarities in the lower speed flow

Both the hydrogen bubble experiments and the PIV measurements explored the structures that occurred using a reduced flow rate. In both cases, the motivation behind using a reduced flow rate was the opportunity to observe and capture the larger, clearer, and more exaggerated structures that resulted in the flow with reduced turbulence and shear.

In the hydrogen bubble visualisations, the bubble timelines did not mix as strongly in the slower flow. This facilitated the photography of bubble patterns as they were not obscured by the turbulent mixing surrounding them. The bubble timelines remained intact for longer distances and underwent twisting and stretching before completely diffusing. Even though arch-type structures were observed in the full-speed flow, they were often too small, fast, and obscured by other bubbles to permit a good image of them. The image in the reduced speed flow therefore offered a representative

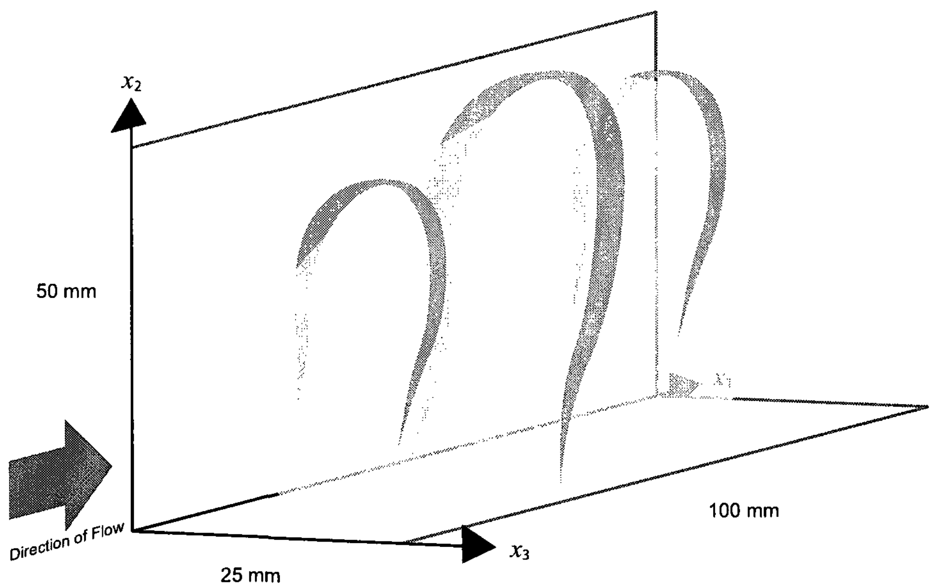

Figure 6.9: Conceptual illustration of the hairpin vortex configuration that would produce the typical low-speed zones of uniform velocity found in USF (illustration created by C. D. McKnight-MacNeil, 2009).

example of these structures in a slightly less cluttered environment.

The same motivations applied to the use of a reduced flow rate in the PIV measurements. The measurements in the slower flow in the vertical plane displayed the same characteristics as those at full speed but much exaggerated. These similarities include the separation of zones of uniform velocity, the strong shear layers, and the location of the vortices along these steep velocity gradients; however, these characteristics were exaggerated in the sense that the velocity gradients were steeper and the vortices were larger than in the full-speed flow. These patterns were therefore more pronounced in the lower-speed flow and aided in the understanding of the mechanisms at work.

The lower-speed flow was examined in the inclined plane after the attempt to track structures in full speed flow turned out to be unsuccessful. The reduced turbulent mixing resulted in structures that were much easier to track even with the relatively low temporal resolution of the PIV system. The reconstructed structures provided perhaps the most striking visual representations of the differences between the full speed and reduced speed USFs. When compared to the reconstructions of the scanning dye visualisations, the difference in length of the structures in unmistakable.

Because the structures in the lower-speed flow tended to be much larger than those observed in the full speed flow, their lengths and proportions should not be used to characterise those structures of the full speed USF. The fact that the structures in the lower-speed flow have different length scales suggests that the shear generating apparatus does not have an overriding effect on the size of the scales, because both flows were created using the same apparatus.

6.5 The vortex lifetime

The lifetime of the large-scale structures was estimated by following the structures as they travelled downstream. A typical value of about $\Delta\tau = 0.5$ was estimated to be the average dimensionless time over which the bubble patterns remained coherent. This indirect measurement, however, was also influenced by the turbulent mixing and the dispersion of the bubbles, resulting in a low estimate of the lifetime of the vortices.

The lifetime and development of the strong clockwise vortices in the vertical plane were investigated using the traversing PIV system. Vortices were not observed to be generated in the flow, grow, and die out. Instead, the initial vortices generated by the shear generator effects were observed to reorganize as they were convected downstream, and all the large downstream vortices were related to these initial vortices. This is consistent with the following Helmholtz vorticity equation for an incompressible homogeneous fluid

$$\partial\Omega/\partial t + (U \cdot \nabla)\Omega = (\Omega \cdot \nabla)U + \nu\nabla^2\Omega, \tag{6.1}$$

which contains no source term. Morton [30] describes that in homogeneous fluids vorticity may only be generated at the boundaries of the flow. In the present case this means that all downstream vortices contained vorticity generated by the shear generator. The vortices were observed to grow through the merger of multiple vortices and to cease existing as single entities by splitting up into separate vortices. This, however, meant that a lifetime could not be estimated as the vortices had no definite beginning or end to their lives.

6.6 Summary of length scales

Many length scales were measured in the set of experiments conducted. These include the typical spacing of the observed vortical structures as well as fundamental scales of the equipment and calculated turbulent scales. These scales are expected to be related to each other and in some cases are different measures of the same property. In order to compare all these length scales, they are divided depending on their associated direction into the streamwise (x_1), spanwise (x_2), and transverse (x_3) scales. These three groups are separately summarised in Tables 6.1 to 6.3.

The streamwise scales include those calculated from the LDV measurements of the velocity, the lengths of the structures observed using hydrogen bubbles, and the lengths of the reconstructed structures from the scanning dye visualisation. The fundamental time scale based on the shear rate is also presented for comparison to the other scales. The observed lengths of the structures are on the same order as the integral length scale.

The spanwise scales are all different measures of the typical width of the structures.

Method	Property	Value
Shear scale	$U_c/\left(\mathrm{d}\langle U_1\rangle/\mathrm{d}x_2\right)$	365 ± 20 mm
LDV, autocorrelation	$L_{11,1}$	27 ± 2 mm
LDV, k.e. estimate	$L_{11,1}$	50 ± 20 mm
LDV, k.e. estimate	$\lambda_{11,1}$	14 ± 3 mm
Scanning dye visualisation	length of structures	70 ± 10 mm
H_2 bubbles	length of structures	25 ± 10 mm

Table 6.1: Summary of the observed streamwise length scales at $\tau \approx 6$.

Method	Property	Value
H_2 bubbles	width of structures	15 ± 10 mm
PIV, horizontal plane	separation of vortex pairs	20 ± 10 mm
PIV, inclined plane	separation of vortex pairs	15 ± 10 mm
Scanning dye visualisation	separation of vortex pairs	30 ± 20 mm

Table 6.2: Summary of the observed spanwise length scales at $\tau \approx 6$.

Method	Property	Value
Shear generating apparatus	vertical spacing	25.4 mm
LDV, autocorrelation	L_{22}	13 ± 3 mm
PIV, vertical plane	vertical separation of shear layers	40 ± 10 mm

Table 6.3: Summary of the observed transverse length scales at $\tau \approx 6$.

These measurements are less scattered than the streamwise scales and are consistently in the range of about 20 mm.

The transverse scales include the imposed length scales from the shear generating apparatus, the transverse integral length scale, and the mean vertical separation of the shear layers measured using PIV in the vertical plane. There is a large difference between the mean spacing of shear layers far downstream and the vertical spacing of the shear generating apparatus.

6.7 Inverted versus upright structures

Results from all experiments support the hypothesis of the prevalence of hairpin vortices. The main exception to this classical view of hairpin vortices is the observation of the existence of inverted as well as upright hairpin vortices in the USF. Furthermore, these inverted structures appear to be as common as the upright structures.

The scanning dye visualisations provided observations of vortex pairs at all inclinations. Based on analysis using the pair matching algorithm, it was concluded that there was a wide distribution of the inclinations of the vortex pairs, with slightly higher populations of upright or inverted structures compared to other inclinations. Although inverted hairpin vortices were not observed in the hydrogen bubble visualisations, it was inferred that this experiment was biased towards the viewing of upright structures. This bias occurred because the flood lights were located behind and below the water tunnel. Because hydrogen bubbles are easier to see when backlit, the structures that moved upwards away for the main stream were observed easier, whereas the structures that dragged below the main bubble plane would have been obstructed by the high bubble concentration in this plane.

The scanning dye visualisations indicated that the inverted structures were inclined at the same angle as the upright structures, but it was uncertain if and where the legs were attached by a vortex head and what the direction of rotation of this head was. If the inverted vortex pairs were connected by a head, two configurations would be possible; the head would connect the legs either at the top of the structure or at the bottom. The first configuration would require the head to rotate counter-clockwise in the vertical plane, which does not agree with measurements that indicate that

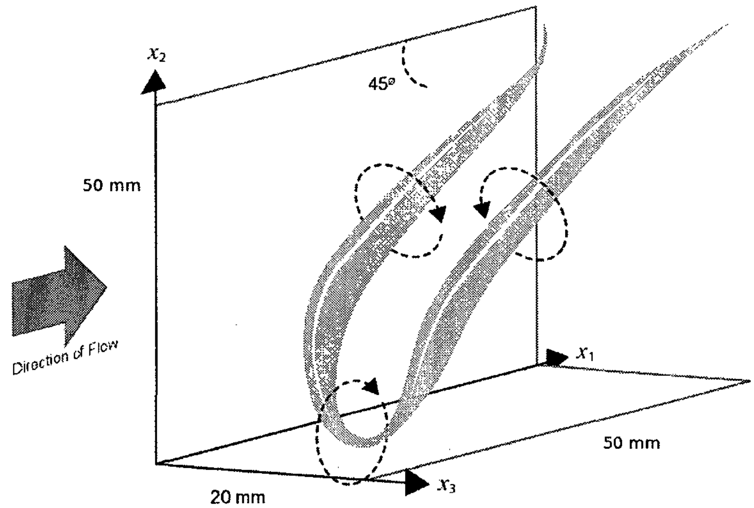

Figure 6.10: Sketch of a possible configuration of the inverted horseshoe vortex (illustration created by C. D. McKnight-MacNeil, 2009).

counter-clockwise vortices were much less common than clockwise vortices in the vertical plane. The second possible configuration conforms to having a clockwise rotating head and coincides with the orientation of the second characteristic vortex found by Rogers and Moin [35]. This configuration is illustrated in Figure 6.10. Other than their direction of rotation, the legs of the inverted hairpin have similar dimensions to those of the upright hairpin. The mechanism for this explanation could be that the mean strain, unhindered by the presence of a wall, causes stretching in both upwards and downwards directions, namely at $45\,^{\circ}$ and $-135\,^{\circ}$. In the turbulent boundary layer, the wall would act as to suppress the development of the inverted structures, leaving only the upright hairpins remaining, whereas the removal of the wall effects in the USF results in the development of these inverted structures as well. As far as the author is aware, such a mechanism has not been described in previous literature. This mechanism is consistent with the illustration by Smith et al. [39] in Figure 6.11, which was originally produced to illustrate the development of a symmetric hairpin. In this illustration, the inverted vortices that are currently discussed would form between the main and subsidiary upright structures.

Another possibility is that the inverted structures have been separated from their horseshoe heads and have twisted and turned in the flow to achieve this wide range

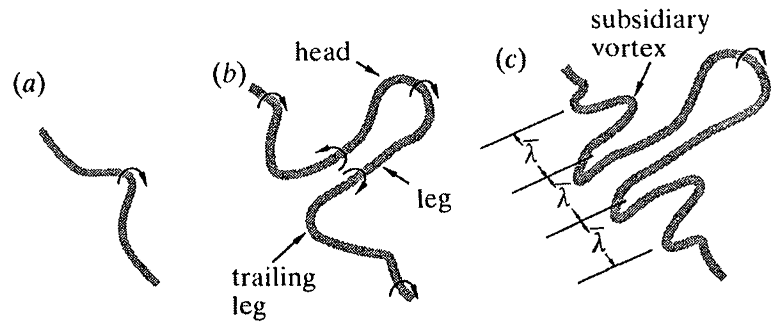

Figure 6.11: Classic view of the evolution of a symmetric hairpin vortex in a the turbulent boundary layer. (a) Initial distortion, (b) development of vortex legs and head, (c) evolution of subsidiary vortices and penetration toward the surface. Figure by Smith et al. [39].

of inclinations. This theory is supported by the observations of twisting vortex pairs in the scanning dye visualisation and by the observations using PIV of spanwise and transverse wandering of the zones of uniform velocity associated with the vortex structures. This would also account for the wide range of inclinations of the vortex pairs rather than only two possible inclinations at 0° and 180°.

6.8 Comparison of USF to the turbulent boundary layer

As discussed in the literature review, the majority of experimentally realised USF, including the present study, have flow properties comparable to those in the outer layer of the turbulent boundary layer. The works by Head and Bandyopadhyay [16] and Adrian et al. [2] both focus on the vortex structures in the outer region of the turbulent boundary layer and will serve as the main sources for comparison.

First of all, vortices are very common in both shear flows. It has been remarked by Adrian et al. [2] that most PIV measurements in the turbulent boundary layer contained at least one vortex. This is definitely the case for the USF where the average number of vortices per PIV measurement exceeds ten in all configurations. Similar remarks can be made about the zones of uniform momentum observed in the vertical PIV fields. These zones have also been observed in 75% of the PIV measurements collected by Adrian et al. in the outer boundary layer.

The actual sizes of the structures cannot be compared to the sizes of those observed

	Boundary layer	Uniformly sheared flow
length of structures	$\sim \delta$	$\sim 2L_{11}$
width of structures	$\sim 100\delta_\nu (\sim 0.2\delta)$	$\sim L_{11}$
diameter of vortices	$\sim 5\delta_\nu (\sim 0.01\delta)$	$\sim 0.2L_{11}$
angle of structures	$45\,^\circ$	$45\,^\circ$

Table 6.4: Comparison of the sizes of fully developed hairpin structures of USF to those observed in the turbulent boundary layer (assuming $\delta/\delta_\nu \approx 500$).

in the turbulent boundary layer because the types of length scales that can be defined in the two flows are very different. Most observations in the turbulent boundary layer are reported in terms of either the boundary layer thickness δ or the viscous length scale $\delta_\nu = \nu/\sqrt{\tau_w/\rho}$, where τ_w is the wall shear stress. In the experiments by Adrian et al. [2], the ratio of δ/δ_ν, known as the von Kármán number, is about 500. Neither of these length scales are applicable to USF as there are no walls or boundaries. The current results are therefore non-dimensionalised by the integral length scale for comparison to the findings in the outer boundary layer reported by Head and Bandyopadhyay [16], Adrian et al. [2], and Davidson [7] as presented in Table 6.4. The scales of the two types of flows are comparable, but the structures of the turbulent boundary have smaller widths and diameters in relation to their lengths.

This difference in the elongation of the vortex loops is probably due to a difference in Reynolds number of the flows. As mentioned in section 6.1.1, Head and Bandyopadhyay [16] explain that at very low Reynolds numbers, the hairpin vortices look more like wide loops or horseshoes, rather than the elongated hairpin shape observed at moderate-high Reynolds number. This effect is also demonstrated in their photographs of mushroom-shaped ejections in a smoke-filled boundary layer, which have been reproduced in Figure 6.12. The legs of the hairpin structures are much closer to each other at higher Reynolds number. The current USF has a turbulence Reynolds number in the range of $80 < Re_\lambda < 100$, which is relatively low in comparison to the experiments in the turbulent boundary layer, which had values in the range of

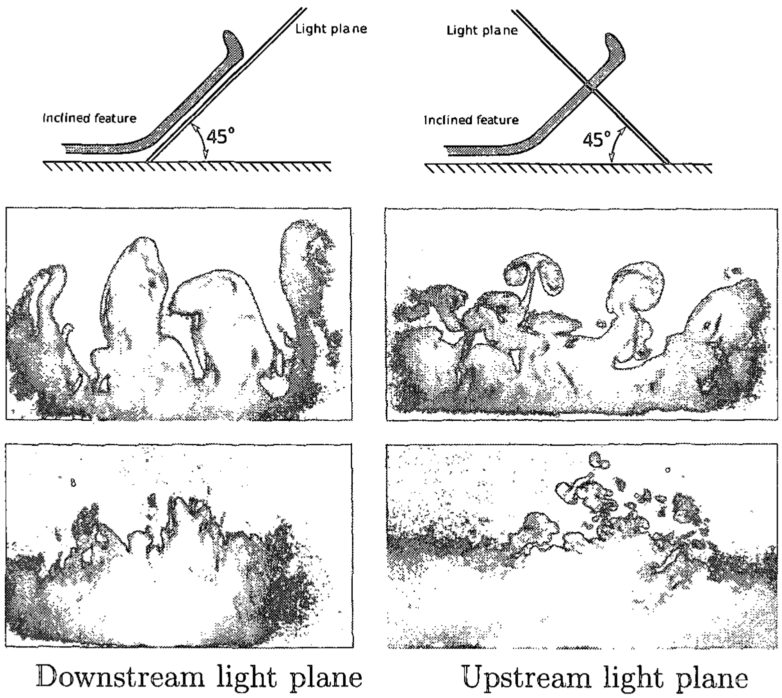

Figure 6.12: Comparison of the structures in the turbulent boundary layer at $Re_\theta = 600$ (top) and $Re_\theta = 9400$ (bottom). The views on the left are in a plane inclined at 45 degrees to the downstream direction and those on the right are in a plane inclined at 45 degrees to the upstream direction, equivalent to the inclined PIV plane of the present study. Images by Head and Bandyopadhyay [16].

$100 < Re_\lambda < 400$ [2].

Similarities between the structures of the USF and the turbulent boundary layer can also be found by comparing the corresponding velocity maps. The observations of ramp-like structures provide evidence about the similar action of the vortices. Vortex heads in USF are found to line up in a nearly streamwise direction, just like they are observed to do in the turbulent boundary layer. The ratios of the spacings between the shear layers and the diameters of the vortices is also comparable in both flows. The lack of wall in USF does not seem to hinder the organization of spanwise vortices into small groups travelling together streamwise with the same convection velocity.

The presence of inverted as well as upright structures in the USF is one of the most significant differences. The presence of inverted structures does not agree with the observations of typical coherent structures in the boundary layer. As discussed in section 6.7, this finding may be attributed to the effect that the wall has in the development of the hairpin structures. The nature of these inverted structures requires further investigation.

Chapter 7

Conclusions and recommendations for future work

Uniformly sheared flow was successfully reproduced in a water tunnel, with characteristics comparable to those in previously published experiments. A turbulence Reynolds number Re_λ in the range of 80 to 100 was obtained, as well as a shear coefficient S^* of approximately 11. Laser Doppler velocimetry was used to verify that the turbulent properties agreed with conventional values.

Horseshoe-shaped structures were observed using flow visualisation. Scanning dye visualisation identified the presence of elongated quasi-streamwise vortex pairs, which were interpreted as the legs of horseshoe vortices. These structures had lengths of about 70 mm and a spanwise spacing of about 30 mm. Vortex pairs were observed having a range of orientations, which included both upright and inverted horseshoe structures. Using hydrogen bubble visualisations, the heads of the horseshoe structures were observed to connect the quasi-streamwise legs at the downstream end.

Measurements using particle image velocimetry were in agreement the observations from the flow visualisations. Furthermore, the instantaneous flow was observed to consist of zones of roughly uniform velocity separated by strong shear layers, rather than having uniform shear. These zones were up to 100 mm in length in the streamwise direction and had an average spanwise spacing of 30 mm. Strong vortices were found to be aligned along these shear layers.

The current work was an introductory exploration of the coherent structures of USF. Very little experimental evidence preceded this work, and several measurement and visualisation techniques were tested in the investigation of this topic.

The PIV measurement technique produced by far the most promising results. The velocity contours alone provided new knowledge of the instantaneous structure of USF. An algorithm for the identification of vortices was developed and implemented with some success. Further development of this algorithm or the analysis of the relationships between the instantaneous flow properties and the vortex properties would be a good extension of this work. Complex flow properties such as the rate of strain or the Reynolds stress distributions could be investigated using the current data and might lead to improved insight into the flow structure.

The scanning dye visualisations were not as successful as anticipated due to the poor resolution of the camera, though they produced some interesting dye patterns which were carefully and diligently extracted. An extension of this method either using a different camera or scanning in a different direction might be worthwhile. If much clearer pictures were obtained, perhaps the heads of the horseshoe-shaped vortices would be more easy to identify.

Lastly, the investigation of the true nature of the inverted structures observed in this introductory work would have enough scope to be the topic of an entirely separate investigation. Many questions remain regarding these observations such as: what shape do they have in 3D? how do they contribute to the Reynolds stress and the turbulent kinetic energy? and how do they develop? Inverted hairpins were observed in DNS studies of USF in the 1980s but have since received little attention as they do not appear in the turbulent boundary. This significant observation may perhaps be consequential in the understanding of the fundamental structure of shear layers and deserves to be examined in depth.

Bibliography

[1] R. J. Adrian. Hairpin vortex organization in wall turbulence. *Physics of Fluids*, 19(4):041301, 2007.

[2] R. J. Adrian, C. D. Meinhart, and C. D. Tomkins. Vortex organization in the outer region of the turbulent boundary layer. *Journal of Fluid Mechanics*, 422:1–54, Nov. 2000.

[3] R. J. Adrian and P. Moin. Stochastic estimation of organised turbulent structure: homogeneous shear flow. *Journal of Fluid Mechanics*, 190:531–559, 1988.

[4] P. Chakraborty, S. Balachandar, and R. J. Adrian. On the relationships between local vortex identification schemes. *Journal of Fluid Mechanics*, 535:189–214, July 2005.

[5] F. H. Champagne, V. G. Harris, and S. Corrsin. Experiments on nearly homogeneous turbulent shear flow. *Journal of Fluid Mechanics*, 41(1):81–139, 1970.

[6] Dantec Dynamics. Laser Doppler anemometry - measurement principles. http://www.dantecdynamics.com, August 2009.

[7] P. Davidson. *Turbulence - An introduction for scientists and engineers.* Oxford University Press, New York, 2004.

[8] F. A. De Souza, V. D. Nguyen, and S. Tavoularis. The structure of highly sheared turbulence. *Journal of Fluid Mechanics*, 303:155–167, 1995.

[9] Y. Dubief and F. Delcayre. On coherent-vortex identification in turbulence. *Journal of Turbulence*, 1(11), December 2000.

[10] W. Dunn. *Vortex Shedding from Cylinders with Step-Changes in Diameter in Uniform and Shear Flows.* PhD Dissertation, University of Ottawa, Ottawa, Ontario, August 2004.

[11] W. Dunn and S. Tavoularis. The use of curved screens for generating uniform shear at low reynolds numbers. *Experiments in Fluids*, 42(2):281–290, February 2007.

[12] R. E. Falco. Coherent motions in outer region of turbulent boundary layers. *Physics of Fluids*, 20(124), 1977.

[13] M. Ferchichi and S. Tavoularis. Reynolds number effects on the fine structure of uniformly sheared turbulence. *Physics of Fluids*, 12(11):2942–2953, 2000.

[14] Q. Gao, C. Ortiz-Duenas, and E. K. Longmire. Circulation signature of vortical structures in turbulent boundary layers. In P. Jacobs, T. McIntyre, M. Cleary, D. Buttsworth, D. Mee, R. Clements, R. Morgan, and C. Lemckert, editors, *16th Australasian Fluid Mechanics Conference (AFMC)*, pages 135–141, Brisbane, Australia, December 2007. School of Engineering, The University of Queensland.

[15] V. G. Harris, J. A. H. Graham, and S. Corrsin. Further experiments in nearly homogeneous turbulent shear flow. *Journal of Fluid Mechanics*, 81(4):657–687, 1977.

[16] M. R. Head and P. Bandyopadhyay. New aspects of turbulent boundary-layer structure. *Journal of Fluid Mechanics*, 107:297–338, 1981.

[17] P. Holmes, J. L. Lumley, and G. Berkooz. *Turbulence, Coherent Structures, Dynamical Systems, and Symmetry.* Cambridge University Press, 1996.

[18] A. K. M. F. Hussain. Coherent structures - reality and myth. *Physics of Fluids*, 26(10):2816–2850, October 1983.

[19] A. K. M. F. Hussain. Coherent structures and turbulence. *Journal of Fluid Mechanics*, 173:303–356, May 1986.

[20] ISS Inc. Table of excitation and emission wavelengths of fluorophores. http://www.iss.com/resources/spectra.html, July 2009.

[21] U. Karnik and S. Tavoularis. Generation and manipulation of uniform shear with the use of screens. *Experiments in Fluids*, 5:247–254, 1987.

[22] S. Kida and M. Tanaka. Reynolds stress and vortical structure in a uniformly sheared turbulence. *Journal of the Physical Society of Japan*, 61(12):4400–4417, December 1992.

[23] B. Kislich-Lemyre. *The large-scale structure of uniformly sheared turbulence and its distortion by a solid wall at rest or in motion.* PhD Dissertation, University of Ottawa, July 2002.

[24] S. J. Kline, W. C. Reynolds, R. A. Schraub, and P. W. Runstadler. The structure of turbulent boundary layers. *Journal of Fluid Mechanics*, 30(741), 1967.

[25] Lavision GmbH. Particle image velocimetry. http://www.lavision.de, October 2008.

[26] M. J. Lee, J. Kim, and P. Moin. Structure of turbulence at high shear rate. *Journal of Fluid Mechanics*, 216:561–583, June 1990.

[27] E. K. Longmire, C. Ortiz-Duenas, Q. Gao, and N. Saikrishnan. Eddy structure in turbulent boundary layers. In *7th International Symposium on Engineering Turbulence Modelling and Measurements*, volume 1, pages 8–13, Limassol, Cyprus, 4-6 June 2008.

[28] E. Menu. Turbulence structure near a moving wall. Internship report, University of Ottawa, September 2004.

[29] F. Moisy. Pivmat - a piv post-processing and data analysis toolbox for matlab. Laboratory FAST, University Paris Sud, CNRS, October 2008.

[30] B. R. Morton. The generation and decay of vorticity. *Geophysical & Astrophysical Fluid Dynamics*, 28:277–308, 1984.

[31] N. Moshtagh. Minimum volume enclosing ellipsoid. MATLAB Central File Exchange, January 2009.

[32] S. Pope. *Turbulent Flows.* Cambridge University Press, 2000.

[33] M. Raffel, C. E. Willert, and J. Kompenhans. *Particle Image Velocimetry: A practical guide.* Springer, 1998.

[34] S. K. Robinson. Coherent motions in the turbulent boundary layer. *Annual Review of Fluid Mechanics*, 23:601–639, 1991.

[35] M. M. Rogers and P. Moin. The structure of the vorticity field in homogeneous turbulent flows. *Journal of Fluid Mechanics*, 176:33–66, 1987.

[36] J. J. Rohr, E. C. Itsweire, K. N. Helland, and C. W. V. Atta. An investigation of the growth of turbulence in a uniform-mean-shear flow. *Journal of Fluid Mechanics*, 187:1–33, 1988.

[37] W. G. Rose. Results of an attempt to generate a homogeneous turbulent shear flow. *Journal of Fluid Mechanics*, 25(1):97–120, 1966.

[38] J. Shen. Tools for nifti and analyze image. MATLAB Central File Exchange, July 2009.

[39] C. R. Smith, J. D. A. Walker, A. H. Haidari, and U. Sobrun. On the dynamics of near-wall turbulence. *Philosophical Transactions: Physical Sciences and Engineering*, 336(1641):131–175, 1991.

[40] A. J. Smits and T. T. Lim, editors. *Flow visualization.* Imperial College Press, illustrated edition, 2000.

[41] Specialist Committee on Uncertainty Analysis of 25th ITTC. *Recommended Procedures and Guidelines - Uncertainty Analysis of Particle Image Velocimetry.* 25th International Towing Tank Conference, September 2008.

[42] S. Tavoularis. Asymptotic laws for transversely homogeneous turbulent shear flows. *Physics of Fluids*, 28(3):999–1001, March 1985.

[43] S. Tavoularis. MCG 5152 - Theory of Turbulence - Course Notes. Department of Mechanical Engineering, University of Ottawa, 2005.

[44] S. Tavoularis. *Measurement in Fluid Mechanics.* Cambridge University Press, 2005.

[45] S. Tavoularis and S. Corrsin. Experiments in nearly homogeneous turbulent shear flow with a uniform mean temperature gradient. Part 1. *Journal of Fluid Mechanics*, 104:311–347, 1981.

[46] S. Tavoularis and U. Karnik. Further experiments on the evolution of turbulent stresses and scales in uniformly sheared turbulence. *Journal of Fluid Mechanics*, 204:457–478, 1989.

[47] M. J. Walsh. Riblets. In D. M. Bushnell and J. M. Hefner, editors, *Viscous drag reduction in boundary layers*, volume 123 of *Progress in Astronautics and Aeronautics*, pages 203–254. American Institute of Aeronautics and Astronautics, 1990.

[48] J. Zhou, R. J. Adrian, S. Balachandar, and T. M. Kendall. Mechanisms for generating coherent packets of hairpin vortices in channel flow. *Journal of Fluid Mechanics*, 387:353–396, May 1999.